Modeling of the Reaction to Fire of Materials in Under-Ventilated Spaces. Application on the PMMA

Rita Nohra

THESE

Pour l'obtention du Grade de
DOCTEUR DE L'ECOLE NATIONALE SUPERIEURE DE MECANIQUE ET D'AEROTECHNIQUE
(Diplôme National – Arrêté du 25 mai 2016 Modifié par l'Arrêté du 26 Août 2022)

Ecole Doctorale :
MIMME Mathématiques, Informatique, Matériaux, Mécanique, Energétique

Secteur de Recherche : Energétique, thermique et combustion

Présentée par : Rita NOHRA

****

Modélisation de la réaction au feu des matériaux en milieux sous ventilés. Application au PMMA.

****

Directeur de thèse : Thomas ROGAUME
Co-encadrant : Benjamin BATIOT, Damien MARQUIS

****

Soutenue le 15 mars 2024
devant la Commission d'Examen

****

JURY

Rapporteurs :
COLLIN Anthony, Pr, Université de Lorraine
MERCI Bart, Pr, Gent Université (Belgique)
Membres :
FONTAINE Gaelle, PR, Université de Lille
PIZZO Yannick, IR, CNRS
BATIOT Benjamin, MCF, Université de Poitiers
MARQUIS Damien, IR, LNE
ROGAUME Thomas, Pr,Université de Poitiers

"All I Know Is That I Know Nothing"

AKNOWLEDGMENT

This thesis is the result of years of dedication and hard work. It has been a journey marked by moments of passion and sometimes doubt. None of this would have been possible without the invaluable assistance and support of numerous individuals, whose presence I am deeply grateful for and whose contributions I wholeheartedly acknowledge.

Je tiens à exprimer ma plus sincère gratitude à mes enseignants, Damien, Benjamin et Thomas, pour vos conseils précieux, votre disponibilité et votre soutien, qui ont joué un rôle important dans ma progression dans mes recherches.

Je suis reconnaissant à mes collègues pour vos conseils avisés, vos discussions enrichissantes et votre expertise, qui ont grandement contribué à mon développement personnel et académique. De plus, je vous remercie pour les moments de convivialité et les échanges qui ont renforcé nos liens amicaux et professionnels.

A mes amis et ma famille , qui ont été bien plus que de simples compagnons de route, je vous adresse mes plus sincères remerciements. Vos encouragements continus et vos sourires, qui ont été autant de sources de courage dans les moments les plus difficiles. Vous avez été le lien précieux qui m'a toujours rattaché à mes racines, étant éloigné de mon pays et de ma culture.

À mon frère, je tiens tout d'abord à te remercier pour ton soutien indéfectible tout au long de ce parcours. Tes encouragements constants et ta présence à mes côtés ont été une source de motivation inestimable. Mais aussi, je te remercie de m'avoir montré chaque jour combien tu es fière de moi doko.

À mes parents, je n'ai pas assez de mots pour vous exprimer ma gratitude. Vous m'avez toujours inculqué l'importance de l'éducation, et vous avez cru en moi même lorsque je doutais de moi-même. Votre amour inconditionnel et vos sacrifices m'ont permis d'accomplir ce que je suis aujourd'hui.

To my partner, your love and unwavering support has been my greatest motivation. Thank

you for believing in me, even when I didn´t believe in myself. Thank you for being my calmness and my home away from home.

Vielen Dank an die Familie meines Partners, dass Sie mir das Gefühl geben, ein Teil von Ihnen zu sein. Sie haben maßgeblich dazu beigetragen, dass ich mich unterstützt und geliebt fühle.

Enfin, je tiens à exprimer ma reconnaissance envers toutes les personnes qui ont contribué de près ou de loin à la réalisation de cette thèse. Vos conseils, vos discussions stimulantes et votre collaboration ont enrichi mon travail et ont contribué à son succès.

TABLE OF CONTENTS

LIST OF FIGURES

LIST OF TABLES

NOMENCLATURE

Latin letters

A	Area, m^2
B	Spalding number
Bi	Biot number
c_p	Specific heat at constant pressure, J/kgK
d	Diameter, m
D	Equivalent diameter, m
Da	Damköhler number
F	View factor
Fo	Fourier number
h_c	Convective heat transfer coefficient, W/m^2K
ΔH_c	Heat of combustion, J/kg
Δh_{CO}	Net heat release per unit mass of oxygen consumed for CO, MJ/kg
Δh_{O2}	Net heat release per unit mass of oxygen consumed, MJ/kg
k	Thermal conductivity, kW/mK
K	Constant
L	Thickness of the sample
L_G	Heat of gasification, kJ/g
L_m	Modified heat of gasification, kJ/g
m	Mass, g
$\dot{m}$	Mass loss rate, g/s
$\dot{m}''$	Mass loss rate per unit area, g/sm^2
$\dot{m}'''$	Mass loss rate per unit volume, g/sm^3
Nu	Nusselt number
Pr	Prandt number
$\dot{q}''$	Heat flux, kW/m^2
$\dot{Q}$	Total heat release, MW/m^2
$\dot{Q}''$	Heat release rate, kW/m^2

r	Stoichiometric ratio air/fuel
Re	Reynolds number
t	Time, s
T	Temperature, K
v	Velocity, m/s
V	Volume, m^3
X_a	Mole fraction of the component a
X_{O2}	Volume fraction of the oxygen concentration
Y	Mass fraction

Greek letters

α	Thermal diffusivity, (m^2/s)
β	In-sample heating rate, (K/s)
ϵ	Total hemispherical emissivity
κ	Extinction coefficient, $1/m$
ϕ	Depletion factor, $1/m$
ν	Kinematic viscosity, (m^2/s)
ρ	Density, kg/m^3
σ	Stefan–Boltzmann constant, $5.67 \times 10^{-8} W/m^2 K^4$
χ	Fraction

Subscripts

∞	Ambient
air	Under air
c	Convective
cat	Catalytic
$cond$	Conductive
cr	Critical

$duct$	Duct corresponding to the chimney of the CACC
e	External
eff	Effective
f	Flame
F	Fuel
g	Gas
$gauge$	At the gauge of the fluxmeter
i	Of species i
ig	Ignition
LHV	Lower heating value
$O2$	Under a certain oxygen concentration
P	Product
py	Pyrolysis
r	Radiative
s	Surface
tc	Thermocouple
tot	Total

Superscripts

$\dot{}$	Per unit time, $1/s$
$''$	Per unit area, $1/m^2$
$'''$	Per unit volume, $1/m^3$
$\overline{...}$	Time averaged
$< ... >$	Space averaged
0	Initial
A	Analyzer-measured variables
in	Incoming air

Acronyms

CACC	Controlled atmosphere cone calorimeter
CADUCEE	Controlled atmosphere device for unburnt and carbon emission evaluation
CC	Cone calorimeter
CHF	Critical heat flux
FPA	Fire propagation apparatus
HRR	Heat release rate
LOC	Limiting oxygen concentration
MLR	Mass loss rate
MMA	Methyl methacrylate
pHRR	Peak heat release rate
pMLR	Peak mass loss rate
PMMA	Polymethyl methacrylate
SMLR	Specific mass loss rate
THR	Total heat release
TRP	Thermal response parameter

Abbreviations

F	Fuel
Ox	Oxidation
P	Product
Py	Pyrolysis

INTRODUCTION

The initiation and propagation of fire are highly dependent on the environment in which it starts. An important factor to consider when studying fire is the ventilation or fresh air supply. When the oxygen concentration in the environment is high, the fire is mainly related to the amount of combustible material. However, in poorly ventilated atmospheres, the behavior of the fire is determined by other factors. In the initial stages, it is similar to well ventilated fire, but as time passes and the combustible material burns, the concentration of oxygen begins to decrease because of its limited quantity, thus, the fire goes into an underventilated state and and it becomes to be controlled by the amount of oxygen present. The flame structure and radiation decreases, having a significant impact on the thermal decomposition of the solid matrix. The decline of the mass loss rate of the materials limits the quantity of combustible gas kept into the gas phase for the combustion, impacting than in turm the flame. Complex unstable behavior can be observed as the heat and mass transfers of the materials present decreases. In addition, toxic, flammable gases begin to be form in the enclosed space, leading to possible various hazardous scenarios.

Such confined spaces can be found in transport such as aircraft and trains or in nuclear facilities. Additionally, to minimize energy losses and increase efficiency, new legislations mandate the improvement of insulation in buildings and structures. Building design has changed as a result of the requirement to minimize energy loss, with a focus on producing well-insulated spaces. Such insulation improves efficiency, but it also restricts the amount of outside air that can enter the building. As a result, there is a serious risk of under-ventilation in these interior spaces, which raises new issues related to fire safety. The new safety challenge and public expectations contribute to the large development of the studies of fire safety engineering, which are based on the use of numerical models, notably CFD codes. In those different modelling tools (as FDS, Firefoam or others) have been developed and improved for many years for well ventilated conditions, their application to under oxygenated situation is questionable.

In fact, experiments and studies on fire in unventilated rooms are quite limited, particularly regarding the effects of varying oxygen concentrations. This resulted in existing fire models

relying on parameters recorded under ambient air conditions, which introduces a significant bias in the results. To improve the accuracy and reliability of fire models, and consequently improve predictions, there is a need for an understanding of fire dynamics in environments with reduced oxygen levels. In this context, the current work focuses on the experimental characterization of polymers under those conditions.

Within this framework, the present study examines key parameters critical to understand the fire behavior of polymers in both the solid and gas phases in reduced oxygen atmospheres. For this, the parameters investigated include heat release rate, heat flux at the sample surface, gas temperatures, mass transfer and in-sample parameters. The investigation uses a controlled atmosphere cone calorimeter and square thick samples of clear polymethyl methacrylate (PMMA) with dimensions of $100 \times 100 \times 30mm$ in a horizontal configuration. The PMMA is a material widely used in applications such as aircraft and billboards. PMMA is chosen because of its well-documented thermochemical properties and its wide use in fire rearche because of its relatively simple decomposition process. The oxygen concentrations are varied from $21\%vol$ to $10\%vol$. Three external heat fluxes ranging from $12kW/m^2$ to $35kW/m^2$ are applied. This approach allows for a thorough investigation of how varying oxygen concentrations in vitiated atmospheres, coupled with varying external heat fluxes, affect critical fire-related parameters.

The following thesis is divided into 4 chapters. The first one provides an overview of research that has been done on PMMA in air and in vitiated environments. The state of the art allows to have comparative basis for the current study but also highlights the gaps in the fire safety community.

The second chapter describes the experimental setup used, which is the controlled atmosphere cone calorimeter, but also the different modifications it has undergone to be able to measure the different parameters mentioned above. This chapter also describes the calculation method used to calculate the heat release rate, the gas temperatures and the averages throughout the study.

Having established the experimental basis, the chapter 3 focuses on the results obtained under normal air conditions. This chapter serves as a basic reference for the following

chapter in vitiated atmospheres.

Finally, the last chapter focuses on the study of these parameters in vitiated atmospheres. The first section of this last chapter deals with the behaviour of the parameters in vitiated atmospheres under an external heat flux. The second and final section focuses on the combined effect of oxygen concentration and external heat flux on both the thermal decomposition and the combustion processes.

CHAPTER 1

STATE OF THE ART

Table of Contents

The present study focuses on the thermal decomposition and the combustion of PMMA (polymethylmethacrylate) in under-oxygenated atmospheres. PMMA is a widely used polymer that is used in applications ranging from building, furnitures, advertising (such as signs and billboards) to art (in design objects and sculptures) and even aviation (for aircraft windows and helicopter cockpits). PMMA is also used as a protective or containment window for glove boxes in the nuclear industry. It is therefore a material of major interest in the fire safety community. In addition, PMMA was chosen because it does not produce carbon residues during combustion and its thermo-physical properties are well documented. Many studies focused on the characterization of the PMMA in the context of fire research. Moreover, in confined spaces, where there is a lack of ventilation and no fresh air supply, the oxygen concentration is decreasing as it is consumed by combustion. This decrease in oxygen levels affects the fire behavior (thermal decomposition and combustion) of the materials present in the space [1]. Several past experimental studies have been carried out to observe the effects of varying oxygen levels on combustion dynamics and material response. This

chapter presents a review of the existing literature. It is divided into 3 main parts. The first section focuses on understanding the thermal decomposition process of PMMA by reviewing findings from relevant studies. The second section deals with a review of the literature on the behaviour of PMMA in under-oxygenated atmospheres. This review covers a wide range from the effects of oxygen depletion on material properties such as viscosity to its effects on PMMA behaviour including ignition time, flame heat flux, burning rate and more. Finally, analytical models that have been developed to predict various properties associated with PMMA behavior under different conditions are presented.

1.1 PMMA fire behvaior under air

This section provides a non-exhaustive literature review focusing on the thermal decomposition and the combustion process of the PMMA under air atmosphere. A brief description is provided first, followed by detailed explanations of both solid and gas phase characteristics, aiming to summarise the key aspects of PMMA thermal decomposition and combustion. Numerous studies have been conducted to investigate the combustion behavior under ambient air, focusing on parameters like pressure and humidity [2, 3, 4], flow velocity [5], sample orientation [6], absorption [7, 8]. While these studies provide valuable insights, they are outside the scope of the current study.

1.1.1 Thermal decomposition of PMMA under air

This section focuses on the thermal decomposition of the PMMA under air. On the molecular level, a well-defined mechanism of thermal decomposition of PMMA is described in the literature [9, 10] and can be summarised in four steps:

- PMMA depolymerizes to yield monomers derived from methyl methacrylate (MMA) through pyrolysis or oxidation reactions.
- The MMA-derived molecules undergo oxidation and are converted to oxygenated products.

- The oxygenated molecules are further oxidized to form exhaust gases and gaseous products.
- These gaseous molecules undergo oxidation into the gas phase.

The previous mechanism is summarized in Equation 1.1.1.

$$\begin{aligned} \text{PMMA} &\xrightarrow{\text{Ox/Py}} \text{MMA} \\ \text{MMA} &\xrightarrow{\text{Ox}} \text{Oxygenaed products} \\ \text{Oxygenaed products} &\xrightarrow{\text{Ox}} \text{Gaseous products} \\ \text{Gaseous products} &\xrightarrow{\text{Ox}} \text{Gas} \end{aligned} \tag{1.1.1}$$

A brief description of the PMMA's molecular decomposition has been provided, however the study focus does not extend to the molecular level of behavior. The material level is the main focus of this investigation. On the material level, the decomposition process of the PMMA under an external heat flux has been classically studied in the literature on two main benches: the cone calorimeter (CC) [11, 12] and the fire propagation apparatus (FPA) [13, 14]. Both apparatuses serve as a way to study the behavior of materials such as the heat release, the ignition time, and the mass loss rate. Tests conducted in FPA and CC can yield different results. The decomposition process happening in the two apparatuses is different since the radiation coming from the two apparatuses is different. In fact, Bal [15], compared existing literature findings to examine potential differences arising from changes in experimental apparatus. They found that for clear PMMA, the majority of energy absorption occurred for wavelengths above $2\mu m$, corresponding to the emission wavelength of the CC. However, a different behavior was observed for wavelengths below $2\mu m$, the wavelength transmitted by the FPA, where clear PMMA transmitted the energy. This change in pyrolysis behavior highlights the importance of a thorough understanding of the radiative properties of the PMMA under investigation before concluding experimental results.

In conducting experiments using the cone calorimeter, *Luche et al* [16] found four primary

stages in the decomposition process of PMMA. Initially, when the PMMA sample is subjected to heat, it undergoes decomposition due to thermal stress, affecting a phase transition with the formation of a gaseous phase within the material. This gaseous phase manifests as a zone of bubbles, typically a few millimeters thick, proximate to the material's surface. As the temperature of the surface increases, the bubble zone diminishes in thickness, giving rise to progressively smaller bubbles. The viscosity decreases, facilitating the expulsion of gaseous pyrolysis products. Consequently, the decomposition of PMMA leads to complete depolymerization, yielding methyl methacrylate (MMA) [17] in the condensed phase. Swelling occurs due to the pressure exerted by the gaseous products, prompting the migration of bubbles toward the surface, ultimately augmenting the exposed surface area of the PMMA. This migration follows the path of least resistance and is primarily influenced by pressure and buoyancy gradients [18, 19]. Flammable gases are generated, which, under favorable conditions, combine with oxygen in the gas phase,and can create a diffusion flame above the sample. The radiative and convective fluxes of this flame can be combined with an external heat flux coming to the surface of the PMMA sample, thereby contributing to ongoing pyrolysis. This coupling mechanism during the second stage serves to perpetuate thermal decomposition and combustion, thereby illustrating the feedback loop between the material and the combustion process. The third stage, described by *Luche et al.*, is an artifact arising due to the cone calorimeter apparatus utilized. It is characterized by the thermal decomposition of the thin remaining layer of the PMMA sample after the initial stages. During this phase, swelling stops, and the decomposition rate is accelerated by the thermal feedback from the insulating plate of the sample holder used during cone calorimeter tests (ISO 5660). The mass loss rate peaks, subsequently decreasing as the remaining PMMA material decomposes, ultimately resulting in the extinguishment of the flame due to the absence of gaseous combustible. The decomposition ends with no PMMA residue in the sample holder.

The decomposition process of PMMA occurs under favorable ignition conditions, which necessitate a sufficient heat flux at the material's surface.

1.1.2 Critical Heat Flux (CHF) and ignition parameters

In the literature there were attempts to determine the critical heat flux to ignition. The CHF can be determined both experimentally and theoretically. Janssens [20] proposed a method to calculate the theoretical heat flux by plotting the inverse of the square root of the ignition time as a function of the external heat flux. The intercept of the plot with the x-axis constitutes the critical heat flux. However, *Luche et al* found that this method is not accurate in predicting the critical heat flux. The authors characterized black PMMA in a cone calorimeter and investigated the effect of the external heat flux on various parameters, including ignition time (Figure 1.1). *Luche et al* attempted to calculate additional thermal properties of the material and observed a linear evolution between the square root of the ignition time and the external heat flux. They found the theoretical critical heat flux (CHF) to be $4.8kW/m^2$, but the experimental one was measured to be $11kW/m^2$ showing the critical nature of this method. In particular, studies such as [21] and [20] propose methods for calculating the experimental critical heat flux using the theoretical critical heat flux.

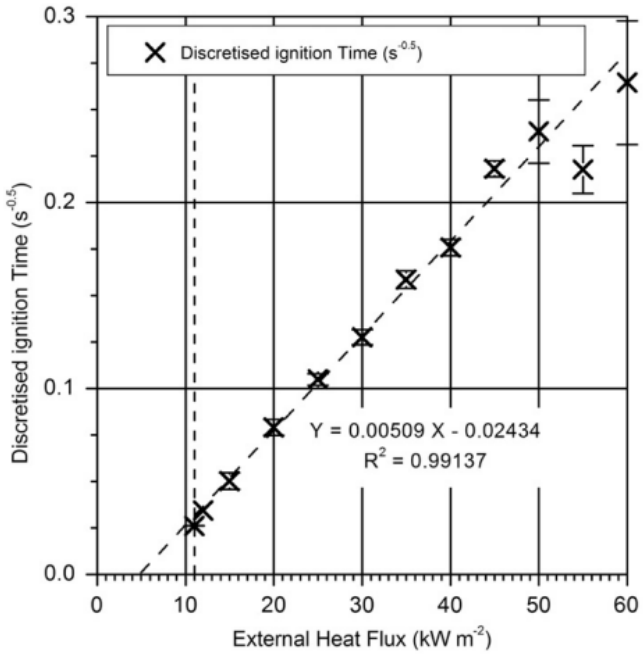

Figure 1.1: Square root of the inverse of ignition time as a function of heat flux from reference [16].

The critical heat flux can be calculated using ignition parameters such as the thermal response parameter (TRP) introduced by Tewarson [22]. For example, *Zarzecki et al* [23] conducted a study using $100 \times 100mm^2$ samples of PMMA in a large pressure vessel. The PMMA was under external heat fluxes ranging from 10 to $72kW/m^2$. The researchers used the TRP and the approach of Quintiere [24] to define the ignition time as shown in Equation 1.1.2, together with the TRP given in Equation 1.1.3.

$$t_{ig} = (\frac{TRP}{\dot{q}''_e})^2 \tag{1.1.2}$$

Where t_{ig} is the ignition time, TRP is the thermal response parameter, and $\dot{q}''_e$ is the external heat flux.

$$TRP = (\frac{\pi}{4} k\rho c_p)^4 (T_g - T_\infty) \tag{1.1.3}$$

Where ρ is the density, c_p is the specific heat at constant pressure, T_g is the gas temperature and T_∞ is the ambient temperature.

However, Zarzecki et al. argued that existing models, particularly those based on TRP, may not accurately predict ignition time as the external heat flux approaches critical levels. Their objective was to develop a model capable of predicting the ignition time at both high and low heat flux conditions. They introduced the critical heat flux (CHF) as defined by Equation 1.1.4, and established a correlation between CHF, $\dot{q}''_e$ and ignition time, illustrated in Equation 1.1.5.

$$CHF = \sigma(T_{ig}^4 - T_\infty^4) + h_c(T_{ig} - T_\infty) + \dot{q}''_{py} \tag{1.1.4}$$

Where σ is the Stefan–Boltzmann constant, T_{ig} is the temperature at ignition, h_c is the convective heat transfer coefficient and $\dot{q}''_{py}$ is the pyrolysis energy heat flux.

The study focused specifically at oxygen concentrations $X_{O2} = 0.21$ and the results are presented in Figure 1.2. In particular, the analytical model was based on a CHF value of $8.2kW/m^2$, calculated using Equation 1.1.4, and a TRP of 179, determined by fitting the ignition time data. The researchers found that the model performed well for lower heat

fluxes, but tended to underestimate ignition times for higher heat fluxes. The model was only compared to values obtained in air and did not include ignition times at lower oxygen concentrations.

$$\frac{CHF}{\dot{q}''_e} = 1 - exp(-\frac{CHF}{TRP})\sqrt{t_{ig}} \tag{1.1.5}$$

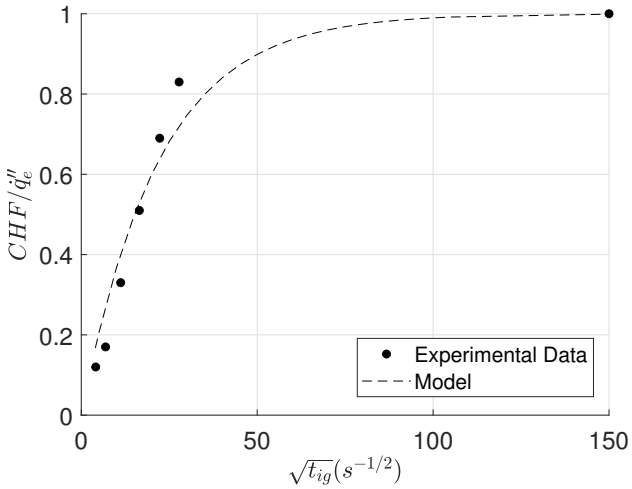

Figure 1.2: Ignition times normalized and plotted versus the external heat flux for $X_{O2} = 0.21$ given by [23], and the model given by Equation 1.1.2

.

In the existing literature, researchers have studied ignition delay time [25, 26, 27]. Additional models to predict the ignition time can be found in the literature such as the one in Equation 1.1.6. It is an analytical model developed by Rhodes and Quintiere [28]. They compared their experimental data, showing good agreement for heat fluxes under $40kW/m^2$. Based on their plot, they determined a theoretical critical heat flux of $4kW/m^2$.

$$t_{ig} = \frac{2}{3} k\rho c_p . \frac{(T_{ig} - T_\infty)^2}{\dot{q}''_{tot}} \tag{1.1.6}$$

This subsection showed attempts from the literature to find models able to predict the critical heat flux and the ignition time under air. The following subsection will focus on flame radiation and its effect on the PMMA.

1.1.3 Flame heat flux and flame temperature

During combustion, the decomposition process is continued by the heat flux receives at the surface of the sample. To measure this heat flux, several apparatuses in the literature are used. For example, Rhodes and Quintiere [28] used the experimental setup, illustrated in Figure 1.3, consisting of a hollow black PMMA sample equipped with a fluxmeter.

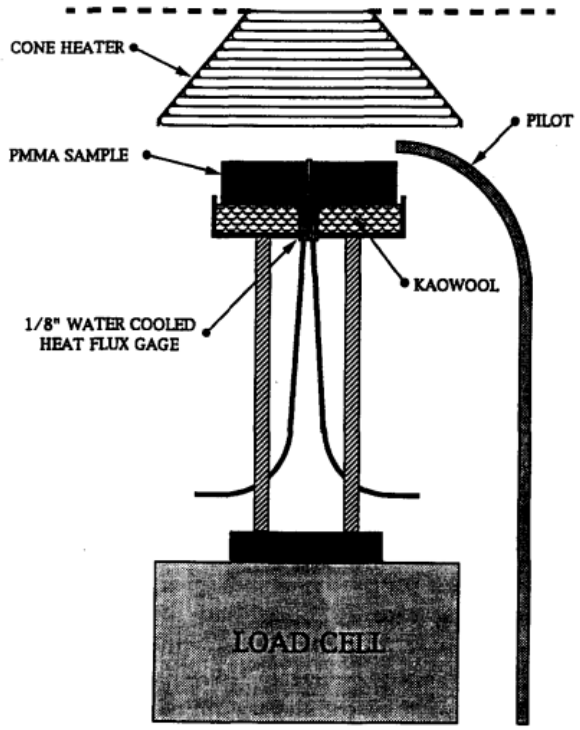

Figure 1.3: Apparatus used in reference [28].

Hopkins and Quintiere [29] investigated the flame heat flux at the PMMA sample surface using Schmidt-Boelter heat flux meters with diameters ranging from 6 to 25mm to measure the total heat flux coming from the flame. This measurement included both the radiative and convective components of the flame heat flux. To prevent interference, a thick ceramic material isolated the sample from the instrumentation, and the system included water cooling at 65°C.

Beaulieu and Dembsey [30] investigated the flammability of black cylindrical PMMA samples with diameters ranging from 105 to 1220mm, in both horizontal and vertical orientations.

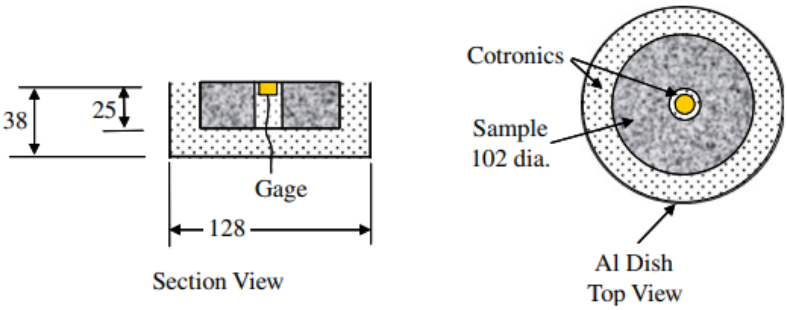

Figure 1.4: Experimental configuration for the measurement (in mm) of flame heat flux used in reference [30].

They used the advanced flammability measurement apparatus [31] and the experimental setup illustrated in Figure 1.4.

The flame heat flux is influenced by the dimensions of the sample in both vertical and horizontal orientation. In fact, *Orloff et al.* [32, 33] focused on large vertical PMMA samples with dimensions of $3560 \times 914 \times 64mm^3$ and $1570 \times 410 \times 45mm^3$. They found a flame heat flux ranging from 27 to $20kW/m^2$. In the vertical orientation, other literature references show similar results. *Pizzo et al.* in 2015 [34] investigated the surface heat flux for vertical clear PMMA samples of different heights. They found a flame heat flux ranging from 23.4 to $30.9kW/m^2$. *Kacem et al.* [35] carried out a series of tests using horizontally positioned translucent PMMA samples of different dimensions. The authors found a flame heat flux of $40.9kW/m^2$ for samples of dimensions $200 \times 200mm^2$ and $59.5kW/m^2$ for samples of dimensions $400 \times 400mm^2$. Similar results were observed by Alibert [36] on the same material where the flame heat flux varied from 24 for samples of dimensions $100 \times 100mm^2$ to $63kW/m^2$ for samples of dimensions $400 \times 400mm^2$. However, the flame heat flux does not seem to be dependant on the external heat flux as shown by Rhodes and Quintiere [28]. The authors found that the flame heat flux received at the surface of a horizontal PMMA sample remained constant at $37kW/m^2$ over a wide range of external heat fluxes ranging from 0 to $75kW/m^2$. This finding suggests that the flame heat flux for black PMMA is not dependent on the external heat flux.

The flame heat flux measured previously account for both radiative and convective compo-

nent. To be able to measure the radiative flux, *Kacem et al.* [35] placed a zinc selenide (ZnSe) pellet on top of the total flux meter. This approach allowed the isolation of the radiative contribution alone. ZnSe was chosen because it has near-zero absorption of radiation over a wide range of wavelengths. The results showed that the radiative contribution was up to 83% of the total heat flux. The radiative heat flux constitutes then a significant proportion of the total heat flux received at the surface of the sample. This method was also used later by Alibert [36] to the same end. The author found a radiative fraction of 65%.

Reference	**Sample Dimensions** (mm)	**Sample Orientation**	**Flame heat flux** (kW/m^2)
Orloff et al. [32]	$1570 \times 410 \times 45$ $3560 \times 914 \times 64$	vertical	20 27
Quintiere et al. [37]	280×280	vertical	$19.6 - 24$
Rhodes and Quintiere [28]	100×100 (black)	horizontal	37
Tsai and Wan [38]	1000×100 1000×300 1000×500 1000×700	vertical	23.58 23.95 30.04 30.21
Leventon and Stoliarov [39]	50×150	vertical	35 and 40
Beaulieu and Dembsey [30]	$diameter = 100$ $diameter = 178$ $diameter = 610$ $diameter = 1220$	horizontal	20 31 47 60
Pizzo et al. [34]	$height = 25$ $height = 200$	vertical	23.4 30.9
Kacem et al. [35]	200×200 400×400	horizontal	40.9 59.5
Alibert [36]	100×100 200×200 400×400	horizontal	24 36.5 63

Table 1.1: Values of flame heat flux during the combustion of PMMA in the literature

It is important to note that the studies include different experimental apparatus, which may contribute to certain discrepancies in the reported results.

A summary of some relevant literature values is given in Table 1.1, including measurements from different sample heights, configurations of both clear and black PMMA, and considering

both radiative and convective heat flux under ambient air conditions.

Although the flame can be characterised by its heat flux, another important factor to consider is the flame temperature. In the literature, the flame temperature has been recorded for different orientations and dimensions of the sample. The results are summarized in Table 1.2.

Reference	**Temperature** (K)
Orloff et al. [32]	1367
Beaulieu and Dembsey [30]	1184
Kacem et al. [35]	1190
Alibert [36]	$1080 - 1180$

Table 1.2: Values of flame temperature during the combustion of PMMA in the literature

Numerous studies have extensively investigated PMMA combustion under ambient conditions, as described above. However, the behavior of PMMA in under-oxygenated atmospheres can be subject to change. The following section provides a non-exhaustive review of the literature, summarising the results of studies of PMMA combustion in such environments.

1.2 Thermal behavior of PMMA under under-oxygenated atmospheres

The thermal decomposition of PMMA is highly dependent on ambient conditions, including external heat flux and oxygen concentration. To understand the behavior of this polymer in different scenarios, researchers have investigated the effect of oxygen concentration on both solid and gas phase parameters during PMMA combustion, such as mass loss rate, gas temperatures, and flame heat flux. The following section provides a review of several literature sources, beginning with the solid phase characteristics, followed by gas phase characteristics, and concluding with analytical models found in the literature to describe the behavior of PMMA in under-oxygenated atmospheres.

1.2.1 Solid-phase characteristics

This subsection is dedicated to present studies that focus on the solid-phase characteristics of the PMMA fire behavior in under-oxygenated atmospheres. The solid-phase characteristics include the effect of oxygen on the viscosity of the PMMA and the mass loss rate.

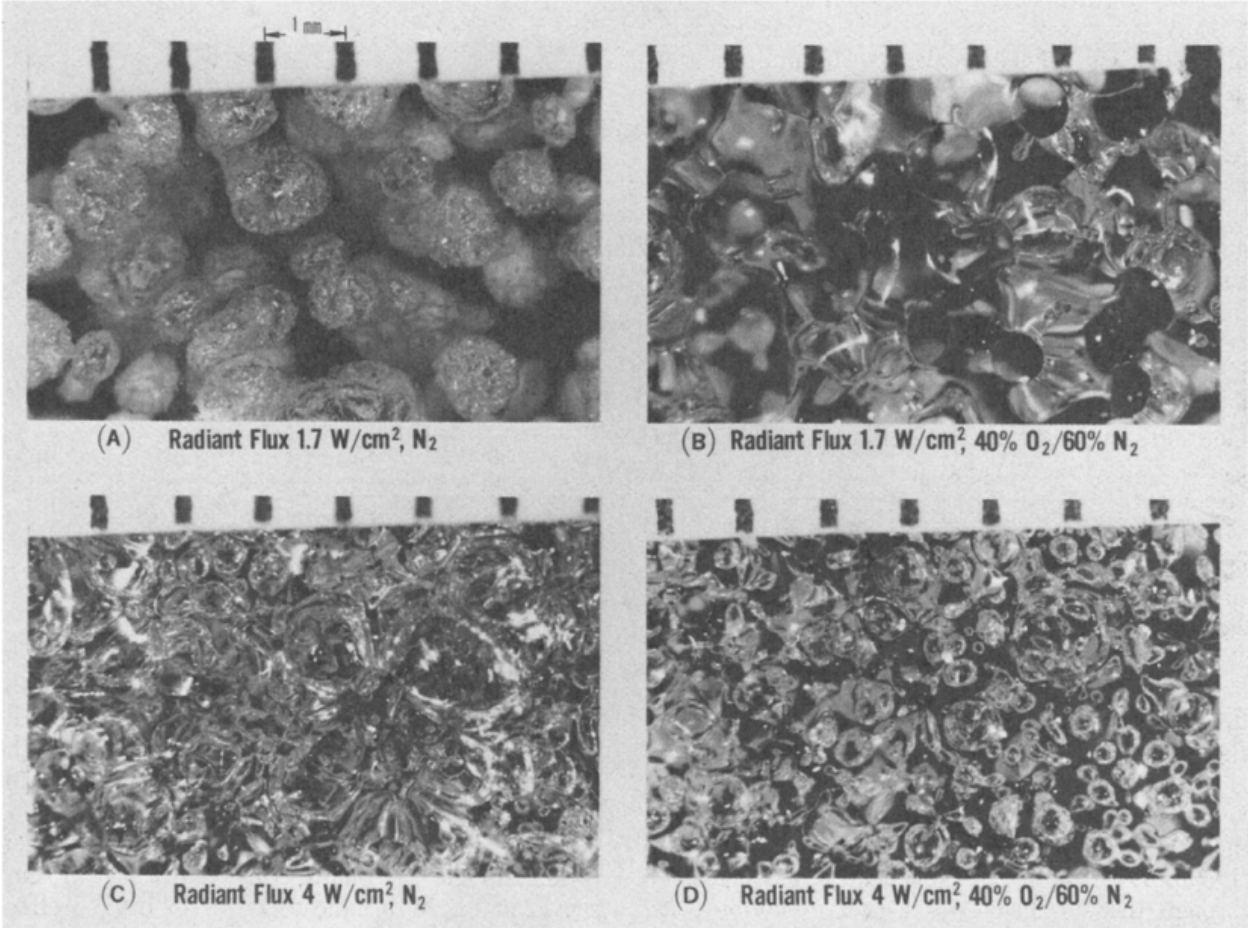

Figure 1.5: Microscope pictures of PMMA surface layers exposed to different radiant fluxes and environmental gases from reference [19]. The distance between two dark bars in the top part of each picture is 1 mm.

Kashiwagi and Ohlemiller [19] determined the effect of the ambient oxygen concentration on the rate of gasification and surface temperature of the PMMA. The oxygen concentrations varied from $X_{O2} = 0$ to $X_{O2} = 0.4$ under two heat fluxes of $10kW/m^2$ and $40kW/m^2$. The authors observed that in an environment with lower oxygen concentrations ($X_{O2} = 0$ and $X_{O2} = 0.10$), the hottest, near-surface layer of PMMA is characterized by the appearance

of large bubbles as shown in Figure 1.5. The presence of oxygen alters the behavior of the surface layer of PMMA. The surface layer becomes less viscous in environments with high oxygen concentrations ($X_{O2} = 0.4$). This promotes mass transfer of decomposition products from deeper layers to the surface by forming bubbles. This bubbling phenomenon affects the depth to which oxygen affects the surface. As the gasification rate increases, the effect of oxygen on the gasification process decreases. This diminishing effect is attributed to the counterflow of gases emanating from the surface of the material, which acts as a regulatory mechanism. It reduces the rate at which oxygen diffuses and is supplied to the condensed phase. The gasification process accelerates. The presence of oxygen also has a significant effect on the surface temperature of PMMA. An increase in the oxygen concentration leads to a significant decrease in the surface temperature of the material.

The mass loss rate of the material is heavily affected by the oxygen concentration. In fact, when the later decreased, the mass loss rate decreases too.

Santo and Tamanini [40] observed that the mass loss rate, showed a decrease from $12.9 g/ms$ to $9.2 g/ms$ as the oxygen volume fraction changed from 0.209 to 0.180.

Mulholland et al. [41] carried out a study of thin PMMA samples measuring $100 \times 100 \times 6 mm$. Their experiments took place in a controlled atmosphere cone calorimeter and the samples were subjected to two different external heat flux conditions: $\dot{q}''_e = 15$ and $30 kW/m^2$. They observed a decrease in the mass loss rate at both external heat fluxes. This decrease is evident as the oxygen concentration decreased, from $25 g/s.m^2$ at $X_{O2} = 0.21$ to $15 g/s.m^2$ at $X_{O2} = 0.14$ for $\dot{q}''_e = 30 kW/m^2$. Similarly, for $\dot{q}''_e = 15 kW/m^2$ the mass loss rate decreases from $5.3 g/s.m^2$ at $X_{O2} = 0.21$ to $3 g/s.m^2$ at $X_{O2} = 0.15$. This study's normalized mass loss rate ratios are later compared with values from other literature sources in this section (see Figure 1.10). The combined influence of heat flux and oxygen concentration results in a significant reduction in the specific mass loss rate, reaching a minimum value of $3 g/s.m^2$.

In 2019, Chatenet [42] realized a series of experiments using the Mass Loss Rate Calorimeter. This standardized apparatus (ISO 13927) is described in detail in [43]. This calorimeter is a modified version of the cone calorimeter that uses a thermopile at the top of the stack to measure the heat release rate, unlike the traditional oxygen consumption method. Chatenet's

investigation focused on determining the Peak Mass Loss Rate (pMLR) under varying oxygen concentrations (Table 1.3). The results show a noticeable decrease in the pMLR as the oxygen concentration decreases. The pMLR decreased from $0.284 g/s$ at $X_{O2} = 0.21$ to 0.232 at $X_{O2} = 0.13$, which is close to the observed limiting concentration reported by the author. Subsequent tests at $X_{O2} = 0.09$, $X_{O2} = 0.06$ and $X_{O2} = 0.02$ show a transition to the non-flaming mode. During this phase, the pMLR is almost constant. This observation is consistent with the findings of *Marquis et al.* [44].

X_{O2}	$pMLR(g/s)$
0.21	0.284
0.18	0.264
0.16	0.246
0.13	0.232
0.09	0.18
0.06	0.173
0.02	0.175

Table 1.3: Values of peak MLR for several oxygen concentrations from reference [42].

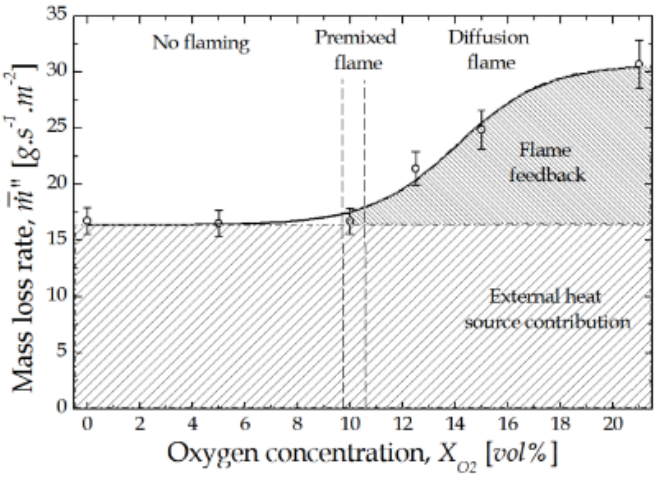

Figure 1.6: Specific mass loss rate values for several oxygen concentrations from reference [45].

Their results for Specific Mass Loss Rate (SMLR) for black PMMA, are presented in Figure 1.6. In both studies, the SMLR shows a decreasing pattern in the flaming region and

becomes constant in the non-flaming region. Thus, the literature shows that the oxygen concentration considerably affects the behavior of the PMMA in its solid phase. The surface layer of the PMMA becomes more viscous with the decreasing oxygen which affects the mass transfer of decomposition products to the surface. The oxygen concentration in turn affects the mass loss rate material which decreases with the decreasing of oxygen.

1.2.2 Gas phase characteristics

In this subsection, studies discussing the gas phase characteristics are presented. The gas phase characteristics include the emittance, the flame heat flux, and the heat release rate. The flame morphology is subject to change with the oxygen concentration. Santo and Tamanini [40] found that the flame dimensions such as diameter and height decrease with the oxygen concentration. For lower oxygen concentrations, the flame height also decreases, with a smaller diameter.

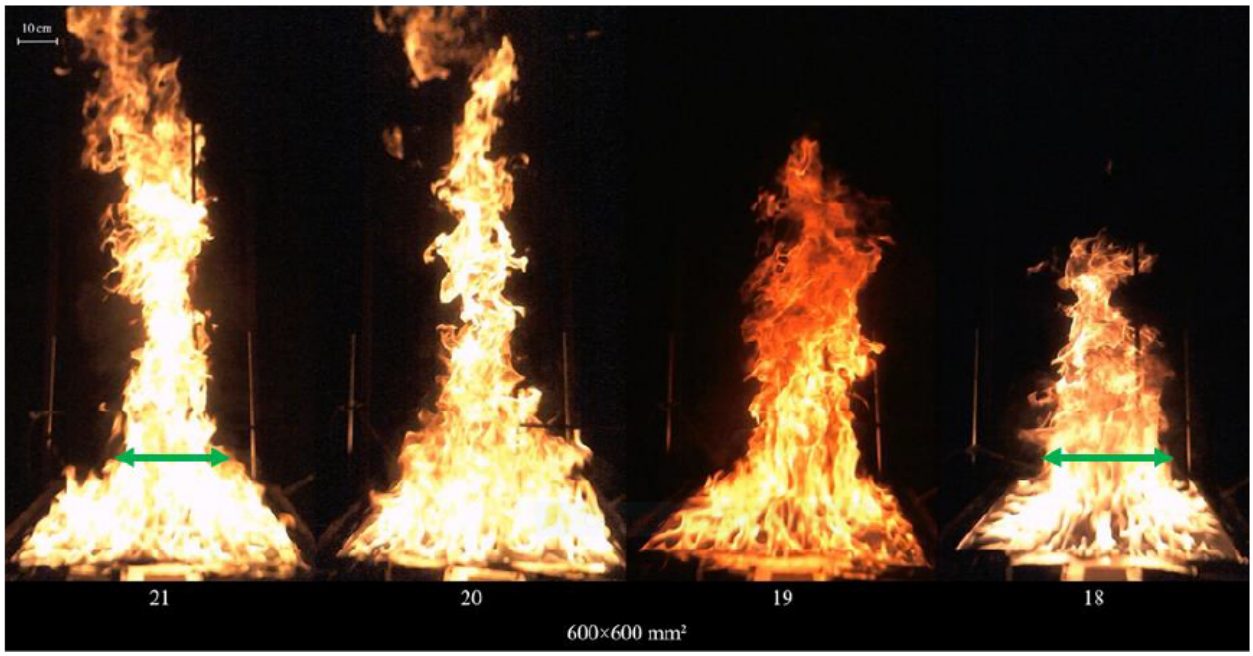

Figure 1.7: Instantaneous pictures of the flames generated by the combustion of the PMMA from reference [36]

This behavior was also observed by Alibert [36]. The author presented pictures of the flame resulting from the combustion of clear PMMA samples of surface $600 \times 600 mm^2$.

As shown in Figure 1.7, the oxygen concentrations varies from $X_{O2} = 0.18$ to $X_{O2} = 0.21$. The flame diameter increases with decreasing oxygen, accompanied by a decrease in flame height. A noticeable change in the color of the flame is observed, appearing bright yellow under normal air conditions and changing to a more orange-yellow hue as the oxygen concentration decreased. This shows that the flame morphology is directly linked to the oxygen concentration present in the ambient environment. The flame heat flux has been found to decrease with the oxygen concentration. In particular, Alibert [36] observed total heat flux at the surface of PMMA samples with dimensions of $200 \times 200mm^2$ and $400 \times 400mm^2$. They found values of 40.9 and $59.5kW/m^2$ under ambient air conditions. Tests carried out at different oxygen concentrations show a decrease in heat flux with increasing oxygen concentration.

X_{O2}	χ_r
0.209	0.36
0.199	0.33
0.190	0.29
0.180	0.25

Table 1.4: Influence of the oxygen fraction on the radiative fraction from reference [40].

The measurement of the radiative flame heat flux has been the subject of interest in several studies. It is also found to decrease with the oxygen concentration. Santo and Tamanini [40] found a correlation between oxygen concentration and the radiative fraction, denoted χ_r. Under normal air conditions, this fraction is measured to be 0.36, but as the oxygen concentration decreased to $X_{O2} = 0.18$, it falls to a value of 0.25. This trend is shown in Table 1.4. Similar trends are observed in other flame properties such as absorption coefficient, emittance, and total radiation. These parameters show a consistent decrease with decreasing oxygen concentration, due to a reduction in soot production and to an increase in flame dimension as oxygen levels increased. A similar behavior was found by *Tewarson et al.* [1]. The researchers used Spalding's B-number and a surface heat balance analysis to estimate the convective and radiative heat flux in flames. This investigation focused on a range of oxygen concentrations, between $X_{O2} = 0.16$ and $X_{O2} = 0.46$. They noticed an increase in

flame radiation with the increase in oxygen concentration. However, the flame convection decreases.

The flame temperature follows the same trend as the heat flux as it decreases with the oxygen concentration. However, while Alibert [36] identified a linear correlation between gas temperatures and oxygen fraction, ranging from $X_{O2} = 0.18$ to $X_{O2} = 0.21$, Santo and Tamanini [40] found that the flame temperature stayed constant as the oxygen decreased.

Another parameter to consider in the gas phase is the heat release rate which also decreases with the oxygen concentration. This was observed for instance in the work of *Mulholland et al.* [41] and Chatenet [42]. *Mulholland et al.* [41] found that heat release rate show a decrease from $6.5kW$ under ambient conditions to $3.7kW$ at $X_{O2} = 0.14$. Chatenet [42] provided data on peak heat release rate (pHRR) and total heat release (THR), as shown in Table 1.5. The reported values show a decreasing trend for both pHRR and THR as oxygen concentrations decreased. The highest values of pHRR reported under air is $489kW/m^2$ and the THR is $130MJ/m^2$. Those values drop to $386kW/m^2$ for the pHRR and $113MJ/m^2$ for the THR at $X_{O2} = 0.16$. At an oxygen concentration of $X_{O2} = 0.13$, the authors refrained from reporting values due to the non-repeatability of the results, indicating getting close to the limiting oxygen concentration. At oxygen concentrations lower than $X_{O2} = 0.13$, where there is no flame, both pHRR and THR are negligible.

X_{O2}	$pHRR(kW/m^2)$	$THR(MJ/m^2)$
0.21	489	130
0.18	451	127
0.16	386	113
0.13	No repeatable results	No repeatable results
0.09	/	/
0.06	/	/
0.02	/	/

Table 1.5: Values of pHRR and THR for several oxygen concentrations from reference [42].

This subsection showed that the gas phase characteristics such as the heat release, the flame morphology, and the flame heat flux are affected by the oxygen concentration in the ambient

air. The previous studies conducted experiments with decreasing oxygen concentration until no flame was observed.

1.2.3 Extinction

This section is focusing on studies about extinction. It will discuss the limiting oxygen index, and the Damköhler number, which is a metric related to extinction and extinction time.

Damköhler number

Flame extinction, as defined by *Maragkos et al.* [46], is when the chemical reaction rate falls below a critical value that renders self-sustaining combustion unattainable. This phenomenon is governed by three mechanisms [47]: aerodynamic quenching, thermal quenching, and dilution quenching. Each of these mechanisms causes extinction by interfering with a critical component that affects its sustained combustion. Aerodynamic quenching induces a rapid flow disturbance, resulting in a critical reduction in flame residence time. Thermal quenching, the second mechanism, extinguishes the flame by significant heat loss. Dilution quenching, the third mechanism, extinguishes the flame by changing the composition of the fuel or oxidizer. To evaluate these quenching mechanisms, a unified criterion known as the Damköhler number has been introduced [48, 49, 50] and is defined by Equation 1.2.1. The Damköhler number serves as a metric that provides a standardized measure to evaluate the three extinction methods.

$$Da = \frac{t_{mixing}}{t_{chemical}} \tag{1.2.1}$$

When Da is lower than a critical number, the mixing time t_{mixing} becomes shorter than the characteristic chemical time $t_{chemical}$, which represents the required duration for the chemistry reaction to take place, the combustion becomes unsustainable and $Da << 1$ [51]. In under-oxygenated atmospheres, extinction happens when the oxidizer is no longer sufficient. In the following section, studies focusing on the extinction times will be discussed as well as the effect the oxygen concentration has on them.

Limiting oxygen concentration and extinction times

This subsection focuses on the limiting oxygen concentration and the extinction times. The limiting oxygen concentration is the concentration at which no ignition happens. It can be affected by factors such as the external heat flux.

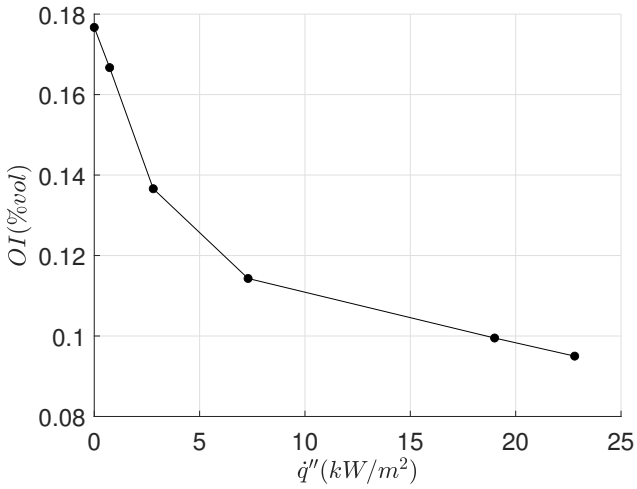

Figure 1.8: Influence of external radiant heat flow upon the oxygen index of the PMMA as found by [52].

With the decrease of the heat flux the limiting oxygen concentration increases in a hyperbolic pattern. This trend was showed by Zhubanov and Gibov [52] on the PMMA.

Decrease in oxygen concentration $\times 10^{-2}(vol)$	Time to extinction (s)
0.5	150
1	95
2	50
3	30
4	15
4	15
5	2

Table 1.6: Influence of the oxygen concentration on the extinction time in [52]

They used hollow cylinders with an external diameter of $10mm$ and an internal diameter of $3.2mm$. To initiate combustion, a polymeric sample was heated by a $NiCr$ spiral and

then removed. The combustion was maintained by the system. As shown in Figure 1.8, they observed that the relationship between the oxygen index and the external heat flux show a hyperbolic pattern. In particular, the oxygen index show lower values at higher heat fluxes, while it show an increase at lower heat fluxes. They also observed that at lower oxygen concentrations, extinction is almost instantaneous. In contrast, when the oxygen concentration is higher, combustion continues, lasting a few minutes (Table 1.6). While the ignition method may not have a direct impact on the ignition times, the presence of external heat flux could. In fact, Tewarson and Pion [14] used various ignition methods, including a match flame, heptane ignited by a match flame, a propane air torch, and the ignition of plastic shavings, n-pentane, and paraffin oil by a match flame to ignite commercial PMMA and concluded that the ignition methods has no discernible effect on the ignition results. However, their results indicated that PMMA extinction occurs at an oxygen concentration of $X_{O2} = 0.17$. This observation leads to the consideration that the methodology involving the absence of an external heat flux may have contributed to the lack of combustion at oxygen concentrations lower than $X_{O2} = 0.17$. Alibert [36] did not observe any ignition for $X_{O2} = 0.18$ which is a value close to the one of close to Tewarson and Pion. The author used the Controlled Atmosphere Device for Unburnt and Carbon Emission Evaluation (CADUCEE). The device consists of a combustion chamber, an octagonal stainless steel enclosure with a volume of approximately $22m^3$, positioned above the oxidizer chamber and below the extraction hood. The ignition procedure involved grooving the top surface of the PMMA sample and filling it with ethanol, which was then ignited. The oxygen concentration was kept constant at $X_{O2} = 0.21$ for some time. This duration ensured the complete combustion of ethanol in a normal atmosphere, resulting in the even coverage of the upper surface of the sample by the flame. As observed in [14], the absence of an external heat flux can be the reason why ignition does not happen at an oxygen concentration lower than $X_{O2} = 0.18$. In parallel, *Mulholland et al.* [41] and Chatenet [42] did not observe ignition for values under respectively $X_{O2} = 0.14$ and $X_{O2} = 0.13$ which are much lower than the values of [36] and [14]. This shows that the external heat flux has a major impact on the limiting oxygen concentration.

This subsection shows that the limiting oxygen concentration is impacted by the presence of an external heat flux. It increases in a hyperbolic trend with the decrease of the external heat flux. The extinction time is affected by the oxygen concentration and decreases with the latter.

1.2.4 Analytical models under under-oxygenated conditions

The previous subsection discussed experimental results on various parameters for the combustion of PMMA. In the literature, researchers attempted to come up with analytical models to illustrate those experimental results and being able to predict them. The following section focuses on the different analytical models developed in the literature to describe the thermal behavior of different fuels during a fire.

The mass loss rate, during the steady burning, can be found by doing an energy balance as shown in Figure 1.9 at the surface of the sample Equation 1.2.2.

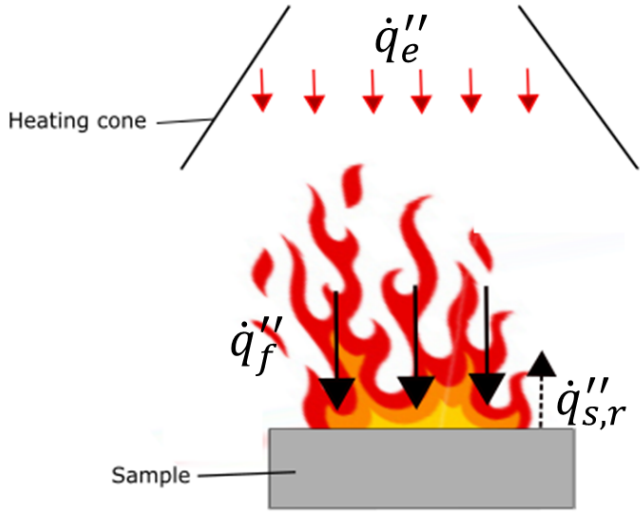

Figure 1.9: Heat balance at the surface of the sample.

$$\dot{m}'' = \frac{\dot{q}''_f + \dot{q}''_e - \dot{q}''_{s,r}}{L_G} \tag{1.2.2}$$

Where $\dot{m}''$ is the specific mass loss rate, $\dot{q}''_f$ is the flame heat flux, $\dot{q}''_e$ is the external heat flux, and $\dot{q}''_{s,r}$ is the radiative losses at the surface.

According to Drysdale [53] the flame heat flux can be divided into three heat fluxes: a conductive heat flux $\dot{q}''_{f,cond}$ Equation 1.2.3, a convective one $\dot{q}''_{f,c}$ Equation 1.2.4, and a radiative one $\dot{q}''_{f,r}$ Equation 1.2.5.

$$\dot{q}''_{f,cond} = \frac{4K_{cond}}{D}(T_f - T_s) \tag{1.2.3}$$

$$\dot{q}''_{f,c} = h_c(T_f - T_s) \tag{1.2.4}$$

$$\dot{q}''_{f,r} = \frac{4K_r}{\pi D^2}(T_f^4 - T_s^4)(1 - \exp -\kappa D) \tag{1.2.5}$$

Where K_{cond} is the conduction constant, D is the equivalent diameter of the surface, h_c is the convection coefficient, T_f is the flame temperature, T_s is the temperature at the surface, K_r is a radiative constant taking into account the Stefan-Boltzmann constant and the view factor, and κ is the extinction coefficient.

The radiative losses $\dot{q}''_{s,r}$ are given by Equation 1.2.6

$$\dot{q}''_{s,r} = \epsilon\sigma(T_s^4 - T_\infty^4) \tag{1.2.6}$$

In light of the previous equations, the mass loss rate is given by Equation 1.2.7.

$$\dot{m}'' = \frac{1}{L_G}[\frac{4K_{cond}}{D} + h)(T_f - T_s) + \frac{4K_r}{\pi D^2}(T_f^4 - T_s^4)(1 - e^{-\kappa D}) + \dot{q}''_e - \epsilon\sigma(T_s^4 - T_\infty^4)] \tag{1.2.7}$$

Correlation of Tewarson and Pion for the mass loss rate

In the aim of defining the mass burning rate of plastics, Tewarson and Pion investigated as documented in [14]. They aimed to determine the mass loss rate at the surface of plastic samples, a critical parameter in understanding flammability characteristics. Using a heat

balance approach, they introduced the specific mass loss rate, denoted $\dot{m}''$, expressed by Equation 1.2.2. They found experimentally that the flame heat flux can be expressed as Equation 1.2.8.

$$\dot{q}''_f = \gamma . X_{O2} \tag{1.2.8}$$

Where γ is a fitted constant and X_{O2} is the molar fraction of oxygen. They conceptualized an ideal scenario where the heat flux lost at the surface is equal to the external heat flux. This ideal burning rate is defined by Equation 1.2.9 and the actual burning rate is represented by Equation 1.2.10.

$$\dot{m}''_{ideal} = \frac{\gamma}{L_G} . X_{O2} \tag{1.2.9}$$

$$\dot{m}'' = \dot{m}''_{ideal} + \frac{\dot{q}''_e - \dot{q}''_{s,r}}{L_G} \tag{1.2.10}$$

Correlation of Peatross and Beyler for the mass loss rate

Peatross and Beyler [54] conducted experiments in a large enclosure under forced and natural ventilation on diesel, wood, and polyurethane. They argued that the mass loss rate per unit area varies significantly for each fuel, and they came up with a new representation for the mass loss rate to help account for those differences. A key aspect of their approach is to normalize the mass loss rate by its corresponding value under ambient air conditions. They used data derived from their experiments as well as supplementary information from the studies of Tewarson et al. [1] and Santo and Tamanini [40]. By assimilating and synthesizing these datasets, Peatross and Beyler created a linear correlation model, detailed in Equation 1.2.11.

$$\frac{\dot{m}''_{O2}}{\dot{m}''_{air}} = AX_{O2} + B \tag{1.2.11}$$

Where $A = 10$ and $B = -1.1$. Based on this approach, Alibert [36] compared their values to the correlation of Peatross and Beyler in Figure 1.10 and it showed a good fit. The data for the PMMA and different studies are shown in and compared to the Peatross and Beyler correlation, showing all a good fit expect for the values of *Mulholland et al.* [41]. The correlation given by Peatross and Beyler is based on experimental results with no or low external heat flux at the surface of the sample. However, in their study, *Mulholland et al.* maintained a constant external heat flux of 30 or $15 kW/m^2$. The added external heat flux could be the reason for the deviation of the specific mass loss rate ratio data. Chatenet [42] explained this difference incident heat flux. Radiative heat flux, a key component of total heat transfer, is closely linked to flame emissivity. Emissivity is in turn influenced by factors such as soot volume fraction, soot absorption coefficient, and partial pressure of gas compounds. This provides an explanation for the observed decrease in mass loss rate (MLR) that would become consistent with the correlation established by Peatross and Beyler.

Model of Utiskul for the mass loss rate

Utiskul [55] developed a theoretical model for the burning rate based on the approach of Quintiere [56] [57] which aims to predict the burning rate under under-oxygenated atmospheres using the Saplding B-number. The authors define a control volume of thickness γ at the gas-solid interface of the sample. They consider a unidimensional problem following the axis y perpendicular to the surface of the sample. The conservation equations can be applied to the layer.

- Conservation of Mass

$$\frac{d}{dy}(\rho V) = 0 \tag{1.2.12}$$

- Conservation of species

$$\frac{d}{dy}(\rho V Y_i) = \frac{d}{dy(\rho D \frac{dY_i}{dy}) + \dot{m}_i'''} \tag{1.2.13}$$

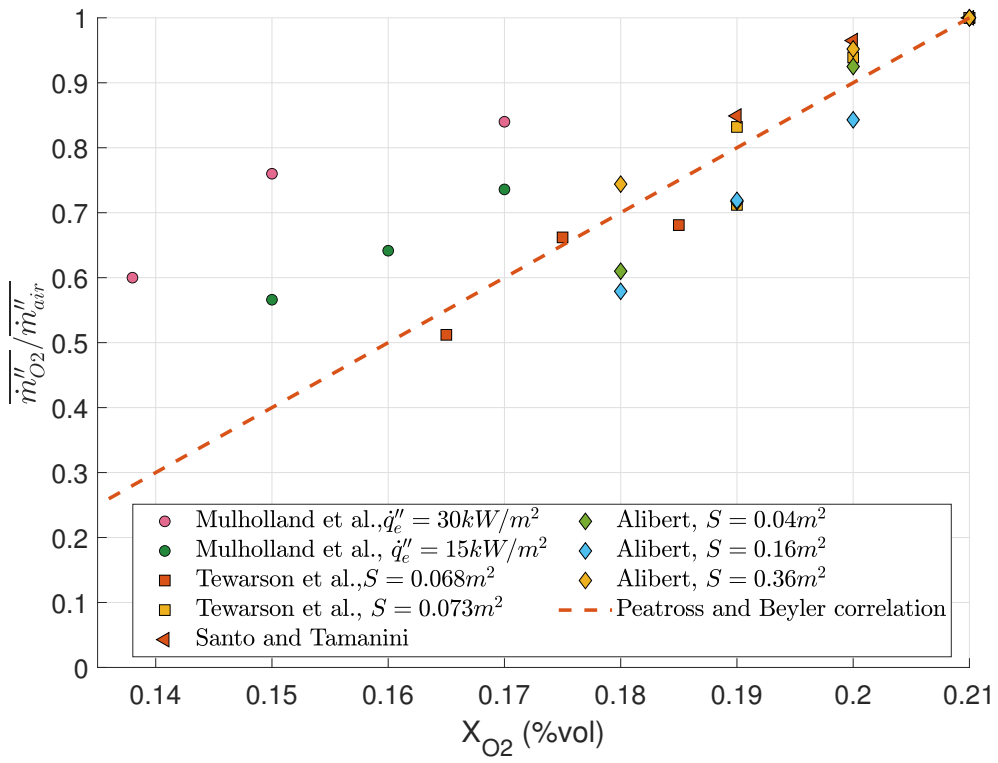

Figure 1.10: Specific mass loss rate data for the PMMA from [41], *Tewarson et al.* [1], Santo and Tamanini [40], Peatross and Beyler [54] and Alibert [36].

.

- Conservation of energy

$$c_p \frac{d}{dy}(\rho \nu T) = \frac{d}{dy}(K_{cond} \frac{dT}{dy}) + \dot{m}''' \Delta H_c \tag{1.2.14}$$

- Conservation of momentum

$$\frac{dP}{dy} = 0 \tag{1.2.15}$$

For the following calculations, a few assumptions are taken:

1. A simple chemical reaction with a single product as follows is considered:

   $(1kg)F + (r.kg)O_2 \longrightarrow (r+1)kgP$

   Where F is the fuel, P are the products, and r is the stoichiometric ratio air/fuel.

2. The flame radiative heat flux is assumed to be negligible and only the convective heat

flux is considered.

3. The specific heat c_p is considered constant
4. A laminar, unidirectional flow is considered following the y direction.
5. The properties used are constant and independent of the temperature.

Integrating Equation 1.2.12 leads to Equation 1.2.16.

$$\dot{m}'' = \rho V = constant \tag{1.2.16}$$

Equation 1.2.16 shows that for $y = 0$ the mass loss rate is the mass loss rate of the vaporized fuel.
Equation 1.2.15 shows that the pressure is constant throughout the axis y giving Equation 1.2.17.

$$p(y) = p_\infty \tag{1.2.17}$$

The energy conservation equation Equation 1.2.14 becmes Equation 1.2.18, and the species conservation equation Equation 1.2.13 becomes Equation 1.2.19.

$$c_p \dot{m}'' \frac{dT}{dy} - K_{cond} \frac{d^2T}{dy^2} = \dot{m}''' \Delta H_c \tag{1.2.18}$$

$$\dot{m}'' \frac{dY_i}{dy} - \rho D \frac{d^2Y_i}{dy^2} = \begin{cases} -\dot{m}''' & \text{if } i = F \\ -r.\dot{m}''' & \text{if } i = O_2 \\ (r+1)\dot{m}''' & \text{if } i = P \end{cases} \tag{1.2.19}$$

The boundary conditions are given at:

- The surface of the sample ($y = 0$)

$$\begin{aligned} T &= T_s \\ Y_{O2} &= 0 \\ Y_p &= 0 \\ Y_F &= Y_{F,0} \end{aligned} \tag{1.2.20}$$

- The interface of the flow of oxygen ($y = \gamma$).

$$\begin{aligned} T &= T_\infty \\ Y_{O2} &= Y_{O2,\infty} = 0.23 \\ Y_p &= Y_{p,\infty} = 0 \\ Y_F &= 0 \end{aligned} \tag{1.2.21}$$

The convective heat flux being the only heat flux at the surface of the sample, Equation 1.2.22 is deduced.

$$\dot{m}'' L_G = \left(K_{cond} \frac{dT}{dy} \right)_{y=0} \tag{1.2.22}$$

The resolution of the system leads to Equation 1.2.23.

$$\dot{m}'' = \frac{h_c}{c_p} ln(1 + B) \tag{1.2.23}$$

Where B is the Spalding number [58] given by Equation 1.2.24.

$$B = \frac{Y_{O2,\infty} \frac{\Delta H_c}{r} - c_p(T_s - T_\infty)}{L_G} \tag{1.2.24}$$

If the radiative heat flux at the surface of the sample was taken into account, a new parameter is introduced. The modified heat of gasification L_m defined by Equation 1.2.25.

$$L_m = L_G - \frac{\dot{q}''_{f,r} + \dot{q}''_{e,r} - \sigma(T_s^4 - T_\infty^4)}{\dot{m}''} \tag{1.2.25}$$

The Spalding number then becomes Equation 1.2.26.

$$B = \frac{Y_{O2,\infty}\frac{\Delta H_c}{r}(1 - X_r) - c_p(T_s - T_\infty)}{L_m} \tag{1.2.26}$$

Based on the previous approach, Utiskul [55] defined the convective heat flux of the flame Equation 1.2.27 using the Spalding number B from Equation 1.2.26.

$$\dot{q}''_{f,c} = \frac{h_c}{c_p}\left[\frac{ln(1+B)}{B}\right](Y_{O2,\infty}\frac{\Delta H_c}{r}(1 - X_r) - c_p(T_s - T_\infty)) \tag{1.2.27}$$

This model was specifically formulated for confined spaces characterized by a reduced mass fraction of oxygen. In this context, Utiskul states that the numerical value represented by B is relatively small, leading to a convergence of the ratio $\frac{\ln(1+B)}{B}$ towards 1. The total heat flux of the flame becomes Equation 1.2.28.

$$\dot{q}''_f = \frac{h_c}{c_p}\frac{\Delta H_c}{r}(1 - X_r)Y_{O2,\infty} - c_p(T_s - T_\infty) + \dot{q}''_{f,r} \tag{1.2.28}$$

The radiative component of the flame heat flux $\dot{q}''_{f,r}$, can be neglected due to its reduction with decreasing oxygen concentration in a horizontal configuration, as established by [40] [1]. Consequently, Equation 1.2.28 illustrates a direct proportionality between $\dot{q}''_f$ and $Y_{O2,\infty}$. Utiskul further asserts that the total heat flux $\dot{q}''_{tot}$, is also proportional to $Y_{O2,\infty}$. This relationship holds even under ambient air conditions, where $\dot{q}''_{tot,air}$ has a similar proportionality to $Y_{O2,air}$, as shown in Equation 1.2.29.

$$\frac{\dot{q}''_{tot}}{\dot{q}''_{tot,air}} = \frac{Y_{O2,\infty}}{Y_{O2,air}} \tag{1.2.29}$$

Whith $\dot{q}''_{tot,air} = \dot{m}''_{air}.L_G$.

The previous equation leads to the correlation of mass loss rates given by

$$\dot{m}'' = \dot{m}''_{air} \frac{Y_{O2,\infty}}{Y_{O2,air}} + \frac{\dot{q}''_e}{L_G} \tag{1.2.30}$$

Model of Quintiere for the flame temperature

In 1993, Quintiere [24] introduced a predictive model for flame temperature, as outlined in Equation 1.2.31.

$$\frac{T_f - T_\infty}{T_\infty} = C_{T,f}(1 - X_r)(\frac{Y_{O2}\Delta h_c}{r c_p T_\infty}) \tag{1.2.31}$$

Where $C_{T,f} = 0.5$ for $c_p = 1kJ/kgK$ and the radiative fraction X_r affected by the oxygen concentration.

1.3 Conclusion

This first chapter is dedicated to the state of the art of the influence of the oxygen concentration on the thermal decomposition and the combustion of the PMMA, both considering the solid, the gas phases and the coupling between these two. The literature review shows that the combustion parameters are influenced by the oxygen concentration and the external heat flux. In the solid phase, the mass transfer is impacted by the PMMA's surface layer becoming more viscous when oxygen levels drop. The mass loss rate material is influenced by the concentration of oxygen and decreases as oxygen levels drop. The oxygen content of the surrounding air has an impact on the gas phase properties, including heat release rate, flame shape and flame heat flux. Additionally, the limiting oxygen concentration is impacted by the external heat flux. Despite the number of experimental data available for flame temperature under air and relatively high oxygen concentrations, there is a significant gap in understanding the behavior of different combustion parameters at lower oxygen concentrations. The rarity of data in this critical range shows the need for further investigation. Moreover, the literature shows a large discrepancy into the values of parameters studied. This is why, the current study focuses on experimental data for several oxygen concentrations and heat flux, in an attempt to fill this gap. The next chapter will present

the experimental setup and protocol used in the study and the different measurements made.

CHAPTER 2

EXPERIMENTAL SETUP

Table of Contents

The state-of-the-art review highlighted the need for combustion data for a wider range of oxygen concentrations, especially lower ones. The present study uses PMMA samples in the controlled atmosphere cone calorimeter. Some modifications have been made to this bench to allow the measurement of several parameters such as the gas temperatures and in-sample heating rate. The following chapter focuses on the experimental setup and protocol used, as well as the measurements done.

2.1 Material

The material used in this study is a non-charring transparent poly(methyl methacrylate)(PMMA) shown in Figure 2.1 obtained by casting from IRPEN. This polymer does not contain any inert charges, flame retardant or fillers. The composition of this PMMA is unknown; however, it is possible to find data for similar products [16].

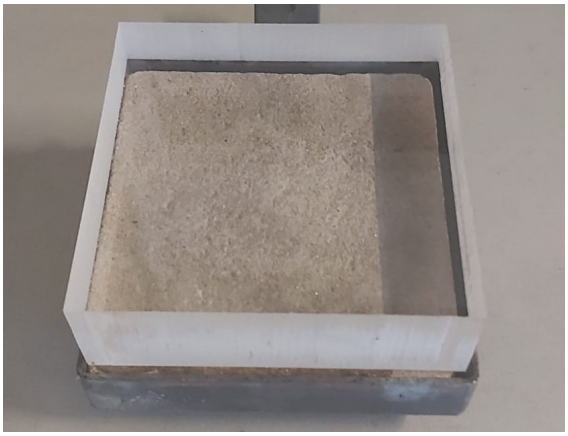

Figure 2.1: Sample of the poly(methyl methacrylate) (PMMA) studied into the cone calorimeter sample holder

Chemical formula	$C_5H_8O_2$
Density (kg/m^3)	1183 (current study)
Thermal conductivity $(W/m.K)$	0.176 [35]
Specific heat $(J/kg.K)$	1680 [59]
Refractive index	1.5 [34]
Auto-inflammation heat flux (kW/m^2)	25-30 [28]

Table 2.1: Properties of the PMMA studied

The behavior of the PMMA used in this thesis has also already been studied on a larger specimen in the references [35] and [36]. The specimens are of dimensions $100 \times 100mm^2$ with a thickness of $30mm$. The properties of the material are summarized in Table 2.1. Before the test, the specimens were conditioned at (23 ± 2) and $(50 \pm 5)\%$ relative humidity for more than 88 hours, in compliance with ISO 291 [60].

2.2 The controlled atmosphere cone calorimeter

The experiments were performed using the controlled atmosphere cone calorimeter (CACC) shown in Figure 2.2, which is a variation of the cone calorimeter (CC) described in ISO 5660-1 [61]. A schematic of this experimental device is shown in Figure 2.3. It is designed to investigate the impact of an oxygen deprived environment on the burning characteristics of solid matter under varying levels of external heat flux. The CACC consists of a standard

truncated conical heater positioned at the top of a stainless steel chamber ($38 \times 32 \times 35 cm^3$). At the basis of the enclosure, two gas inlets equipped with two Bronkhorst mass flow meters allow the control of the air/nitrogen mixture inside the enclosure ($X_{O_2} \in [0 - 21]\%vol$). Their characteristics are presented in Table 2.2.

Type	Flow controller (D)
Fluid	Air or Nitrogen
Flow	$100 L/min$ or $200 L/min$
Pressure	4.0 bars
Temperature	$20°C$

Table 2.2: Characteristics of the two Bronkhorst flowmeters used

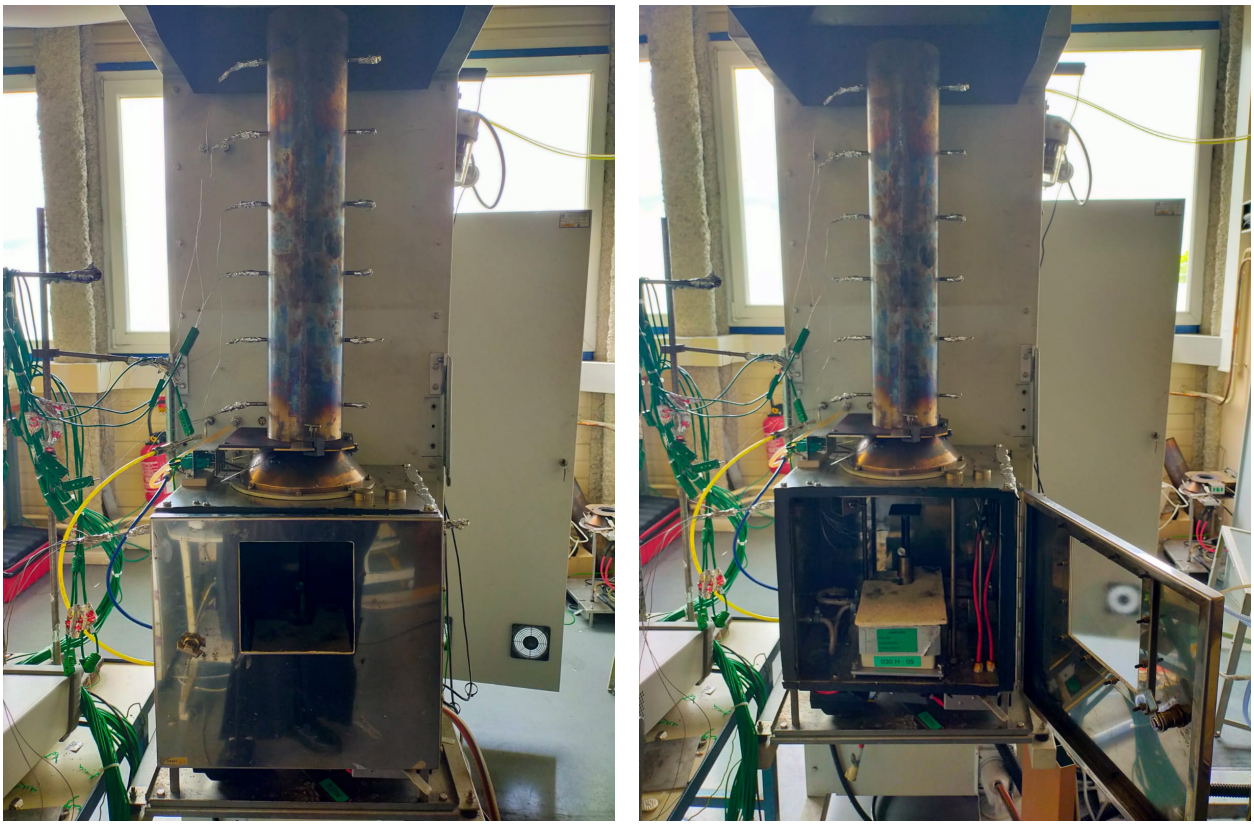

Figure 2.2: The controlled atmosphere cone calorimeter

The air/nitrogen mixture is thoroughly mixed before entering the enclosure to ensure a homogeneous mixture inside the combustion chamber. The radiant cone, similar to a gray

body, exposes the sample to a constant heat flux within the range of 5 to $75kW/m^2$. The temperature of the heating cone is regulated through several thermocouples. At its basis, the remotely operated shutters limit the quantity of heat at the surface of the sample before the start of the test. The height between the exposed surface of the sample and the radiant cone is fixed at $25mm$. A spark plug, located $15mm$ above the exposed surface of the sample, is used to ignite the decomposition gases when the gas concentration reaches the lower flammability limit. A chimney of $0.6m$ height is placed in the upper part of the cone heater and directly underneath the exhaust hood without a direct connection. This chimney is used to limit post-oxidation phenomena at the cone outlet [44]. To prevent the backflow of ambient air into the chimney, a 20% diameter restriction is applied to the chimney outlet. The device is positioned under an exhaust duct, inside of which a ring allows the sampling of the gases, which are then passed through carbon monoxide, carbon dioxide, and oxygen analyzers. The measurement of these gases allows the calculation of the heat release rate using the oxygen depletion method.

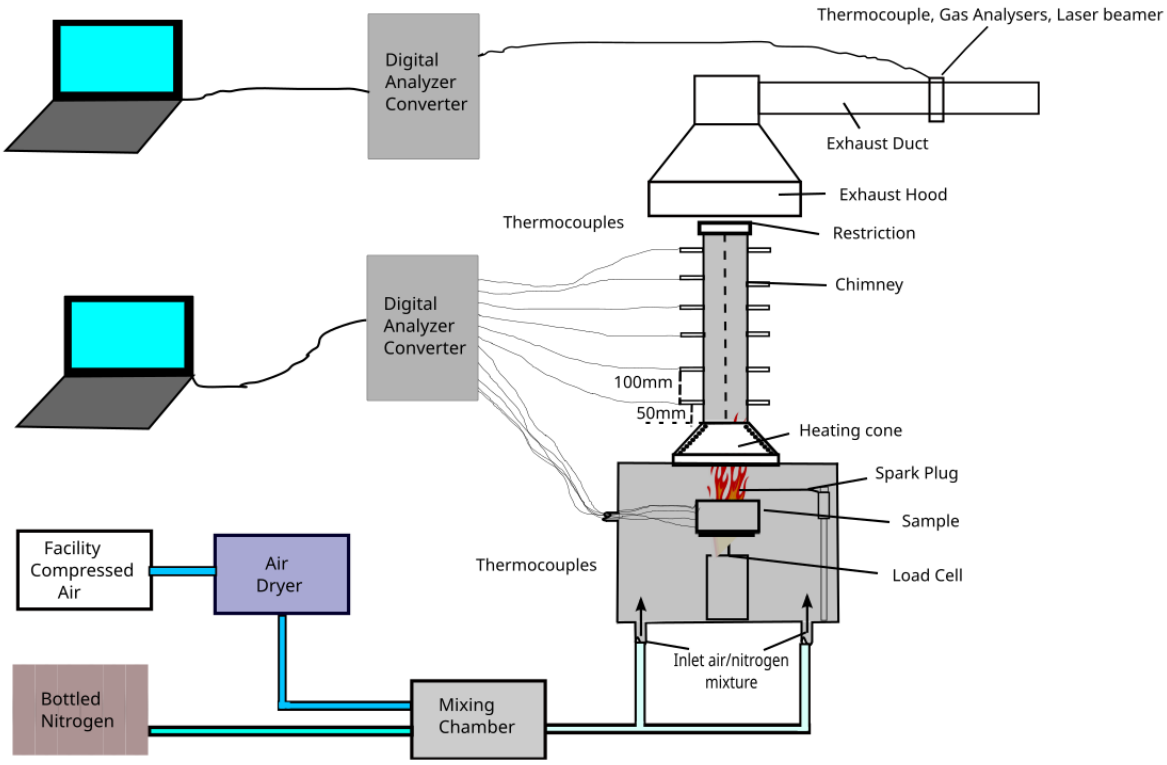

Figure 2.3: Schema of the Controlled Atmosphere Cone Calorimeter device used

The experimental bench used in this study has a few limitations. The impact of those limitations on the results is unknown and is complicated to quantify. Tests have been performed continuously at a rate of 2 to 3 tests per day. After each test, the bench is left to rest for 15 minutes. However, the resting phase does not allow a full cooling of the bench. Then, the first test of the day is generally conducted inside a "cooler" bench. The second and third tests are performed then in a bench whose sides have already stored heat (already exposed to heat generated by the heating cone and the combustion of the material). Moreover, it is important to note that the door of the enclosure is equipped with a joint isolating the enclosure from the outside air. However, this joint is not a 100% effective, and air from outside can leak inside. Consequently, oxygen is still entering the controlled atmosphere and it is not possible to reach a totally inert atmosphere.

2.3 Heat release rate correction

The heat release rate is the energy released per unit time during the combustion. It is calculated using the oxygen depletion method which suggests that the energy released is proportional to the oxygen consumed [62]. To determine the latter, a measurement of the combustion products is necessary. Some methods are based upon the measurements of CO_2 and O_2, CO_2, CO, and O_2 or others CO_2, CO,O_2 and soot. The following method used in this study is based on the O_2 depletion. Janssens [63] suggests an equation (Equation 2.3.1) to calculate the heat release rate in a cone calorimeter based on the mass conservation principle. This formula is typically used for the standard cone calorimeter.

$$\dot{Q} = \left[\Delta h_{O_2}\phi - (\Delta h_{CO} - \Delta h_{O_2})\frac{1-\phi}{2}\frac{X^A_{CO}}{X^A_{O_2}}\right]\frac{\dot{m}_e}{1+\phi(\alpha-1)}\frac{M_{O_2}}{M_a}(1-X^0_{H_2O})X^{A^0}_{O_2} \quad (2.3.1)$$

With the depletion factor ϕ as:

$$\phi = \frac{X^{A^0}_{O_2}(1-X^A_{CO}-X^A_{CO_2}) - X^A_{O_2}(1-X^{A^0}_{O_2})}{(1-X^A_{O_2}-X^A_{CO_2}-X^A_{CO})X^{A^0}_{O_2}} \quad (2.3.2)$$

Where $\dot{Q}$ is the heat release rate, Δh_{O_2} is the average value of the net heat release per unit mass of oxygen consumed, ϕ is the oxygen depletion factor, Δh_{CO} is the net heat release per unit mass of oxygen consumed for CO ($\Delta h_{CO} = 17.6kJ/g_{O_2}$, [64], X^A_{CO} is the measured mole fraction of carbon monoxide in the exhaust gases, $X^A_{O_2}$ is the measured mole fraction of oxygen in the exhaust gases, $\dot{m}_e$ is the mass flow rate in the exhaust duct, α is the chemical expansion factor, M_{O_2}, M_a are the molecular weight of O_2 and air, $X^0_{H_2O}$ is the mole fraction of water vapor in the incoming air, $X^{A^0}_{O_2}$ is the measured mole fraction of oxygen in the incoming air, X^A_{CO} is the measured mole fraction of carbon monoxide in the exhaust gases, and $X^A_{CO_2}$ is the measured mole fraction of carbon dioxide in the exhaust gases. "A" refers to analyzer-measured variables.

However, in this study, the measure of the gaseous component is realized in the exhaust hood system, which is not directly linked to the CACC device. Due to this open design, the combustion gases may continue to oxidize with the surrounding air of the laboratory when they emerge from the chimney up to the sampling probe, biasing the oxygen measurement and therefore the heat release rate calculations. To compensate for this error, the heat release rate is corrected using Werrel's method [65].

Werrel starts with Hugget's [66] proportionality equation for complete combustion and the oxygen mass consumed as shown in Equation 2.3.3.

$$\dot{Q} = \Delta h_{O_2}.(\dot{m}^{in}_{O2} - \dot{m}_{O2}) \tag{2.3.3}$$

Where $\dot{Q}$ is the heat release rate, Δh_{O_2} is the average value of the net heat release per unit mass of oxygen consumed, $\dot{m}^{in}_{O2}$ is the mass flow rate of O_2 in the incoming air and $\dot{m}_{O2}$ is the mass flow rate of O_2 in the exhaust gas.

Assuming that the generation of carbon monoxide is an indicator of an incomplete combustion [63, 64] and that the ratio of O_2, N_2, CO_2 and CO does not change because of the trapped water, Werrel [65] writes the mole fraction of the incoming air in the duct of the oxygen analyzer as Equation 2.3.4.

$$X_{O_2}^{A^{in}} = \frac{\frac{\dot{m}_{O2}^{in}}{M_{O2}}}{\frac{\dot{m}_{O2}^{in}}{M_{O2}} + \frac{\dot{m}_{N2}^{in}}{M_{N2}} + \frac{\dot{m}_{CO_2}^{in}}{M_{CO_2}} + \frac{\dot{m}_{CO}^{in}}{M_{CO}}} \tag{2.3.4}$$

Where $X_{O_2}^{A^{in}}$ is the measured mole fraction of O_2 in the incoming air, $\dot{m}_{O2}^{in}$, $\dot{m}_{N2}^{in}$, $\dot{m}_{CO_2}^{in}$, $\dot{m}_{CO}^{in}$ are the mass flow rate of respectively O_2, N_2, CO_2, and CO in the incoming air, and M_{O2}, M_{N2}, M_{CO_2}, M_{CO} are the molecular weight of respectively O_2, N_2, CO_2, and CO. Similarly, Werrel writes the depleted mole fraction of oxygen in the exhaust gas in the duct of the oxygen analyzer as shown in Equation 2.3.5.

$$X_{O_2}^{A} = \frac{\frac{\dot{m}_{O2}}{M_{O2}}}{\frac{\dot{m}_{O2}}{M_{O2}} + \frac{\dot{m}_{N2}}{M_{N2}} + \frac{\dot{m}_{CO_2}}{M_{CO_2}} + \frac{\dot{m}_{CO}}{M_{CO}}} \tag{2.3.5}$$

Where $X_{O_2}^{A}$ is the measured mole fraction of O_2 in the exhaust gaz, $\dot{m}_{O2}$, $\dot{m}_{N2}$, $\dot{m}_{CO_2}$, $\dot{m}_{CO}$ are the mass flow rate of respectively O_2, N_2, CO_2, and CO in the exhaust gas.
Since nitrogen does not participate in the combustion, its incoming mass flow rate is equal to its outflow mass flow rate [63] and can be written as Equation 2.3.6.

$$\dot{m}_{N2}^{in} = \dot{m}_{N2} \tag{2.3.6}$$

Rearranging Equation 2.3.4 and Equation 2.3.5 in terms of Equation 2.3.6, the mass flow of oxygen consumed is given by Equation 2.3.7.

$$\dot{m}_{O2}^{in} - \dot{m}_{O2} = \left[\frac{X_{O_2}^{A^{in}}(1 - X_{CO_2}^{A} - X_{CO}^{A} - X_{O_2}^{A})(1 - X_{CO_2}^{A^{in}} - X_{CO}^{A^{in}})}{(1 - X_{O_2}^{A^{in}} - X_{CO_2}^{A^{in}})(1 - X_{O_2}^{A} - X_{CO_2}^{A} - X_{CO}^{A})} \right] \dot{m}_{N2}^{in}.\frac{M_{O2}}{M_{N2}} \tag{2.3.7}$$

Where $X_{CO_2}^{A}$ and X_{CO}^{A} are the measured mole fraction of respectively CO_2, and CO in the exhaust gas, and $X_{CO_2}^{A^{in}}$ and X_{CO}^{A} are the measured mole fraction of respectively CO_2, and CO in the incoming air.
Replacing Equation 2.3.7 in Equation 2.3.3 and adding the correction for the trapped water $(1 - X_{H_2O}^{A^{in}})$ that is assumed known from the humidity in the room, the resulting equation

is given by Equation 2.3.8.

$$\dot{Q} = \Delta h_{O_2} \left[\frac{X_{O_2}^{A^{in}}(1 - X_{CO_2}^{A} - X_{CO}^{A} - X_{O_2}^{A})(1 - X_{CO_2}^{A^{in}})}{(1 - X_{O_2}^{A^{in}} - X_{CO_2}^{A^{in}} - X_{CO}^{A})} \right] \dot{m}_a . \frac{M_{O2}}{M_a}(1 - X_{H_2O}^{A^{in}}) \quad (2.3.8)$$

Where M_a is the molecular weight of the incoming air and $\dot{m}_a$ is the mass flow rate of the incoming air given by Equation 2.3.9.

$$\dot{m}_a = \frac{\dot{m}_e}{1 + \phi(\alpha - 1)} \quad (2.3.9)$$

Where $\dot{m}_e$ is the mass flow rate of the exhaust gaz, ϕ is the oxygen depletion factor related to the entire combustion system given by Equation 2.3.10 and α is the chemical expansion factor.

$$\phi = \frac{X_{O_2}^{A^{in}}(1 - X_{CO_2}^{A} - X_{CO}^{A} - X_{O_2}^{A})(1 - X_{CO_2}^{A^{in}})}{(1 - X_{O_2}^{A^{in}} - X_{CO_2}^{A^{in}} - X_{CO}^{A})X_{O_2}^{A^{in}}} \quad (2.3.10)$$

Werrel states that the heat released by incomplete combustion can be calculated by substracting the heat released through the oxidation of CO from the heat released through complete combustion as shown in Equation 2.3.11.

$$\begin{aligned} \dot{Q} &= \dot{Q}_{tot} - \dot{Q}_{CO} \\ &= \Delta h_{O_2}(\dot{m}_{O2}^{A^{in}} - \dot{m}_{O2} + (\Delta\dot{m}_{O2})_{CO} - \Delta h_{CO}(\Delta\dot{m}_{O2})_{CO} \\ &= \Delta h_{O_2}(\dot{m}_{O2}^{A^{in}} - \dot{m}_{O2}) - (\Delta h_{CO} - \Delta h_{O_2})(\Delta\dot{m}_{O2})_{CO} \end{aligned} \quad (2.3.11)$$

Where $\dot{Q}$ is the heat release rate of incomplete combustion, $\dot{Q}_{tot}$ is the heat release rate of complete combustion, $\dot{Q}_{CO}$ is the heat release rate of oxidation of CO, Δh_{CO} is the net heat release rate per unit mass of oxygen consumed for the combustion of CO to CO_2, and $(\Delta\dot{m}_{O2})_{CO}$ is the oxygen mass consumed by the oxidation of CO.

Using the stochiometric approach from [63]for $(\Delta\dot{m}_{O2})_{CO}$, Werrel writes this parameter as

shown in Equation 2.3.12.

$$(\Delta \dot{m}_{O2})_{CO} = \frac{1}{2}(1-\phi)\frac{X^A_{CO_2}}{X^A_{O_2}}\frac{M_{O2}}{M_a}\dot{m}_a X^{A^{in}}_{O_2} \tag{2.3.12}$$

Equation 2.3.8, Equation 2.3.9, Equation 2.3.10 and Equation 2.3.12 lead to Equation 2.3.13.

$$\dot{Q} = \left[\Delta h_{O_2} - (\Delta h_{CO} - \Delta h_{O_2})\frac{1-\phi}{2}\frac{X^A_{CO_2}}{X^A_{O_2}}\right]\frac{\dot{m}_e}{1+\phi(\alpha-1)}(1-X^{A^{in}}_{H_2O})X^{A^{in}}_{O_2} \tag{2.3.13}$$

By introducing a thermal expansion factor $\tilde{\nu}$, $(1-X^{A^{in}}_{H_2O})$ becomes $(1-X^A_{H_2O}.\tilde{\nu})$, Knowing that the ratio of mlecular weight of oxygen and air is 1.10, the final expression of the heat release rate is given by Equation 2.3.16.

$$\dot{Q} = 1.10\Delta h_{O_2} X^{A^{in}}_{O_2}\dot{m}_e\left[\frac{\phi - 0.5\left(\frac{\Delta h_{CO}}{\Delta h_{O_2}}-1\right)(1-\phi)\left(\frac{X^A_{CO}}{X^A_{O_2}}\right)}{(1-\phi)+\phi(\alpha-1)X^B_{O_2}}\right].(1-X^A_{H_2O}.\tilde{\nu}) \tag{2.3.14}$$

With the oxygen depletion factor defined by Equation 2.3.15

$$\phi = \frac{X^{A^{in}}_{O_2}(1-X^A_{CO_2}-X^A_{CO}) - X^A_{O_2}(1-X^A_{CO_2}.\tilde{\nu})}{X^{A^{in}}_{O_2}(1-X^A_{O_2}-X^A_{CO_2}-X^A_{CO})} \tag{2.3.15}$$

Where Δh_{O_2} is the net heat of combustion per unit mass of oxygen consumed, $X^B_{O_2}$ is the time-dependent intake mole fraction of O_2, $\dot{m}_e$ is the mass flow rate in the exhaust duct calculated from the pressure drop and the gas temperature at the orifice flow meter, Δh_{CO} is the net heat release per unit mass of O_2 consumed for the oxidation of CO into CO_2, α is the stoichiometric dilution factor, $\tilde{\nu}$ is a thermal expansion factor, X_{O_2}, X_{CO} and X_{CO_2} are respectively the measured mole fraction of O_2, CO and CO_2 in the exhaust duct, $X^A_{CO_2}$ the measured mole fraction of CO_2 in the diluting ambient air, and $X^A_{H_2O}$ is the mole fraction of water in the diluting ambient air.

A correction example is shown in Figure 2.4. The heat release rate under air is shown in Figure 2.4a. The corrected (red plot) and measured (blue plot) heat release rates are identical. The heat release rate under a vitiated atmosphere is shown in Figure 2.4b. The results show that the measured HRR is overestimated by 29% in this case, but the error can go as high as 30% according to Werrel [65]. In the present document, the calculations of the HRR are therefore based upon Werrel's approach.

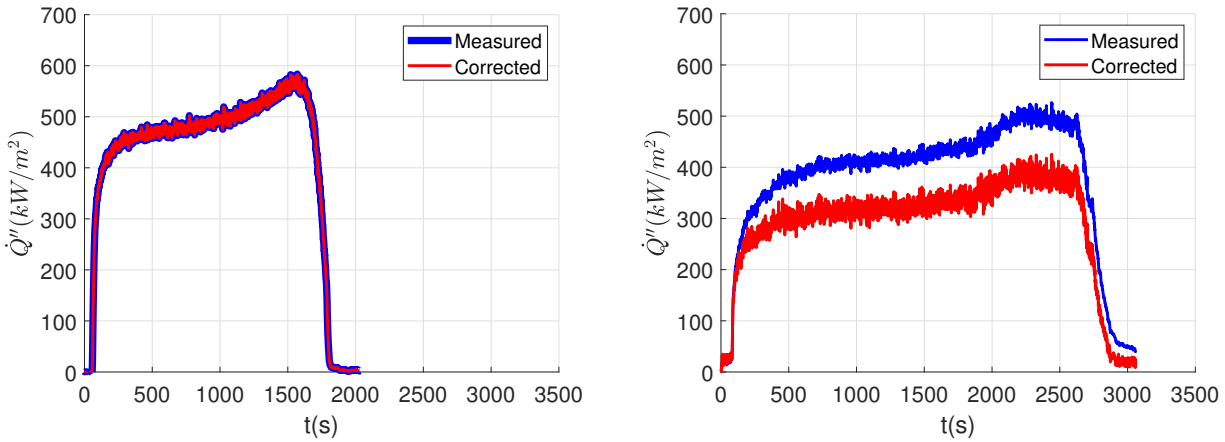

(a) (b)

Figure 2.4: Illustration of the measured and corrected heat release rate per unit surface with a) under air and b) under vitiated atmosphere

The total heat release rate $\dot{Q}$ expressed in J may be caluclated based on the heat release rate $\dot{Q}''$ using Equation 2.3.16.

$$\dot{Q} = \int_S \int_t \dot{Q}'' dS dt \tag{2.3.16}$$

2.4 Gas temperature field

During this thesis, gas temperatures are evaluated under different conditions. The purpose of this is to evaluate the gas temperatures and to observe their behavior under different oxygen concentrations and heat flux conditions during the tests (considering also ignition and extinction).

During the tests, the gas temperature field distribution is measured within the stack. The

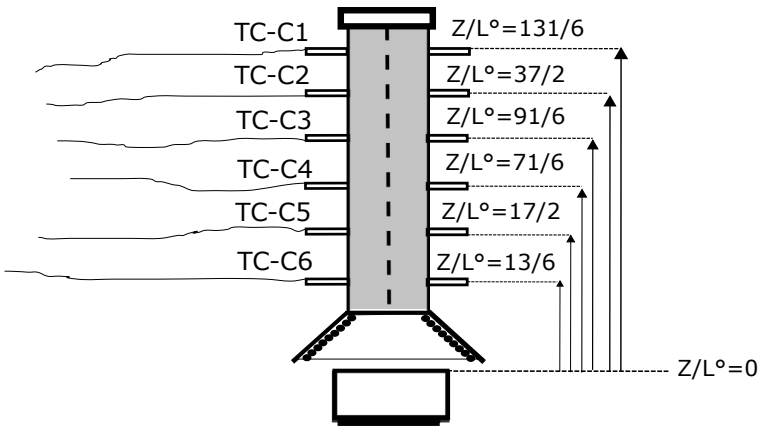

Figure 2.5: Setup of the thermocouples within the stack

chimney is equipped with small hollow metal tubes (Figure 2.3) allowing the insertion of sheathed thermocouples at several heights. Measurements are performed using type K, class A thermocouples featuring a mineral-insulated sheath diameter of 0.5mm. The thermocouple TC-C1 is positioned at a height of 50mm from the base of the chimney (i.e. at a height of 155mm from the initial surface of the sample). The thermocouples TC-C2, TC-C3, TC-C4, TC-C5, and TC-C6 are then placed 100 mm apart. The hot junction of the thermocouples is positioned along the centreline of the duct. The acquisition time is 1s.

The temperature measurements are corrected by factoring in the thermal inertia effects and radiative exchanges at the bead with the environment. Measurements are affected by the environment (convection, radiation from the cone, gas, and internal walls) and are subject to thermal leakage as shown in Figure 2.6. The heat balance is written at the thermocouple bead of diameter d and the gas temperature T can be expressed from the thermocouple temperature T_{tc} by Figure 2.6. Any heat transfer occurring between the thermocouple and the heated cone, the flames, or the outside air from the top of the chimney will be neglected. The thermal balance at the bead of the thermocouple can be written as Equation 2.4.1.

$$\rho.V_{tc}.C_p\frac{dT_{tc}}{dt} = \dot{Q}_{cat} + \dot{Q}_{cond} + \dot{Q}_c + \dot{Q}_r \tag{2.4.1}$$

$\dot{Q}_{cat}$ refers to the catalytic flux, $\dot{Q}_{cond}$ refers to the conduction energy lost through the thermocouple, $\dot{Q}_c$ refers to the convection energy between the thermocouple and the fluid

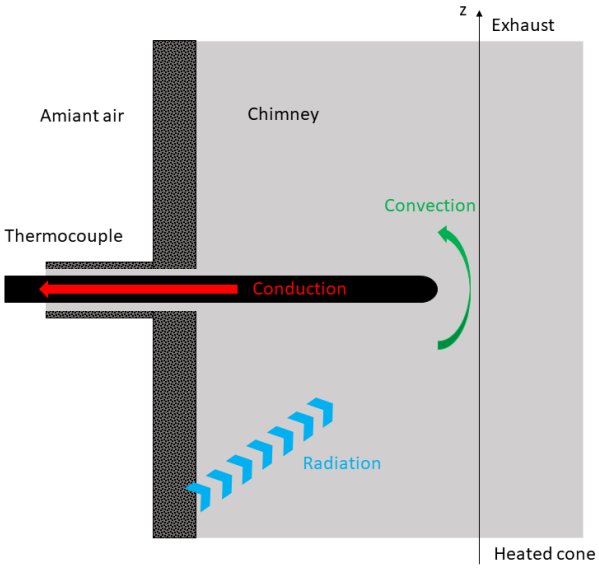

Figure 2.6: Thermal balance at the bead of a single thermocouple inside the chimney

in the chimney and $\dot{Q}_r$ refers to the radiation exchange between the theromcouple and its environment. The catalytic flux is assumed to be negligible as the hot junction is covered in a mineral sheath [67]. The heat losses from conduction can be assumed to be negligible [68]. For an unsteady system, Equation 2.4.1 becomes Equation 2.4.2.

$$\rho.V_{tc}.c_p\frac{dT_{tc}}{dt} = h_c.A_{tc}(T - T_{tc}) - \epsilon.\sigma.A_{tc}(T_{tc}^4 - F_{(tc-duct)}.T_{duct}^4.\epsilon_{duct})\frac{A_{tc}}{V_{tc}} \tag{2.4.2}$$

Equation 2.4.2 leads to Equation 2.4.3.

$$\frac{dT_{tc}}{dt} = \frac{h_c(T - T_{tc})}{\rho C_p}\frac{A_{tc}}{V_{tc}} + \frac{\epsilon\sigma}{\rho c_p}(F_{(tc-duct)}.T_{duct}^4.\epsilon_{duct} - T_{tc}^4) \tag{2.4.3}$$

The fluid passing through the chimney is assumed to be air and its thermal transport properties, such as the thermal conductivity k in $(W/m.K)$ (Equation 2.4.4), the kinematic viscosity ν in (m^2/s) (Equation 2.4.5), the specific heat at constant pressure c_p in $(J/kg.K)$ (Equation 2.4.6) and the density ρ in (kg/m^3) (Equation 2.4.7), are assumed to be temperature dependent and are calculated using the following equations [69].

$$k = 1.5207^{-11}T_{tc}^3 - 4.857^{-8}T_{tc}^2 + 1.0184^{-4}T_{tc} - 3.400747^{-6} \tag{2.4.4}$$

$$\nu = -1.363528^{-14}T_{tc}^3 + 1.00881778^{-10}T_{tc}^2 + 3.452139^{-8}T_{tc} - 3.400747^{-6} \tag{2.4.5}$$

$$c_p = 948.38 + 0.36T_{tc} - 1.43^{-4}T_{tc}^2 + 2.20^{-8}T_{tc}^3 \text{ , with } T_{tc} \text{ in } ^\circ C \tag{2.4.6}$$

$$\rho = 351.9T_{tc}^{-0.9996} \text{ , with } T_{tc} \text{ in } ^\circ C \tag{2.4.7}$$

The thermal diffusivity α in (m^2/s) (Equation 2.4.8) is calculated as follows [70]

$$\alpha = \frac{k}{C_p \rho} \tag{2.4.8}$$

In Equation 2.4.3, the convection coefficient h_c is defined from the Nusselt number Nu (Equation 2.4.9) [71].

$$h_c = \frac{Nuk}{d_{tc}} \tag{2.4.9}$$

The Nusselt number is calculated as a function of the Reynolds number Re as well as the Prandt number Pr using a correlation that characterizes the heat exchange involving the flow field perpendicular to a horizontally oriented cylinder (Equation 2.4.10) [72].

$$Nu = 0.42Pr^{1/5} + 0.57Re^{1/2}Pr^{1/3} \tag{2.4.10}$$

The Reynold's number of the flow in the stack is defined by Equation 2.4.11 [73].

$$Re = \frac{v_g d_{tc}}{\nu} \tag{2.4.11}$$

The gas velocity v_g inside the chimney is considered to be uniform. It is calculated using the imposed flow rate of the inlet air $(160l/min)$ and the exit diameter of the cone $d_{cone} = 0.076m$. The Prandt number of the flow in the stack is defined by Equation 2.4.12 [74].

$$Pr = \frac{\nu}{\alpha} \tag{2.4.12}$$

The bead of the thermocouple is considered to be a sphere. The ratio between the surface and the volume of the sphere is defined by Equation 2.4.13.

$$\frac{A_{tc}}{V_{tc}} = \frac{4\pi(\frac{d_{tc}}{2})^2}{\frac{4}{3}\pi(\frac{d_{tc}}{2})^3} = \frac{6}{d_{tc}} \tag{2.4.13}$$

As a result, the gas temperature equation is then deduced as such:

$$T = T_{tc} + \frac{d_{tc}^2 \rho c_p}{6Nu.k}\frac{dT_{tc}}{dt} - \frac{d_{tc}^2 k}{6Nu.k}(T_{tc}^4 - F_{(tc-duct)}.T_{duct}^4.\epsilon_{duct}) \tag{2.4.14}$$

For the calculations, the following assumptions are taken:

1. The media is supposed to eb transparent
2. The thermocouples are considered to be made only of Alumel. The properties of Alumel are: $\rho = 8610kg/m^3$, $c_p = 523J/kg.K$ and $k = 29W/mK$.
3. The effect of pyrolysis and combustion gas are neglected.
4. The inner wall of the chimney is considered to be black because of soot: $\epsilon_{duct} = 0.95$.
5. The view factor is assumed to be the one from a sphere of radius r to a coaxial cylinder of height $2H$ and radius R and is defined by Equation 2.4.15 [75].

$$F_{tc-duct} = \frac{1}{\sqrt{1 + \left(\frac{H}{R}\right)^2}} \tag{2.4.15}$$

The difference between the temperature given by a thermocouple and the temperature of the gas given by Equation 2.4.14 is shown in Figure 2.7. The thermocouple tends to underestimate the temperature of the gas in high-temperature environments. The difference between the thermocouple measurement and the calculated gas temperature can go as high as 7.2%.

2.5 In-sample temperature profile measurements

Five thermocouples, TC-S1, TC-S2, TC-S3, TC-S4, and TC-S5, have been placed within the specimen as shown in Figure 2.8 and Figure 2.9 and are connected to a central data

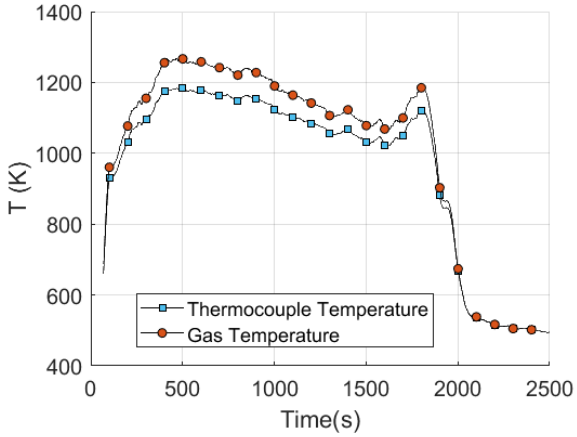

Figure 2.7: Difference between the thermocouple temperature and the gas temperature

acquisition system.

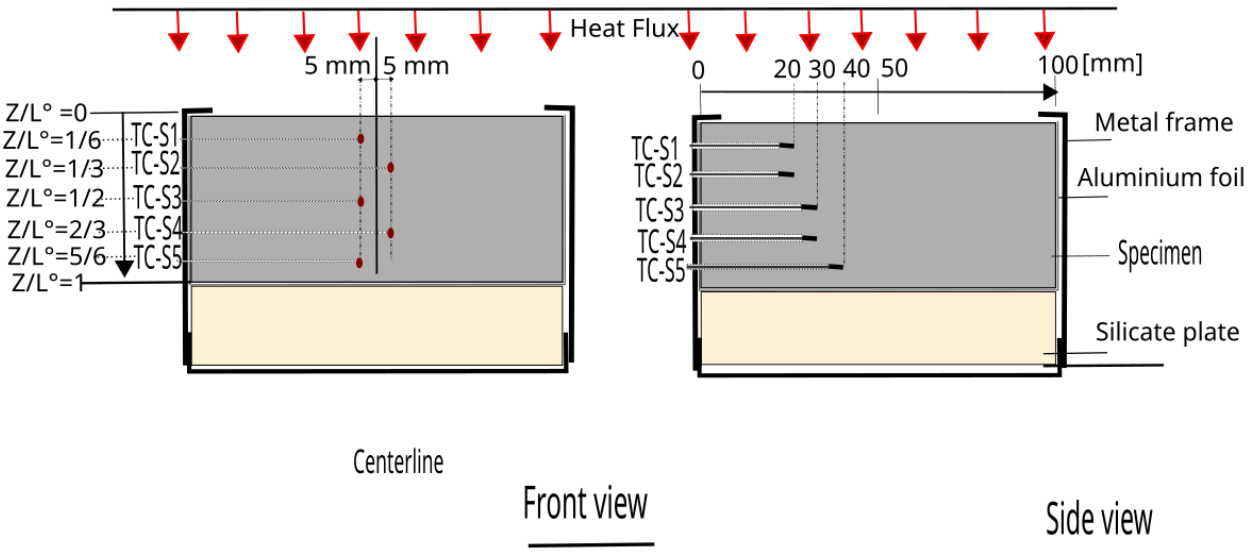

Figure 2.8: Front and side view of the disposition of the in-sample thermocouples.

The primary objective of this test procedure is to measure the in-depth heating and temperature profile within the sample. The metal frame was fitted with 1mm holes drilled into the side face to support and guide the thermocouples. Following the same approach, the specimens were also fitted with five thermocouples inserted into 1mm holes, also drilled from the side face. Sensors are arranged on 2 axes and in a staggered line so as to not interfere with the

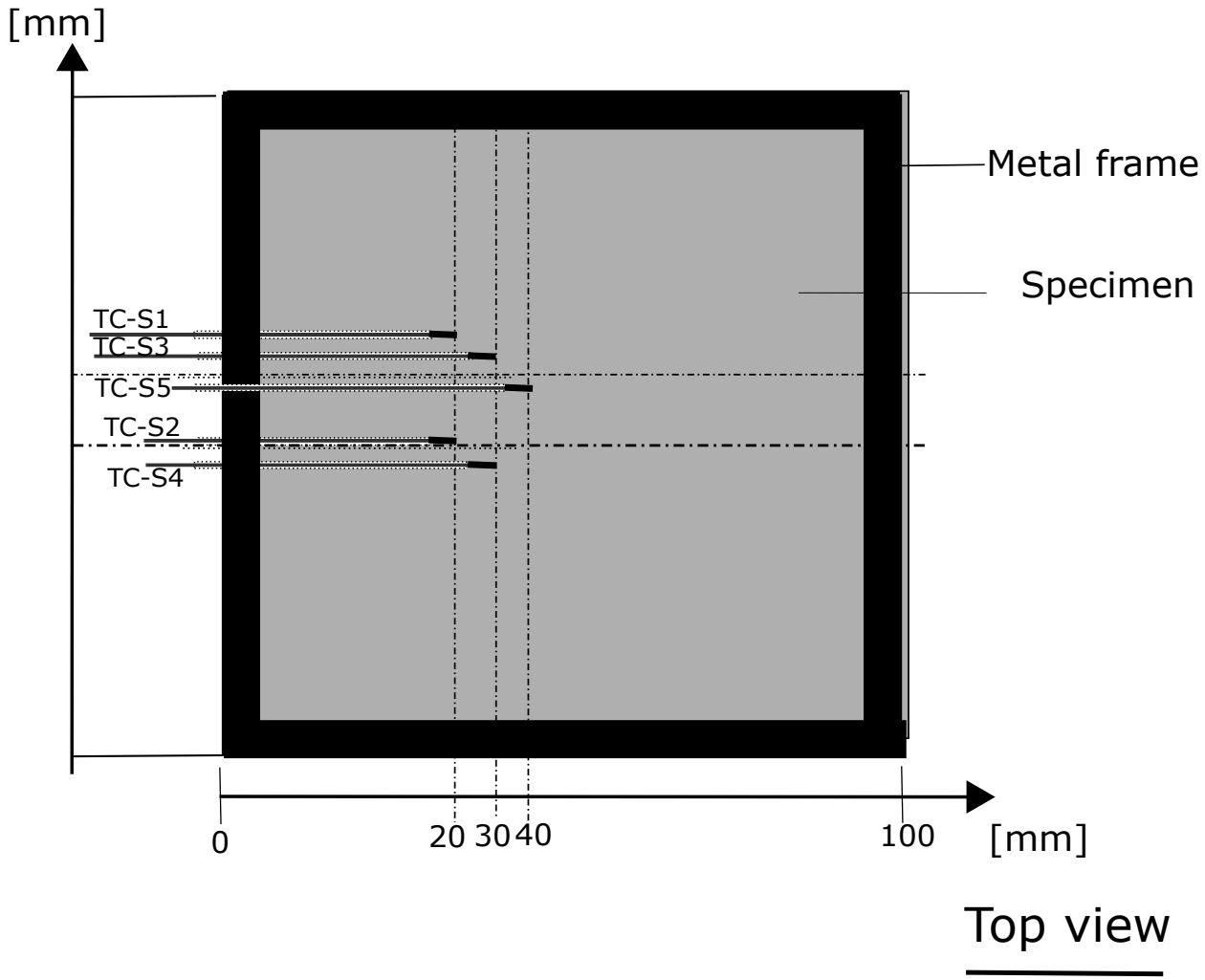

Figure 2.9: Top view of the disposition of the in-sample thermocouples

measurements. The thermocouples are positioned through the sample, perpendicular to the radiant heat flux, and aligned with the direction of the isotherm. The thermocouple closest to the surface, TC-S1, is located at a depth of $5mm$ from the sample surface. Subsequent thermocouples are positioned at $5mm$ intervals. All thermocouples embedded in the sample are sheathed in Type K, Class A material with a diameter of 0.5mm. The sampling period is 1s and the representation of the data is stopped as soon as the thermocouple temperature reaches $550K$. The in-sample temperatures are used to calculate the heating rate β inside the sample (Equation 3.2.9). The in-sample data were subject to only one test for every condition.

$$\beta = \frac{dT}{dt} \tag{2.5.1}$$

2.6 Total surface heat flux

Additional experiments were carried out to evaluate the total heat flux (from the cone, the flame...) received by the PMMA at material its surface. A hole was drilled in the center of the PMMA sample and the silicate plate. A wide view angle (180°C), water-cooled Schmidt–Boelter heat flux transducer with a $12mm$ diameter was used to measure the total heat fluxes as shown inFigure 2.10. The cooling water has an assumed temperature of $20°C$ and a flow rate of $0.67L/min$. The transducer was initially aligned with the surface of the sample and remained in a constant position throughout the test. Despite the changing surface conditions of the sample due to decomposition, the position of the heat flux remained unchanged. It can therefore be concluded that the transducer is not accurately located at the surface of the material during the test. Defining the errors introduced by this misalignment proves challenging. During those tests, the sample was not covered with a metal frame but rather rested on the top of a hollowed silicate plate and metallic table. It is covered in aluminum foil on all sides. A stainless steel cylinder is placed in the cylindrical hole between the material and the fluxmeter to protect the latter.

The energy equation at the surface of the gauge of the fluxmeter can be written as follows:

$$\dot{q}''_{tot} = \epsilon_{gauge}(\dot{q}''_{inc} - \sigma T^4_{gauge}) + h_c(T - T_{gauge}) \tag{2.6.1}$$

Where $\dot{q}''_{tot}$ is the heat flux at the gauge, ϵ_{gauge} the gauge emissivity, $\dot{q}''_{inc}$ the incident radiative heat flux, σ the Stefan-Boltzmann constant, T_{gauge} the gauge temperature, h_c the convective heat transfer coefficient, and T the gas temperature in the vicinity of the gauge. The first part of the equation corresponds to the net radiative component and the second one is the convective component.

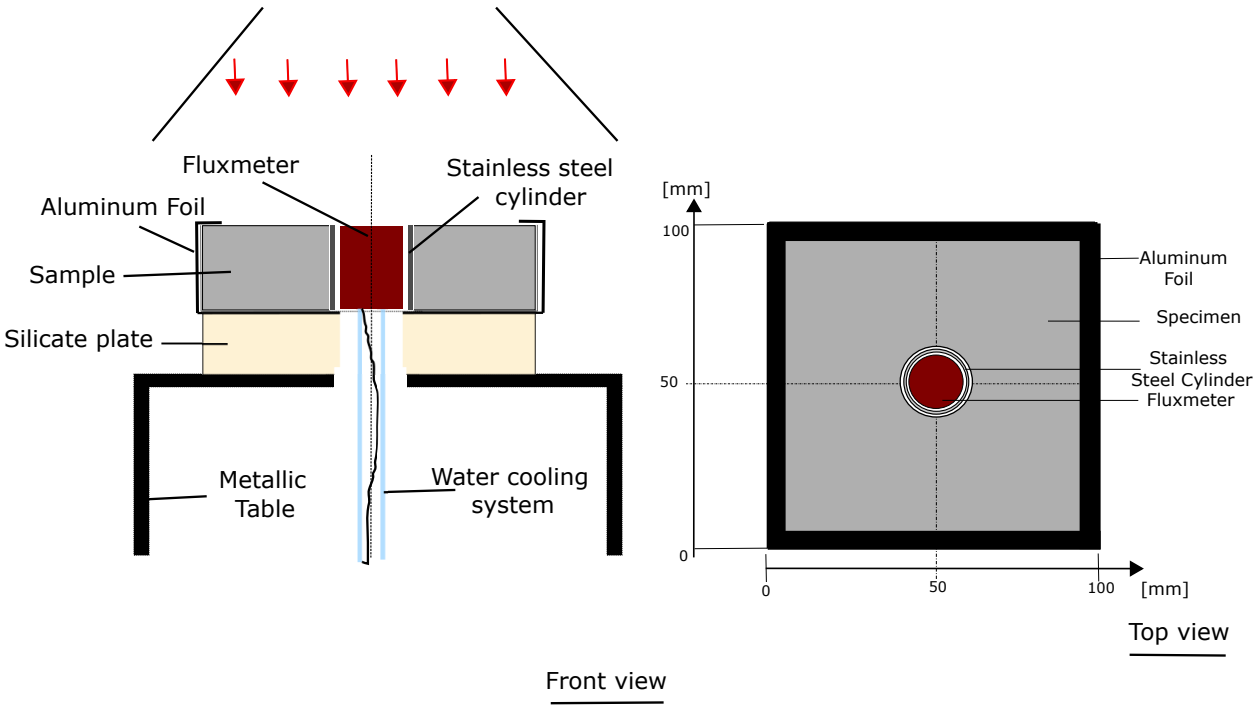

Figure 2.10: Surface heat flux measurement setup

2.7 Test conditions and experimental protocol

The specimen is placed on top of a silicate plate. The sample is covered with an aluminum sheet on three of its sides and on its bottom. One side is left uncovered to observe the time evolution of the surface during the tests. The aluminum foil limits the gas diffusion on the sample's sides and controls the exposed surface. The sample is covered with a metal frame. The exposed surface of the specimen is then $88.36mm^2$. During the test, the exhaust flow rate of the hood is set at $24 \pm 2l/s$. The tests are performed under a constant inlet air flow rate of $160l/min$. A high inlet rate would cause perturbations inside the enclosure, altering the decomposition of the PMMA. Conversely, a lower rate could induce vitiation and compromise the effective diffusion of the inlet mixture [45].The connection between the radiant cone and the metallic enclosure is water-cooled to limit the heating of the walls. The initial time t^0 corresponds to the moment the sample is exposed to the radiant cone. The acquisition period is fixed at 1s, it is performed during the entire combustion and is

stopped a few minutes after flame extinction. The tests are performed at constant oxygen concentrations ranging from 10 to 21%*vol*. Five main test campaigns were carried out. The first one consisted of testing the sample without any modification. Those tests allowed the data acquisition of the heat release rate, mass loss rate, and gas temperatures. They were repeated twice or thrice. The results presented in this study are the average data of all the tests done for each condition. The second testing campaign involved the placement of the thermocouples inside the sample. Those tests were carried out once. Finally, the third campaign was about the in-sample fluxmeter aimed to study the total heat flux at the surface of the sample. Two other test campaigns were carried out to determine the critical heat flux of ignition of the PMMA and its limiting oxygen concentration.
All the tests were done following the experimental protocol described below:

1. Calibration of the various devices such as the gas analyzers, the exhaust hood ventilator, and the radiant cone at the desired heat flux.

2. Door closed, calibration of the oxygen concentration and the airflow rate of the carrier gas within the enclosure until obtaining its stability at the desired values. In parallel, the preparation of the sample and positioning in the sample holder.

3. Opening the chamber door, position the sample inside on the rod of the precision scale, and closing the door.

4. Position the spark plug above the sample and expose the material to the radiant cone. Recording of the measurements.

5. End of test.

2.8 Determination of the ignition and extinction times

This section aims to explain the procedures used in order to determine the parameters at ignition and extinction. Indeed, ignition and extinction times are crucial parameters of fire behavior. For a test under normal air, the ignition time presents no confusion. It

is represented by the appearance of the flame and the rapid growth of the HRR curve. However, this study focuses on different oxygen concentrations ranging from $X_{O2} = 0.10$ to $X_{O2} = 0.21$. Lower oxygen concentrations can then result in chaotic and unpredictable behavior and oftentimes, interrupted and unsustained combustion, especially in its early phases. Figure 2.11 shows the heat release rate plots during the combustion at $X_{O2} = 0.21$ (blue plot) and $X_{O2} = 0.11$ (orange plot). The blue plot has a clear ignition time where sustained combustion starts and the HRR peaks. The orange plot shows chaotic behavior until stabilization at approximately $2250s$. It is then necessary to distinguish two types of ignition times: an unsustained combustion time starting at approximately $500s$ and a sustainable ignition time starting at approximately $2250s$. To determine the ignition time, the HRR is differentiated with respect to time and plotted around the time it peaks. The resulting plot is shown in Figure 2.12. The highest peak observed at $43s$ is the ignition time. The extinction time is determined by the same method as the ignition one. The HRR plot is differentiated with respect to time and plotted around the time it goes down to its initial value. The highest peak observed at $1790s$ is the extinction time. In cases where two ignition times are recorded, the unsustained ignition time is determined using the same method as before but with respect to the mass loss rate.

2.9 Mean calculation

Throughout this study, the time and space average values of the parameters are studied and compared. The time average is denoted by $\overline{...}$, and the space average is denoted by $< ... >$. The time averages of parameters are calculated based on the ignition time and extinction time referred to in the previous section. A time of $200s$ is added to t_i and substracted from t_e forming the mean calculation time range, following Equation 2.9.1.

$$\overline{X} = \frac{1}{(t_f - 200) - (t_i + 200)} \int_{t_i+200}^{t_f-200} X(t)dt \tag{2.9.1}$$

The spatial averaged is calculated by

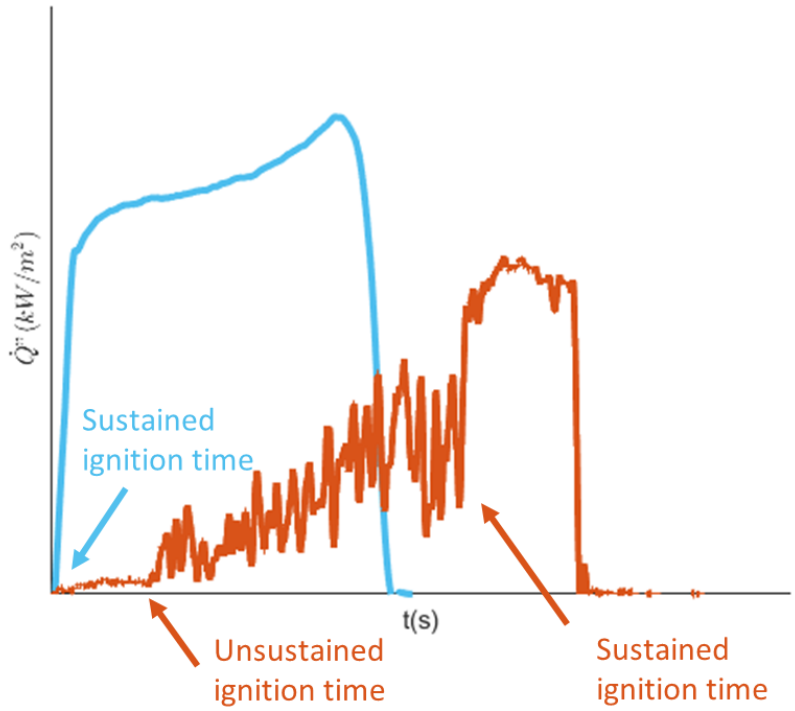

Figure 2.11: Sustained and unsustained ignition time

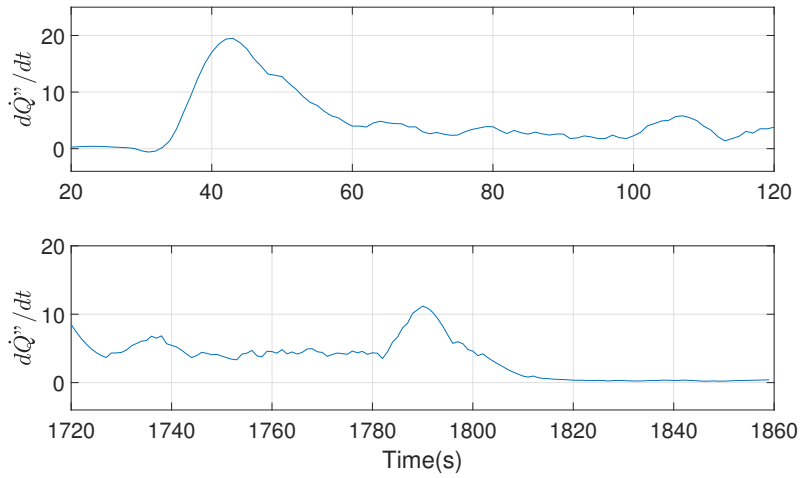

Figure 2.12: First derivative of the HRR

$$X = \frac{\sum_{Z/L^0=a}^{Z/L^0=b} X_i}{N} \tag{2.9.2}$$

Where $[a, b]$ is the range of the distance where the spatial average is calculated, and N is

the number of data being summed.

Most of the tests were repeated several times, in that case, the parameters used are the average of all the repetitions.

$$\overline{X} = \frac{\sum_{i=1}^{N} X_i}{N} \tag{2.9.3}$$

Where N is the number of repetitions.

2.10 Data representation

Sometimes, a measurement of a parameter can yield a signal that is extremely noisy. The Savitsky-Golay filter can be used to smooth the signal for the purpose of clarity. Better representation of the kinetics is possible with this filter without causing distortion. This is accomplished using the convolution technique, which involves using linear least squares to fit successive subsets of nearby data points with a low-degree polynomial. An analytical solution to the least-squares equations can be discovered when the data points are evenly spaced. This analytical solution takes the form of a single set of "convolution coefficients" that can be applied to all data sub-sets to provide estimates of the smoothed signal.

2.11 Conlusion

The chapter 2 has permitted to present the controlled atmosphere cone calorimeter modified and used in the present study as well as the expérimental protocol developed. A specific instrumentation has been implemented in order to characterize the flammability and combustibility parameters (as mass loss, mass loss rate, delay of ignition, HRR...), the temperature distributions in both the condensed and gas phases, and the heat transfers between those two phases. Finally, the formulas used for the determination of specific parameters are presented. In the two following chapter the results obtained from these experimental investigations are presented.

CHAPTER 3

THERMAL BEHAVIOR OF PMMA UNDER AIR

Table of Contents

This chapter serves as a platform to present the results of the parameters studied in the air environment ($X_{O2} = 0.21$). Its main goal is to provide a basis for the analysis of subsequent results obtained in atmospheres with lower oxygen concentrations. The study at an oxygen concentration of $X_{O2} = 0.21$ is performed under three different external heat flux conditions for $\dot{q}''_e$: $35kW/m^2$, $20kW/m^2$, and $12kW/m^2$. The following sections describe various parameters including the transfer of mass and heat inside the specimen through mass loss, in-sample temperature, and heating rate of the specimen. The analysis also focuses on the burning characteristics in the gas phase such as heat release, gas temperature field distribution, and total heat received by the specimen during the test. The first section focuses on the ignition parameters and the critical heat flux. The second section deals with the behavior of the PMMA in the solid phase and analyses parameters such as mass fraction, mass loss rate and in-sample temperature. Finally the third section focuses on the behavior of PMMA in the gas phase through parameters such as heat release, gas temperature and heat flux.

3.1 Ignition Parameters and critical heat flux under ambient air conditions

This section focuses on the ignition parameters of the PMMA under air exposed to various levels of external heat flux. It deals with the determination of the ignition parameters of the PMMA such as critical heat flux, the minimal ignition temperature, and the thermal response parameter defined by Janssens [20]. Tests were conducted to determine the ignition times for various conditions. If no ignition was observed within one hour during the test, the conditions were considered non-flammable. The averaged ignition times and their standard deviation observed for different external heat fluxes are detailed in Table 3.1.

Irradiance level $\dot{q}''_e(kW/m^2)$	Ignition time $t_{ig}(s)$
35	65 ± 4
20	274 ± 46
15	688
12	1603 ± 313
11	No ignition
10	No ignition
9	No ignition
8	No ignition

Table 3.1: Averaged ignition times of PMMA at $X_{O2} = 0.21$ for several heat fluxes

The ignition time increased from an average value of $65s$ at $\dot{q}''_e = 35kW/m^2$ to as high as $1603s$ for $\dot{q}''_e = 12kW/m^2$. The repeatability between the values in each condition increased significantly, from a few seconds for $\dot{q}''_e = 35kW/m^2$ to as much as $313s$ for $\dot{q}''_e = 12kW/m^2$. The repeatability is highlighted in Figure 3.1a. The ignition time seems to evolve in a hyperbolic function and tends to become almost instantaneous for higher heat fluxes. Another representation is to plot the evolution of the ignition time as $1/\sqrt{t_{ig}}$ instead as shown in Figure 3.1b. This representation facilitates the calculation of various parameters, such as the critical heat flux $\dot{q}''_{cr}$ following Janssen's method [63] used later in the calculation of the thermal response parameter (TRP). Conventionally, the $\dot{q}''_{cr}$ is assumed to be sufficient to heat the surface temperature of the sample to its minimal inflammation temperature with

an infinite exposure time. Tests were conducted to determine the critical heat flux $\dot{q}''_{cr}$ below which no ignition would occur under air for the PMMA under piloted ignition. The results showed a critical heat flux of $11.5 kW/m^2$ which is coherent with the values in the literature which fall between 9 and $13 kW/m^2$ [5, 6, 11, 16, 76].

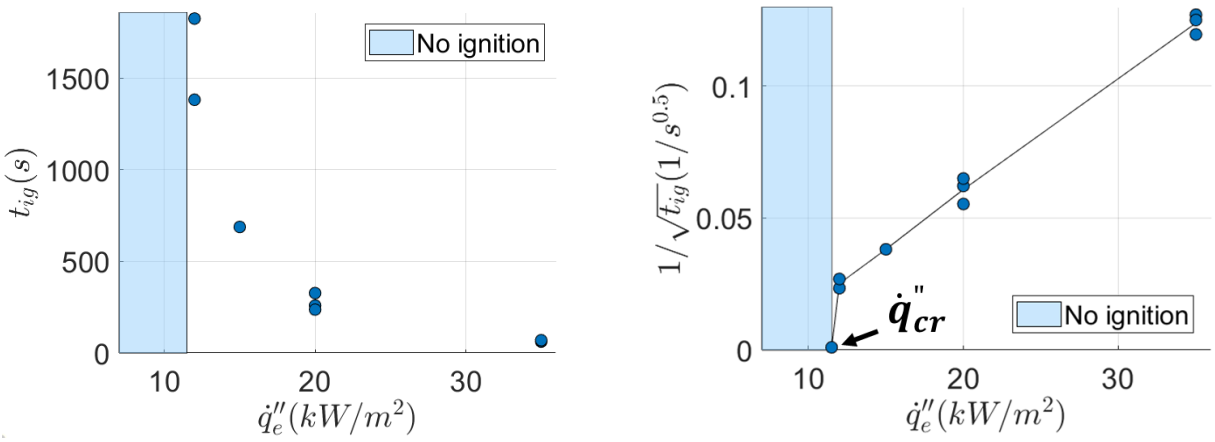

Figure 3.1: a) The ignition time of the PMMA sample under air for different heat fluxes. b) $1/\sqrt{t_{ig}}$ under air for different heat fluxes.

The minimum ignition temperature T_{ig} is the lowest temperature at which a substance can ignite and sustain combustion. It is possible to determine T_{ig} using Equation 3.1.1 [77].

$$T_{ig} = (\frac{\dot{q}''_{cr}}{2\sigma} + T_\infty^4)^{\frac{1}{4}} \tag{3.1.1}$$

Where T_{ig} is the minimal ignition temperature in (K), $\dot{q}''_{cr}$ is the critical heat flux for ignition in (kW/m^2), σ is the Stefan-Boltzmann constant in (W/m^2K^4), and T_∞ is the ambient temperature in (K). At the end of the calculations, the determined ignition temperature T_{ig} is $574K$. This value is inferior to the one reported by [77] which is $639K$. However, a crucial factor influencing this disparity becomes apparent when examining Table 3.2 showing that the critical heat flux in reference [77] is $18 kW/m^2$. This difference in heat flux explains the observed discrepancies in ignition temperatures between the two studies.

The thermal response parameter (TRP) is a parameter defined by Janssens to characterize the heating rate inside the material. According to the authors, it can be expressed by

Equation 3.1.2.

Parameter	Current study	*Parot et al.* [77]
$\dot{q}''_{cr}(kW/m^2)$	11.5	18
Ambient temperature $T_\infty(K)$	300	300
$T_{ig}(K)$ with Equation 3.1.1	574	639

Table 3.2: Comparison of the parameters and results of Equation 3.1.1 for the current study and the reference [77].

$$TRP = (T_{ig} - T_\infty)\sqrt{b} \tag{3.1.2}$$

Where TRP is the thermal response parameter, and b is the thermal effusivity in $(W/Km^2s^{0.5})$ given by Equation 3.1.3.

$$b = \sqrt{a.0.73.\dot{q}''_{cr}h_{ig}^{-1.1}} \tag{3.1.3}$$

Where a is the slope of the plot of $1/\sqrt{t_{ig}}$ as function of $\dot{q}''_e$ (see Figure 3.1b), and h_{ig} is the convective term introduced by Mikkola and Witchman [78] to linearise the radiative losses and given by Equation 3.1.4

$$h_{ig} = h_{cv} + \epsilon\sigma\frac{T_s^4 - T_\infty^4}{T_s - T_\infty} \tag{3.1.4}$$

Where h_{cv} is given by Equation 3.1.5 for $\dot{q}''_e < 50kW/m^2$ [63].

$$h_{cv} = 0.01198 + 3.74.10^{-4}\dot{q}''_e \tag{3.1.5}$$

Based on the previous equations, the value of the TRP is $243kWs^{0.5}/m^2$. This value is close to the one obtained by Tsai [6] for PMMA. In a horizontal configuration, the authors obtained a TRP of $250.8kWs^{0.5}/m^2$.

3.2 Behavior of PMMA solid phase under ambient air conditions

This section focuses on the solid-phase behavior of PMMA under ambient air conditions, specifically examining its responses at three distinct external heat flux: $\dot{q}''_e$: $35kW/m^2$, $20kW/m^2$, and $12kW/m^2$. In the following section, a dimensionless time t^+ is introduced as the product of the Fourier number Fo and the radiative Biot number Bi_r. It is obtained by Equation 3.2.1. This representation compare the results on the same time scale. It puts into evidence the difference in kinetics observed by eliminating the time delays due to the different external heat fluxes.

$$t^+ = Fo.Bi_r \tag{3.2.1}$$

Where Fo is the Fourier number given by Equation 3.2.2, and Bi_r is the radiative Biot number given by Equation 3.2.4.

$$Fo = \frac{\alpha t}{\overline{z}^2} \tag{3.2.2}$$

Where α is the thermal diffusivity, $t(s)$ the time, and $\overline{z}$ the average thickness based on the mass fraction and the initial thickness given by Equation 3.2.3. It is assumed that the average thickness is uniform across the entire surface of the sample, ensuring homogeneity. In addition, any potential side effects due to thermal losses are deliberately neglected in this analysis.

$$\overline{z} = Y.L^0 \tag{3.2.3}$$

Where L^0 is the initial thickness of the sample (which is $30mm$ in the current study).
The radiative Biot number is then calculated using Equation 3.2.4.

$$Bi_r = \frac{\epsilon \sigma T_s^3 \overline{z}}{k} \tag{3.2.4}$$

Where ϵ is the emissivity, σ is the Stefan-Boltzmann constant, $T_s(K)$ is the surface temperature that is assumed to be T_{ig} and k the thermal conductivity in $(W/(mK)$.

The previous equation leads to a simplified expression of t^+ given by Equation 3.2.5

$$t^+ = \frac{t.\epsilon\sigma T_s^3}{\overline{z}\rho c_p} \tag{3.2.5}$$

Where ρ is the density in (kg/m^3) and c_p the specific heat in $(J/(kgK)$.
In this chapter, the ignition times differences are important due to varying external heat fluxes, ranging from higher $\dot{q}''_e$ to lower values. For a better representation, the ignition time t_{ig} will be subtracted from the time t. The resulting dimensionless time Δt^+ calculated is defined by Equation 3.2.6.

$$\Delta t^+ = \frac{(t - t_{ig}).\epsilon\sigma T_s^3}{\overline{z}\rho C_p} \tag{3.2.6}$$

Where t_{ig} is the ignition time.

3.2.1 Mass transfer within the sample

This subsection focuses on the mass transfers for the PMMA under air for the three irradiance levels studied. The thermal decomposition is described through two parameters: the mass fraction Y and the specific mass loss rate $\dot{m}''$. The calculation of Y is detailed in Equation 3.2.7.

$$Y = \frac{m(t)}{m_0} \tag{3.2.7}$$

Where $m(t)$ is the mass in g at a time t and m_0 is the initial mass in g of the sample.
The mass loss rate $\dot{m}$, is determined from the time derivative of the mass by the application of Equation 3.2.8. In the interest of facilitating a more meaningful comparison with existing literature, this study emphasizes the specific mass loss rate, denoted as $\dot{m}''$ which is the mass loss rate per unit area. This parameter was smoothed using the Savitsky-Golay filter during the whole duration of the test.

$$\dot{m}'' = \frac{1}{A}.\frac{dm(t)}{dt} \tag{3.2.8}$$

Where A is the exposed area of the sample in (m^2).

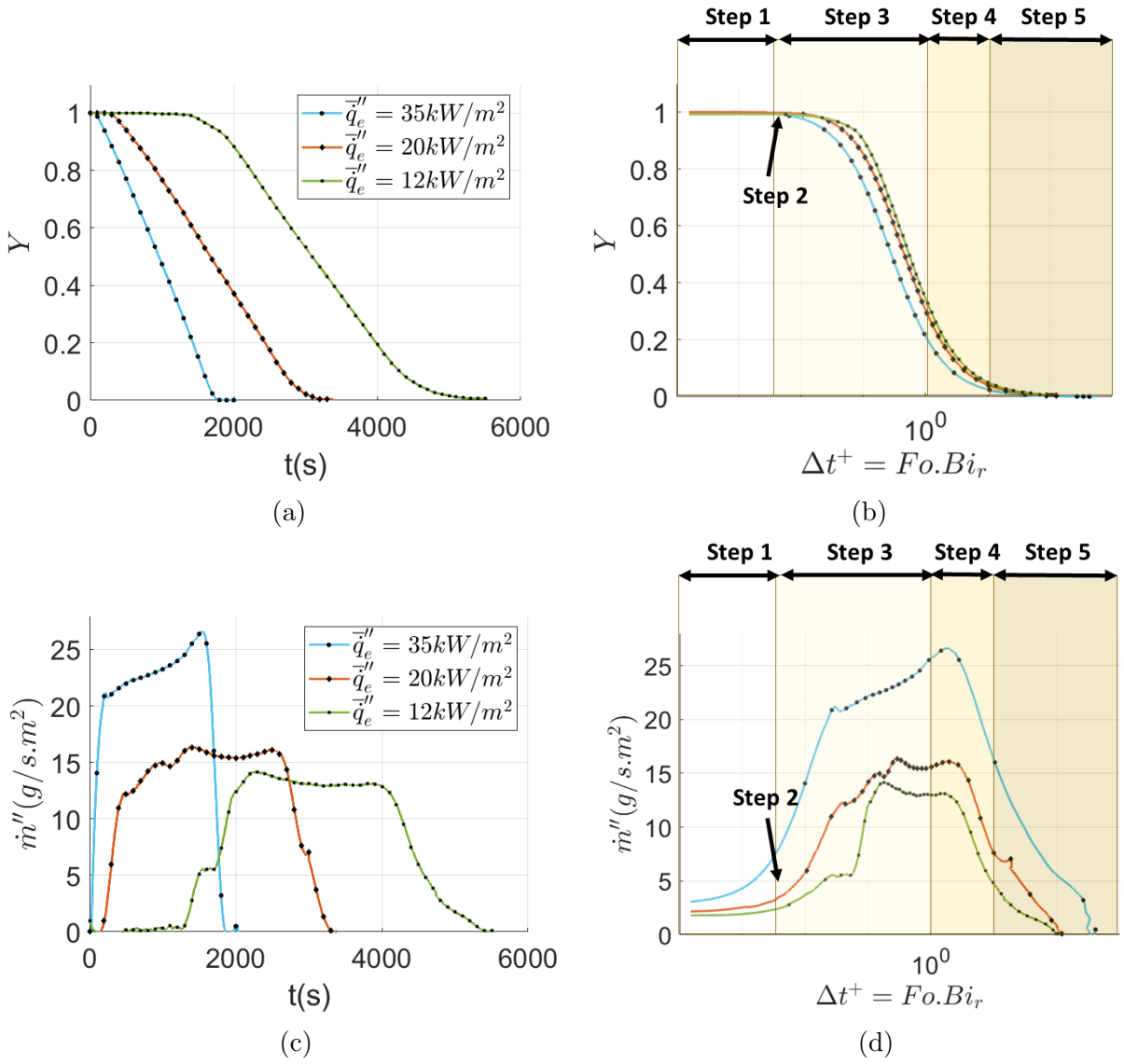

Figure 3.2: a) Mass Fraction Y with respect to time under air for several external heat fluxes. b) Mass Fraction Y with respect to t^+ under air for several external heat fluxes. c) Specific mass loss rate $\dot{m}''$ with respect to time under air for several external heat fluxes. d) Specific mass loss rate $\dot{m}''$ with respect to t^+ under air for several external heat fluxes.

The mass fraction Y is shown both in Figure 3.2a with respect to time and in Figure 3.2b with respect to t^+. Similarly, the specific mass loss rate is shown in Figure 3.2c with respect to time and in Figure 3.2d with respect to t^+. The curves shown in Figure 3.2 are the averaged curves of all the tests done for the same condition. The course of the decomposition process

shows a strong correlation with the external heat flux. In particular, a significantly slower decomposition is observed at lower $\dot{q}''_e$. For example, at $\dot{q}''_e = 35kW/m^2$, the test duration is about $1800s$. In contrast, this duration almost doubles to about $3000s$ when the external heat flux is reduced to $\dot{q}''_e = 12kW/m^2$. It is worth noting that at the end of each test, the value of Y approaches zero, indicating that all the material has decomposed and no residue is left. Consequently, the ending of the decomposition process is due to the absence of material.

The PMMA decomposition is classically described in four steps marked in Figure 3.2b and Figure 3.2d.

- Step 1: The PMMA sample is heated by cone radiation and reaches a critical point, initiating its thermal decomposition. The decomposition products, with lower decomposition temperature than the sample, are heated. This marks the start of the nucleation process, during which bubbles form and travel through the viscosity gradient toward the path of least resistance - the sample surface. At the surface, these bubbles burst, creating voids within the sample, increasing its exposed surface area. This step is represented as a constant slab in Figure 3.2 visible for lower values of $\dot{q}''_e$.

- Step 2: In the initial phase, when the surface temperature reaches the critical value and sufficient oxygen is available, the PMMA sample ignites. This ignition is indicated by a sudden increase in the $\dot{m}''$ and the appearance of an inflection point in the Y. For higher values of $\dot{q}''_e$, the ignition time is almost instantaneous, making in comparison Step 1 less noticeable in comparison. It is worth noting that Step 2 intervenes at the same t^+ moment for all three heat fluxes in Figure 3.2b and Figure 3.2d.

- Step 3: The following stationary phase corresponds to the thermal decomposition of thermally thick samples. This phase is characterized by a stable, almost constant value of the $\dot{m}''$ and a linear line with no change in slope observed in the Y.

- Step 4: The thermal feedback phase is initiated by the presence of an insulating silicate plate placed under the sample and corresponds to the decomposition of a thermally

thin sample. This phase is characterized by a pronounced spike in the $\dot{m}''$ and the appearance of another inflection point in the Y curve. The intensity of the spike in $\dot{m}''$ varies, being more pronounced at higher values of $\dot{q}''_e$ and more muted at lower values of $\dot{q}''_e$. However, it happens at the same t^+ time for the three different heat fluxes.

- Step 5: The final phase is characterized by the extinction of the fire. During this stage, the Y approaches zero, indicating a significant reduction in the material. At the same time, the $\dot{m}''$ decreases significantly due to the lack of the material. The reduction in the mass loss rate is a direct consequence of the reduction in material available for combustion.

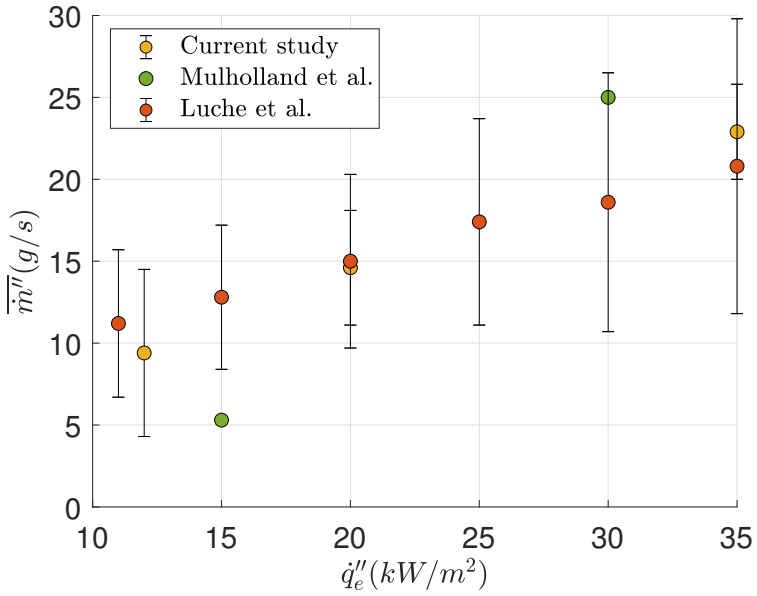

Figure 3.3: Averaged values of the specific mass loss rate for the current study, *Mulholland et al.* [41] and *Luche et al.* [16].

The external heat fluxes have a clear effect on the $\dot{m}''$ curves. They show a pronounced decrease at lower values of $\dot{q}''_e$. The average specific mass loss rate $\overline{\dot{m}''}$ calculated over the stationary phase shows a decrease from $22.9g/s.m^2$ for $\dot{q}''_e = 35kW/m^2$ to a value of $9.4g/s.m^2$ for $\dot{q}''_e = 12kW/m^2$. The values obtained in this current study are compared with values from the literature from *Mulholland et al.* [41] for clear PMMA and *Luche et al.* [16]

for black PMMA (Figure 3.3). The values from the current study are in agreement with the values from the literature.

This section shows that the thermal decomposition of the PMMA can be explained in 5 steps. Those five steps happen at different times due to the difference in heat flux. For a better representation, it is possible to get around those delays by plotting the specific mass loss rate against a dimensionless time. The averaged values of the specific mass loss rate have been calculated and represented with values from the literature. The results of this current study are in agreement with those of the literature. For a deeper understanding of the decomposition process happening inside the PMMA sample, the in-sample temperature and heating rates are detailed in the following section.

3.2.2 In-sample temperature and heating rate

Experiments were carried out to determine the temperatures within the sample throughout the decomposition process, and to observe the thermal response of the sample in an air environment under different external heat flux conditions. Five thermocouples were placed, at different heights from $Z/L^0 = 1/6$ to $Z/L^0 = 5/6$, to monitor the temperature evolution within the sample. The temperatures are represented until they reach a surface temperature of $T_s = 550K$. The results are shown in Figure 3.4. Upon ignition, the in-sample temperatures show a rapid rise, with the rate increasing as the thermocouple approaches the surface.

The evolution of the in-sample temperature with respect to time can be used to determine the heating rate $\beta(K/s)$ using Equation 3.2.9, providing an insight into the heat propagation inside the sample. The results are shown in orange in Figure 3.4.

$$\beta = \frac{dT}{dt} \tag{3.2.9}$$

Upon ignition of the sample, a rapid rise in the heating rate is observed, followed by a stabilization phase as the temperature of the thermocouple rises. In particular, as the thermocouple approaches the surface of the sample, there is a marked acceleration in the heating

rate. While the peak is less pronounced at lower external heat fluxes, it remains a noticeable phenomenon across varying heat flux conditions.

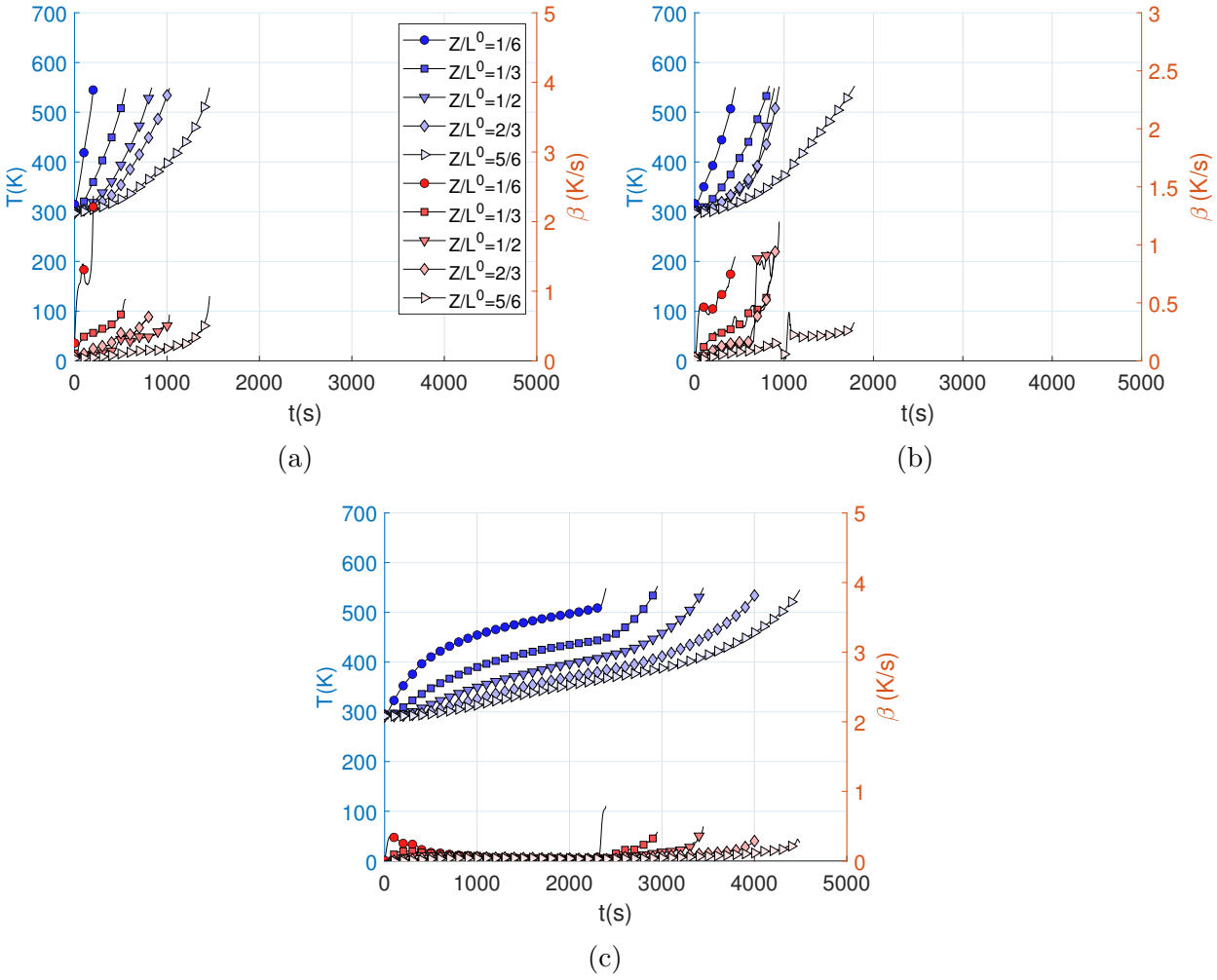

Figure 3.4: In-sample temperatures and their respective heating rate for a)$\dot{q}''_e = 35kW/m^2$, b)$\dot{q}''_e = 20kW/m^2$ and c) $\dot{q}''_e = 12kW/m^2$.

3.3 Behavior of PMMA gas phase under ambient air conditions

This section focuses on the gas phase behavior of PMMA at ambient air conditions, with particular emphasis on its response to various external heat fluxes. The investigation covers several parameters including heat release, gas temperature distribution, and total heat flux.

3.3.1 Heat release rate

The heat release rate is represented in Figure 3.5a with respect to time and Figure 3.5b with respect to t^+. The total heat release $\dot{Q}$ is represented in Figure 3.5c with respect to time. In Figure 3.5d, a dimensionless total heat release parameter $\dot{Q}^+$ is plotted with respect to t^+. It is calculated using Equation 3.3.1.

$$\dot{Q}^+ = \frac{\dot{Q}}{\dot{m}_0.\Delta H_{LHV}} \tag{3.3.1}$$

Where $\dot{m}_0.\Delta H_{LHV}$ represents the theoretical total heat release attainable.
The progression through the five steps described previously is apparent in Figure 4.2.

- Step 1: The PMMA sample starts its decomposition when exposed to the radiating cone. The duration of this phase is more prolonged for lower values of $\dot{q}''_e$.
- Step 2: Ignition occurs, illustrated by a sudden increase in $\dot{Q}''$ and an inflection point in the $\dot{Q}$ curve.
- Step 3: This phase is characterized by a stable, almost constant value of $\dot{Q}''$ and a linear $\dot{Q}$ curve with no change in slope.
- Step 4: A pronounced spike in $\dot{Q}''$ and another inflection point in the $\dot{Q}$ curve characterize this stage. Similar to $\dot{m}''$, the abruptness of the spike in $\dot{Q}''$ varies, being more pronounced at higher $\dot{q}''_e$ values and more muted at lower values.
- Step 5: This final stage involves a decrease in $\dot{Q}''$ due to the decrease in $\dot{m}''$ and the depletion of material. The $\dot{Q}$ curve reaches its final value during this phase.

Figure 4.2 shows a clear correlation between the heating rate and the irradiance levels applied. All the values recorded are in line with the reference value presented in [16] for black PMMA. The total heat release rate (THR), assessed under ambient air shows a clear correlation with the irradiance levels applied. The final value is attained faster for higher $\dot{q}''_e$. The resulting THR ranges from 800 to $1000 MJ/m^2$. Variation in initial sample mass contributes to the observed disrepancies in THR. The initial mass of the sample exhibits variability ranging

from $320g$ to $357g$, which affects the overall THR. As shown in Figure 3.5d, the final $\dot{Q}^+$ is between 0.8 and 1 for all the higher external heat fluxes, meaning that almost theoretical combustion energy has been attained.

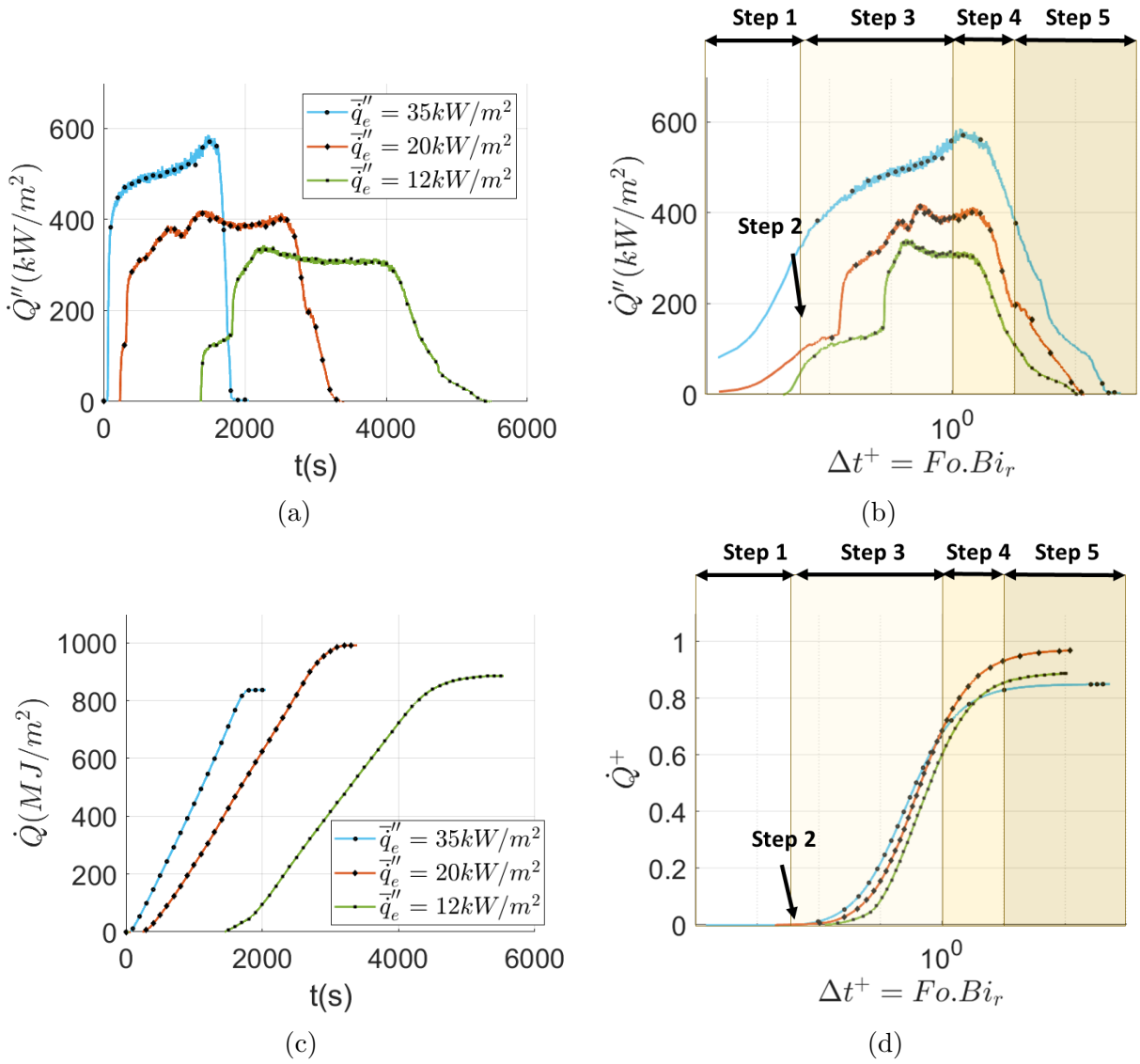

Figure 3.5: a) Heat release rate $\dot{Q}''$ with respect to time under air for several external heat fluxes. b) Heat release rate $\dot{Q}''$ with respect to t^+ under air for several external heat fluxes. c) Total heat release $\dot{Q}$ with respect to time under air for several external heat fluxes. d) Dimensionless total heat release $\dot{Q}^+$ with respect to t^+ under air for several external heat fluxes.

$\dot{q}''_e$	Current study	Luche *et al* [16]
35	513 ± 50.2	499 ± 238
20	367 ± 83.4	349 ± 138.5
12	287 ± 14.4	–
11	–	274 ± 116

Table 3.3: Average HRR in kW/m^2 for the current study and comparison of with the literature.

3.3.2 Effective heat of combustion

The effective heat of combustion $\Delta H_{c_{eff}}$ is defined as the ratio between the averaged heat release rate $\dot{Q}''$ and the specific mass loss rate $\dot{m}''$ as described in Equation 3.3.2. This subsection focuses on presenting the $\Delta H_{c_{eff}}$ values under ambient air conditions for three different irradiance levels, as detailed in Table 3.4. The values obtained range from 22.4 to $30.5 kJ/g$ and show good agreement with those reported in the literature [9, 16, 79].

$$\Delta H_{c_{eff}} = \frac{\overline{\dot{Q}''}}{\overline{\dot{m}''}} \tag{3.3.2}$$

$\Delta H_{c_{eff}}(kJ/g)$	Reference
24.7 ± 9.1	[16]
23.7 ± 6.7	[16]
25.0	[16]
24.0 ± 2.3	[16]
21.8	[9]
23.2	[79]
26 ± 4.12	Current study

Table 3.4: Average $\Delta H_{c_{eff}}$ for the current study and comparison of with the literature.

3.3.3 Gas Temperature field distribution

The gas temperature data is shown in Figure 3.6 for $\dot{q}''_e = 35 kW/m^2$, Figure 3.7 for $\dot{q}''_e = 20 kW/m^2$, and Figure 3.8 for $\dot{q}''_e = 12 kW/m^2$. It closely mirror the trends observed for the $\dot{Q}''$ and the $\dot{m}''$. The distinctive five-phase characteristics are clearly evident at the three

irradiance levels studied $\dot{q}''_e$. The first peak in the gas temperatures corresponding to the ignition phase exceeds the second peak corresponding to the decomposition of a thermally thin sample. This pattern holds for all three cases. The second peak is less marked for lower values of $\dot{q}''_e$, similar to the trends observed for both $\dot{q}''$ and $\dot{m}''$.

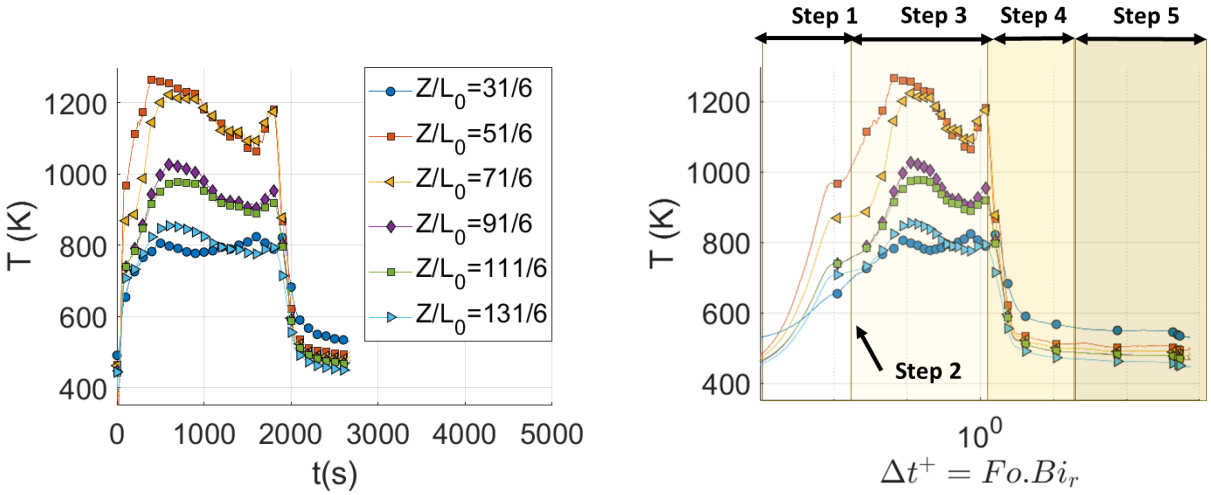

(a) (b)

Figure 3.6: a) Gas temperatures T with respect to time under air. b) Gas temperatures T with respect to t^+.

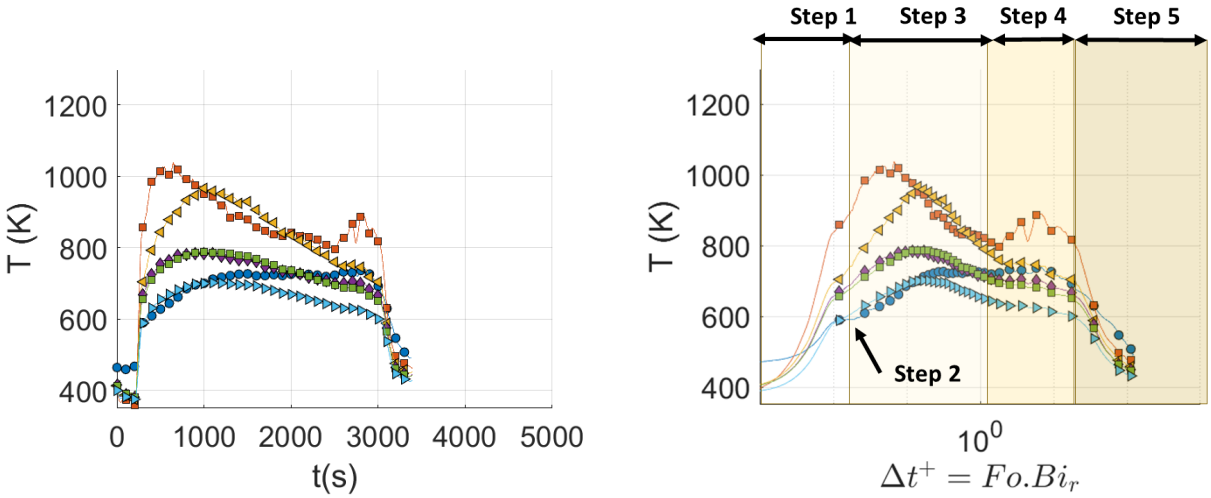

(a) (b)

Figure 3.7: a) Gas temperatures T with respect to time under air. b) Gas temperatures T with respect to t^+ under air.

It's worth noting that in all three cases the lowest thermocouple, located at a $Z/L_0 = 31/6$

and closest to the sample, does not record the highest temperatures, but comparatively lower values. This observation suggests the possibility that the lowest thermocouple is located below the reactive diffusion zone of the flame, where temperatures are significantly lower. The other thermocouples show a consistent decreasing temperature trend, starting from $Z/L_0 = 17/2$ and continuing toward the end of the stack. The gradual decrease in temperature along this trajectory provides insight into the vertical distribution of gas temperatures within the chimney. This temperature trend is a good indicator of the overall flame behavior. Lower temperatures in this context indicate a more intermittent flame, whereas higher temperatures indicate a more sustained and persistent flame, particularly in the vicinity of the sample.

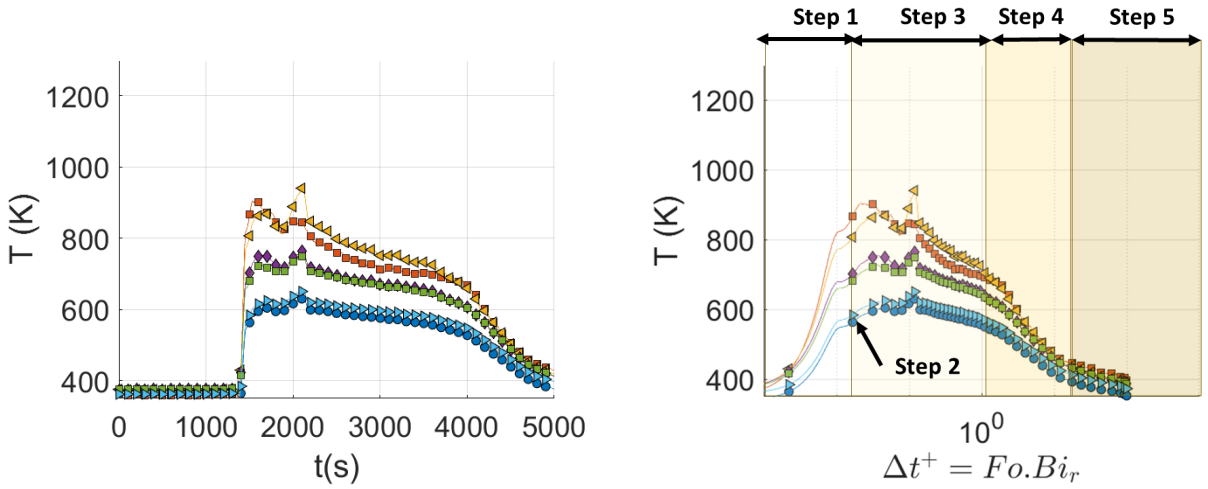

(a) (b)

Figure 3.8: a) Gas temperatures T with respect to time under air. b) Gas temperatures T with respect to t^+.

For a better representation, the time-averaged gas temperature, designated as $\overline{T}$ is presented in Figure 3.9a. A considerable difference between the highest and lowest irradiance levels is recorded. The highest time-averaged gas temperature detected was $1043K$ which is close to the values reported by *Alibert et al.*[36] $(1087 \pm 20)K$, *Kacem et al.* [35] $1100K$ and Beaulieu and Dembsey $(1184 \pm 100)K$ [30] for PMMA flames. In this section, a dimensionless gas temperature parameter T^+ is introduced and is given by Equation 3.3.3.

$$T^+ = \frac{T - T_\infty}{T_\infty} \tag{3.3.3}$$

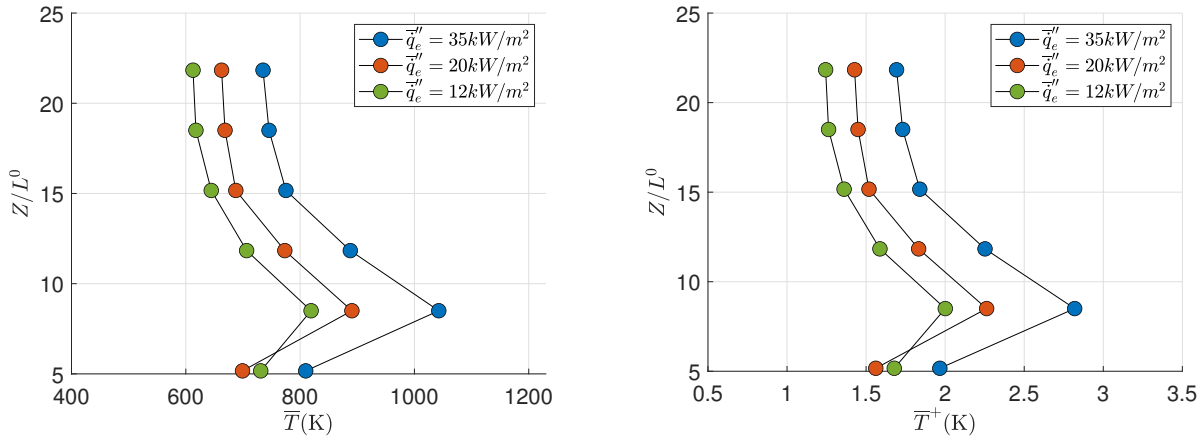

(a) (b)

Figure 3.9: a) Averaged gas temperature $\overline{T}$ at several heights in the chimney. b) Averaged dimensionless gas temperature $\overline{T}^+$ at several heights in the chimney

Where T_∞ is the ambient temperature in K.

The dimensionless gas temperature is represented in Figure 3.9b. This representation allows the comparison with ambient temperature. For example, the highest temperature recorded at $\dot{q}''_e = 35kW/m^2$ is $1043K$ which is 2.8 times the ambient temperature. For the lowest heat flux, the gas temperature high in the chimney recorded low values that were slightly higher, 1.2 than the ambient temperature. At the same positions, the temperatures go as high as 1.7 times the ambient temperature.

3.3.4 Irradiance level at the surface of the specimen

In this section, the heat flux at the surface of the sample is studied. A fluxmeter was inserted in the center of a hollowed PMMA sample to assess the irradiance level received at the surface of the sample. Similar to the trends observed in the heat release rate, specific mass loss rate, and gas temperatures, the evolution of the heat flux over time follows a consistent pattern at all three irradiance levels studied as shown in Figure 3.10. The evolution of the heat flux shows five distinct phases.

- Step 1: This phase is characterized by a slab only evident for the lowest $\dot{q}''_e$. The initial value of the total heat flux $\dot{q}''_{tot}$ in this stage equals $\dot{q}''_e$.

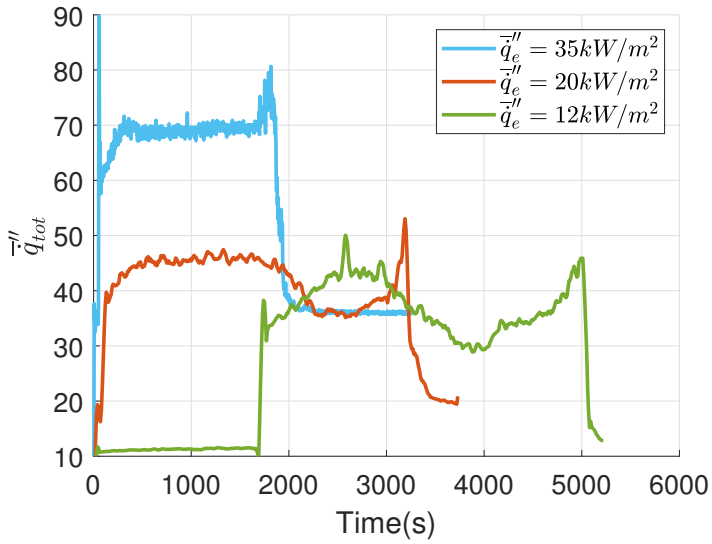

Figure 3.10: Total heat flux at the gauge for different external heat fluxes

- Step 2: There is a rapid peak in the heat flux. This spike reflects an intensified heat transfer, associated with ignition.
- Step 3: This phase is characterized by a stationary heat flux, where $\dot{q}''_{tot}$ remains relatively constant. This phase suggests a period of thermal equilibrium.
- Step 4: A peak is visible, aligning with the decomposition of a thermally thin sample. This peak represents a notable increase in heat release.
- Step 5: The final phase marks the extinction of the experiment, where $\dot{q}''_{tot}$ returns to its initial value.

It's worth noting that the presence of a hole, in which the fluxmeter is inserted, can affect the duration, ignition, and extinction times of the tests in three significant ways:

- Reduced exposed surface area: The drilling of the hole involves the removal of material, thus reducing the total exposed surface area. This change in surface geometry can affect the dynamics of heat transfer, potentially affecting the overall thermal response of the sample.

- Delayed ignition: The hole is positioned in the center of the sample, exactly where the spark plug would be. This is why, the spark plug needs to be positioned further back, and not at the center of the sample This positioning can result in variations in ignition times.

- Thermal leak: The gauge of the fluxmeter is water-cooled at $20°C$. This constitutes a cold thermal leak for the PMMA sample around it, biasing the results.

The recorded values of $\dot{q}''_{tot}$ are detailed in Table 3.5. The ratio of $\dot{q}''_{tot}$ to the fixed $\dot{q}''_e$ are represented in Figure 3.11. For cases where $\dot{q}''_e$ is set to $35kW/m^2$ and $20kW/m^2$, the heat flux absorbed by the gauge is twice the intensity imposed on the heating cone. A slight increase in this ratio is observed for $\dot{q}''_e = 12kW/m^2$. The ratio of $\dot{q}''_{tot}$ to $\dot{q}''_e$ can be expressed by a linear equation shown in Equation 3.3.4

$$\frac{\dot{q}''_{tot}}{\dot{q}''_e} = -0.0267\dot{q}''_e + 2.82 \tag{3.3.4}$$

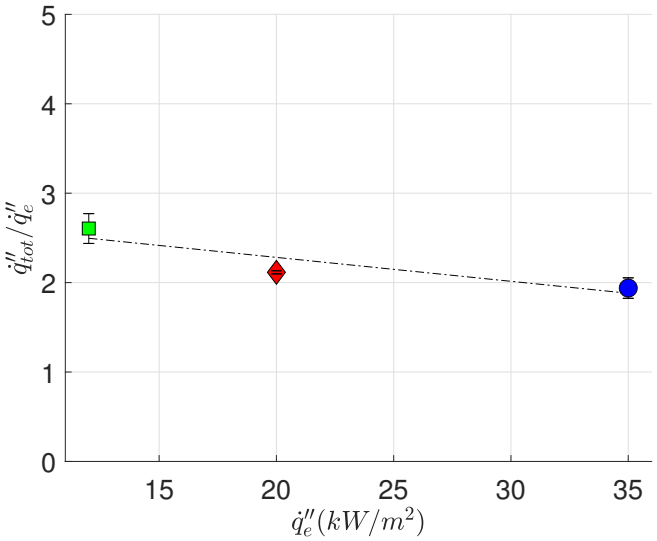

Figure 3.11: Ratio of the heat flux at the gauge $\dot{q}''_{tot}$ and the fixed heat flux at the cone $\dot{q}''_e$ for different heat fluxes

It can be considered that the difference between $\dot{q}''_{tot}$ and $\dot{q}''_e$, denoted by $\Delta\dot{q}''$ represents the heat flux contributed by the flame. The heat flux generated by the flame equals the value

initially imposed on the CACC. This observation highlights the important role played by the flame in enhancing the overall heat transfer dynamics within the experimental setup. The heat flux emphasizes the additional thermal energy introduced by the flame. However, it is noticeable that the flame heat flux is almost constant with a decreasing external heat flux.

$\dot{q}''_e(kW/m^2)$	$\dot{q}''_{tot}(kW/m^2)$	$\Delta\dot{q}''(kW/m^2)$
35	63 ± 0.86	28
20	42 ± 0.6	22
12	34 ± 0.7	21

Table 3.5: Values of $\dot{q}''_e$, $\dot{q}''_{tot}$ and $\Delta\dot{q}''$ under air for different heat fluxes

Reference	**Dimensions** (mm)	**Orientation**	**Flame heat flux** (kW/m^2)
Orloff et al. [32]	$1570 \times 410 \times 45$ $3560 \times 914 \times 64$	vertical	20 27
Quintiere et al. [37]	280×280	vertical	$19.6 - 24$
Rhodes and Quintiere [28]	100×100 (black)	horizontal	37
Tsai and Wan [38]	1000×100 1000×300 1000×500 1000×700	vertical	23.58 23.95 30.04 30.21
Leventon and Stoliarov [39]	50×150	vertical	35 and 40
Beaulieu and Dembsey [30]	$diameter = 100$ $diameter = 178$ $diameter = 610$ $diameter = 1220$	horizontal	20 31 47 60
Pizzo et al. [34]	$height = 25$ $height = 200$	vertical	23.4 30.9
Kacem et al. [35]	200×200 400×400	horizontal	40.9 59.5
Alibert [36]	100×100 200×200 400×400	horizontal	24 36.5 63
Current study	100×100	horizontal	$21 - 28$

Table 3.6: Flame heat flux comparison between the current study and the literature.

The flame heat flux values obtained in the current study are compared with values from the

literature in Table 3.6. The values of the current study are very close to the one from the literature.

3.4 Conclusion

This first chapter addresses the experimental results obtained under air conditions and, for three external heat fluxes. The parameters studied are both characteristics of the solid phase and the gas phase, like the mass loss, the in-sample heating, the heat release, and the heat flux received at the surface of the PMMA sample. The ignition times increased in a hyperbolic trend with the decrease of the heat flux. The critical heat flux to ignition is determined to be $11.5 kW/m^2$. A dimensionless time was introduced that allowed the results under different heat fluxes to be compared at the same scale. The parameters studied in both solid and gas phase showed a consistent decrease with the heat flux. The five steps of the thermal decomposition of the PMMA were visible in the kinetics of the heat release rate, the total heat release, the mass fraction, the mass loss rate, the gas temperatures and the total heat flux. The values obtained are in good agreement with the results from the literature. This chapter will serve as a comparative basis for the following chapter, where the same parameters are studied under several reduced oxygen concentrations.

CHAPTER 4
THERMAL BEHAVIOR OF PMMA IN UNDER-OXYGENATED ATMOSPHERES

Table of Contents

This chapter focuses on the effect of vitiation and external heat flux on the thermal decomposition and the combustion of the PMMA. The solid phase section involves a study of mass transfer and temperature evolution within the PMMA sample. The gas phase analysis focuses on the heat release, the spatial distribution of gas temperatures and the heat flux received at the sample surface. This chapter is divided into two main sections. The first one examines the influence of the oxygen concentration and the next one examines the combined effects of both vitiation and external heat flux.

4.1 Behavior of the PMMA in under-oxygenated atmospheres

This section focuses on the behavior of PMMA in under-oxygenated atmospheres, under several oxygen concentrations ranging from $X_{O2} = 0.10$ to $X_{O2} = 0.21$ at one external heat flux $\dot{q}''_e = 35kW/m^2$.

4.1.1 Behavior in the gas phase

The investigation includes an analysis of:

- The flame characteristics which sheds light on the combustion processes within the gas phase.
- The spatial distribution of gas temperatures.
- The heat release rate.

Flame observations

During the tests, a camera was positioned in front of the glass window of the CCAC in order to compare the flames colors and structures conducted at different oxygen concentrations. The images, presented in Figure 4.1, show a progression where the oxygen concentration decreases from the top to the bottom of the image. The images are cut exactly at the surface of the sample. Under ambient air conditions in Figure 4.1 a), the flame is luminous, characterized by a bright yellow color. This full flame starts at the surface of the sample and extends upwards through the chimney. This bright yellow color is caused by the oxidization of soot that causes them to radiate. At a slight decrease in oxygen concentration to an $X_{O2} = 0.15$ in Figure 4.1 b), the width of the flame decreases slightly. However, the bright yellow light and luminosity are still dominant, with the flame still emanating from the surface of the sample. A further reduction in the oxygen concentration to $X_{O2} = 0.13$ in Figure 4.1 c) shows a less full and bright flame. At this concentration, the oxygen is insufficient to oxidize the soot, reducing radiation. The flame is narrower. Its luminosity decreases and shows more intermittent behavior. At an even lower $X_{O2} = 0.12$, Figure 4.1 d), the flame is

weaker, with a reduced luminosity. It is starting to detach from the surface of the sample. At $X_{O2} = 0.11$, Figure 4.1 e), the flame is detached from the surface of the PMMA and is now anchored to the spark plug. The flame lost all of its luminosity and is barely visible. Finally, at $X_{O2} = 0.10$, no flame was observed.

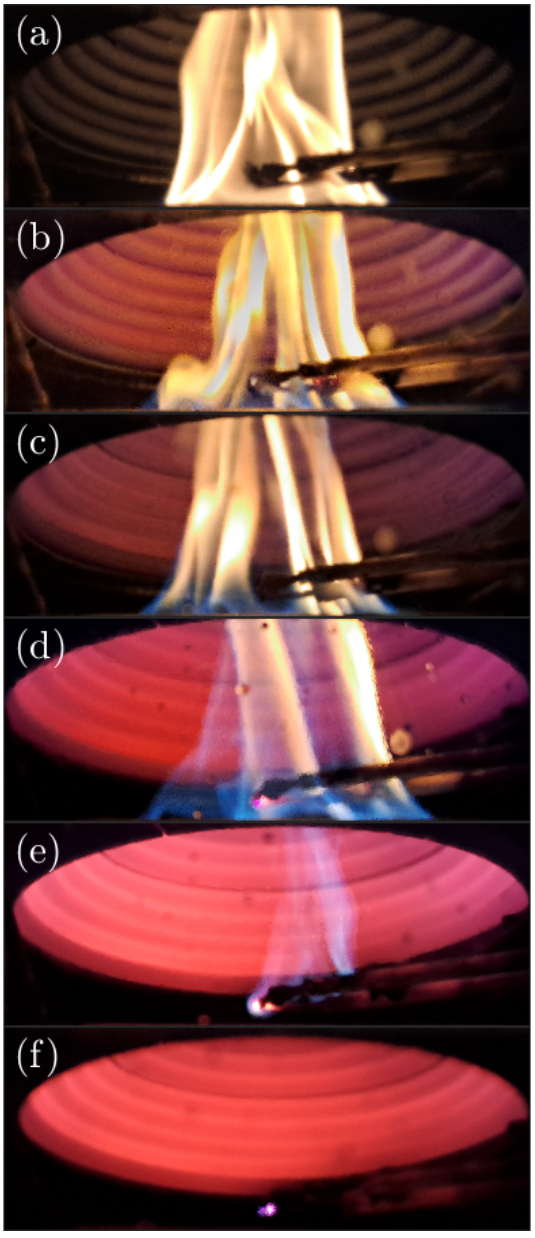

Figure 4.1: Images of the flame at different oxygen concentrations: a) $X_{O2} = 0.21$, b)$X_{O2} = 0.15$, c) $X_{O2} = 0.13$, d), $X_{O2} = 0.12$, e) $X_{O2} = 0.11$ and f) $X_{O2} = 0.10$

Gas temperature field distribution

The gas temperature field distribution is examined by inserting thermocouples at different heights in the chimney of the CACC, starting from $Z/L^0 = 31/6$ until $Z/L^0 = 131/6$. The gas temperature field distribution inside the chimney is shown in Figure 4.2a.

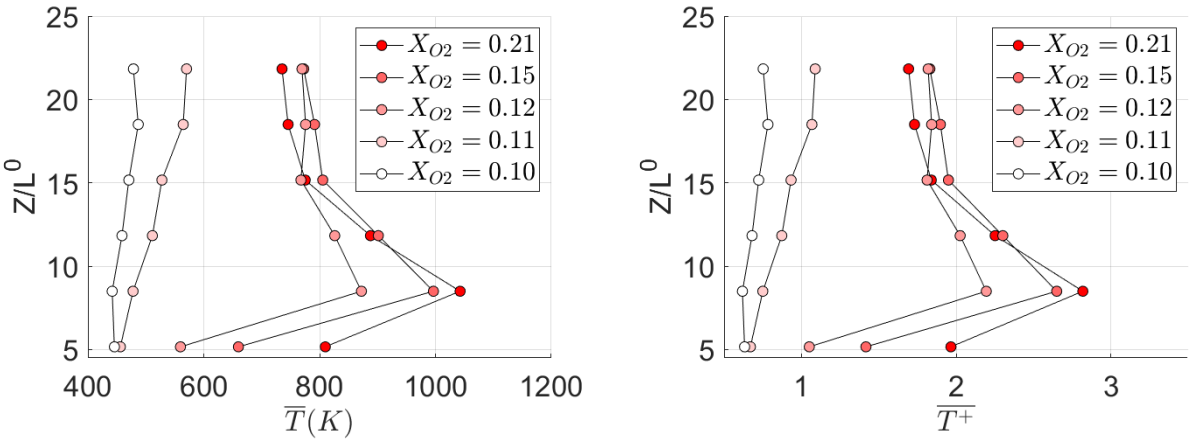

(a) (b)

Figure 4.2: a) Gas temperature evolution T through the stack. b) Dimensionless temperature evolution T^+ field distribution through the stack.

The results are consistent with those presented in the previous chapter under air, particularly for oxygen concentrations above $X_{O2} = 0.12$. In particular, the thermocouple at the lowest level, positioned at $Z/L^0 = 31/6$ and the closest to the sample, registers lower temperatures than expected, corresponding to 1 to 2 of the ambient temperature. This observation suggests that this particular thermocouple may be located below the reactive diffusion zone of the flame, where temperatures tend to be significantly lower. In contrast, the remaining thermocouples show a consistent and gradual decrease in temperature, starting from $Z/L^0 = 17/2$ and extending towards the end of the stack. The average temperatures show a decreasing trend from higher to lower oxygen concentrations, peaking at $1043K$ (3 times the ambient temperature), at $X_{O2} = 0.21$ and decreasing to $819K$ (around 2 times the ambient temperature) at $X_{O2} = 0.12$. This temperature decrease is consistent with the observations of Figure 4.1, where a brighter, wider yellow flame corresponds to higher temperatures, gradually giving way to decreasing temperatures as soot radiation decreases

and the flame weakens. Changes in the distribution of the gas temperature field occur as the oxygen concentration approaches the lower limit. At $X_{O2} = 0.11$, the temperature, at its maximum does not exceed $570K$, corresponding to less than 1 the ambient temperature at the base, and slightly exceeding 1 at the outlet of the chimney. This suggests that there might be a slight re-inflammation of the gases as they approach the outlet of the chimney and ambient air. At $X_{O2} = 0.10$, where no flame is observed, the temperatures are somewhat constant throughout the stack suggesting that this is the default temperature inside it, when no ignition happens. For better clarity, the standard deviations were not presented in the images. Details about all the values can be found in Table 4.1.

Heat release rate

The following subsection deals with heat release and examines both the heat release rate as well as the total heat release. The evolution of the heat release rate is observed over time as shown in Figure 4.3a and in terms of dimensionless time, denoted as $t+$ in Figure 4.3b.
The heat release rate shows an increase at higher oxygen concentrations, due to an increase in the thermal decomposition of the solid phase. This leads to the presence of a more substantial flame, establishing a cycle.
In the context of the representation in Figure 4.1, the presence of radiating soot, manifesting by a bright yellow flame, contributes to a higher heat flux at the surface of the material, which subsequently increases the overall thermal decomposition rate. The heat release rate profiles show a characteristic shape when the oxygen concentration exceeds $X_{O2} = 0.12$. However, there is a significant deviation as the oxygen concentration decreases, leading to the absence of the five-step heat release curve at a concentration of $X_{O2} = 0.10$. The heat release rate curve observed Figure 4.3b is explained in five steps:

- Step 1: This step is very fast for this heat flux ($\dot{q}''_e = 35kW/m^2$). The PMMA undergoes thermal decomposition. If the oxygen concentration is lower, at $X_{O2} = 0.10$, Step 1 is prolonged. No ignition is observed during this phase, with decomposition being the only process.

X_{O2}	Z/L^0	$T(K)$
0.21	31/6	810 ± 5.7
	17/2	1043 ± 55.6
	71/6	888 ± 60.3
	91/6	776 ± 44.9
	37/2	745 ± 44.3
	131/6	735 ± 34
0.15	31/6	660 ± 40.8
	17/2	997 ± 13.7
	71/6	901 ± 7.4
	91/6	805 ± 12.3
	37/2	791 ± 0.2
	131/6	773 ± 1.4
0.12	31/6	560 ± 15
	17/2	872 ± 3.8
	71/6	866 ± 5.9
	91/6	768 ± 8.6
	37/2	776 ± 12
	131/6	770 ± 3.4
0.11	31/6	456 ± 15.9
	17/2	478 ± 17.3
	71/6	511 ± 29.4
	91/6	528 ± 34
	37/2	565 ± 46.8
	131/6	570 ± 45.8
0.10	31/6	446 ± 1.1
	17/2	442 ± 0.1
	71/6	459 ± 5
	91/6	471 ± 15.8
	37/2	487 ± 36.3
	131/6	479 ± 28.5

Table 4.1: Averaged gas temperature inside the stack for several oxygen concentrations.

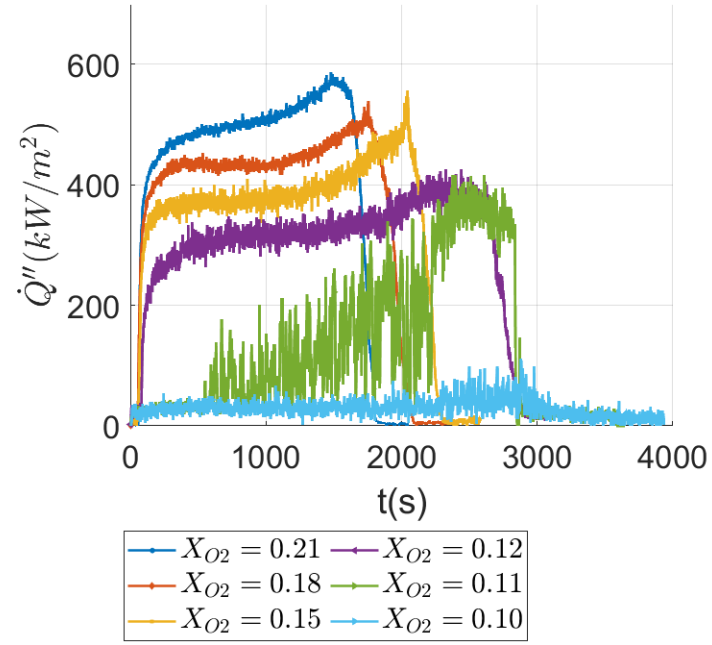

(a)

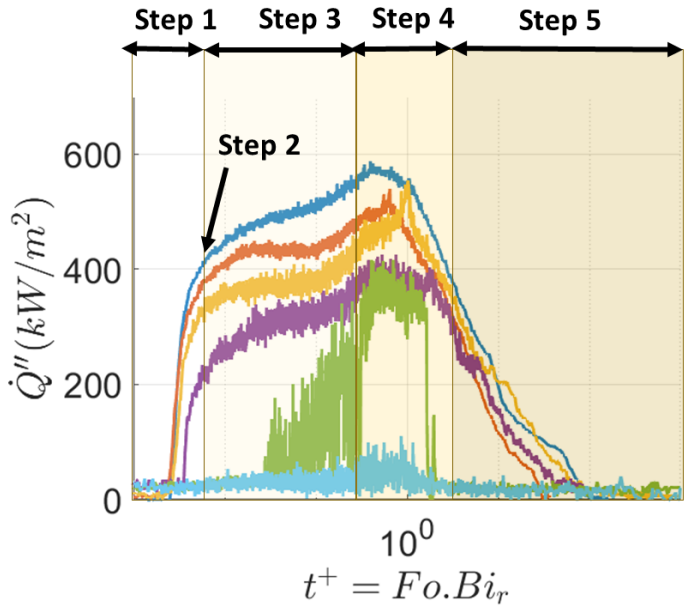

(b)

Figure 4.3: a)Heat release rate for different oxygen concentrations against t. b) Heat release rate for different oxygen concentrations against t^+.

- Step 2: The ignition is marked by a sudden increase in $\dot{Q}''$, observable when the oxygen concentrations exceeds $X_{O2} = 0.12$. The ignition time happens at the same

dimensionless time t^+ for those concentrations but shows a decreasing delayed time along with the decreasing oxygen concentration. For an oxygen concentration of $X_{O2} = 0.11$, two distinct ignition times can be identified, an unsustained ignition time where the flame is intermittent and anchored to the spark plug and a sustained ignition time where the flame propagates within the stack.

- Step 3: This step represents a stationary phase characterized by an almost constant $\dot{Q}''$ for oxygen concentrations above $X_{O2} = 0.12$. However, the duration of this step varies considerably, ranging from about $1800s$ for $X_{O2} = 0.21$ to about $2500s$ for $X_{O2} = 0.12$. This step exhibits a considerable variation in $\dot{Q}''$ for an oxygen concentration of $X_{O2} = 0.11$.

- Step 4: During this step , an experimental artifact happens at all oxygen concentrations which is the thermal feedback peak due to the insualtion of the sample holder used occurring at the same dimensionless time t^+.

- Step 5: Finally, extinction happens at different times, with lower oxygen concentrations experiencing delayed extinction events.

The transition observed in $\dot{Q}''$, shows a good agreement with the flame images presented in Figure 4.1. There is a clear and visible five-step characteristic curve, corresponding to the bright yellow flame observed under higher oxygen conditions. Conversely, the faint flame corresponds to the $\dot{Q}''$ at $X_{O2} = 0.11$.

The test at $X_{O2} = 0.11$ needs a closer look. While only one test at this oxygen concentration is shown in Figure 4.3 for clarity, this test was repeated several times. Looking at the different responses in Figure 4.4, it is clear that the three tests conducted at $X_{O2} = 0.11$ yield three different results. In particular, one of these tests shows a significantly weakened combustion response. The non-repeatability of the results highlights the critical nature of this concentration, close to the limiting oxygen concentration. The observed behavior in this particular scenario is characterized by chaos and unpredictability. This complexity of responses highlights the challenges associated with accurately predicting and understanding combustion dynamics under conditions close to the limiting oxygen concentration.

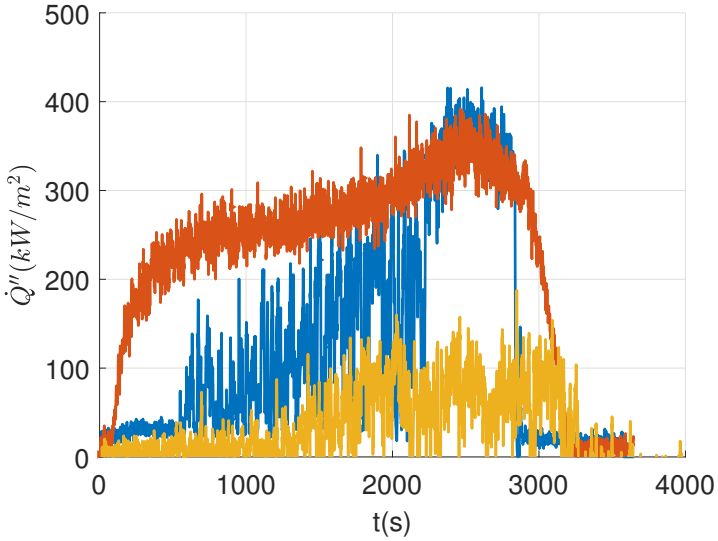

Figure 4.4: Heat release rate at $X_{O2} = 0.11$

The total heat release plots in Figure 4.5a shows a clear correlation with the oxygen concentrations. In particular, the $\dot{Q}$ peaks faster and has a steeper slope as the oxygen concentration increases. The final values of $\dot{Q}$ are between 800 and $1000MJ/m^2$ for oxygen concentrations above $X_{O2} = 0.12$. However, there is a significant decrease in the value of $\dot{Q}$ at $X_{O2} = 0.11$, where $\dot{Q}$ drops to $445MJ/m^2$, and further to $116MJ/m^2$ at $X_{O2} = 0.10$, where no flame is observed. The dimensionless representation of total heat release, $\dot{Q}^+$, shown in Figure 4.5b and plotted against the dimensionless time $t+$, reveals the five decomposition steps of PMMA combustion, which are mainly observed for oxygen concentrations above $X_{O2} = 0.12$. Additionally, this graph shows the transition happening in the flame, going from a full bright flame to a non-existent one, and highlights the combustion regime happening as the oxygen concentration drops. The $\dot{Q}^+$ reaches almost 1 under air conditions, indicating that the theoretical energy release has been attained. However, a slight decrease to about 0.9 is observed for oxygen concentrations of 0.18, 0.15, and 0.12. The dimensionless total heat release experiences a significant decrease, dropping to 0.23 at $X_{O2} = 0.11$ and reaching a minimum value of 0.1 at $X_{O2} = 0.10$. The previous subsection shows that, as stated by *Tewarson et al.* [1], a significant reduction in oxygen levels has a significant effect on flame temperatures. This leads to reduced radiative feedback reaching the PMMA surface, resulting in a reduction in

the mass loss rate.

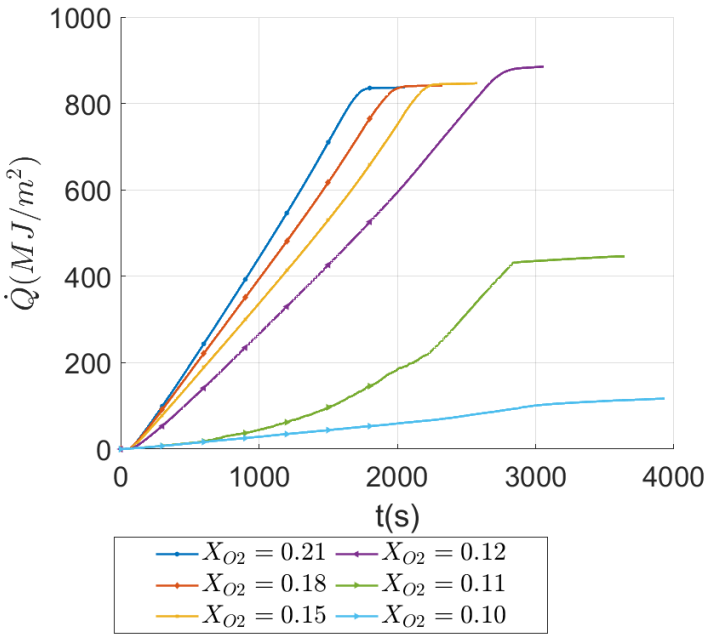

(a)

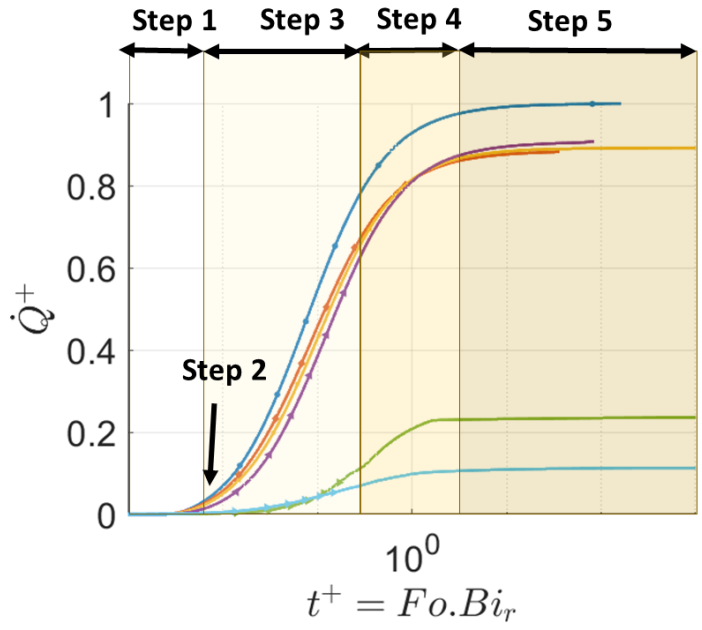

(b)

Figure 4.5: a)Total heat release $\dot{Q}$ for different oxygen concentrations with respect to t. b) Dimensionless total heat release $\dot{Q}^+$ for different oxygen concentrations with respect to t^+.

4.1.2 Behavior in the solid phase

The investigation includes an analysis of the mass transfer within the sample and the in-sample temperatures and heating rates

Mass transfer within the sample

The thermal decomposition is described through two parameters: the mass fraction Y and the specific mass loss rate $\dot{m}''$.

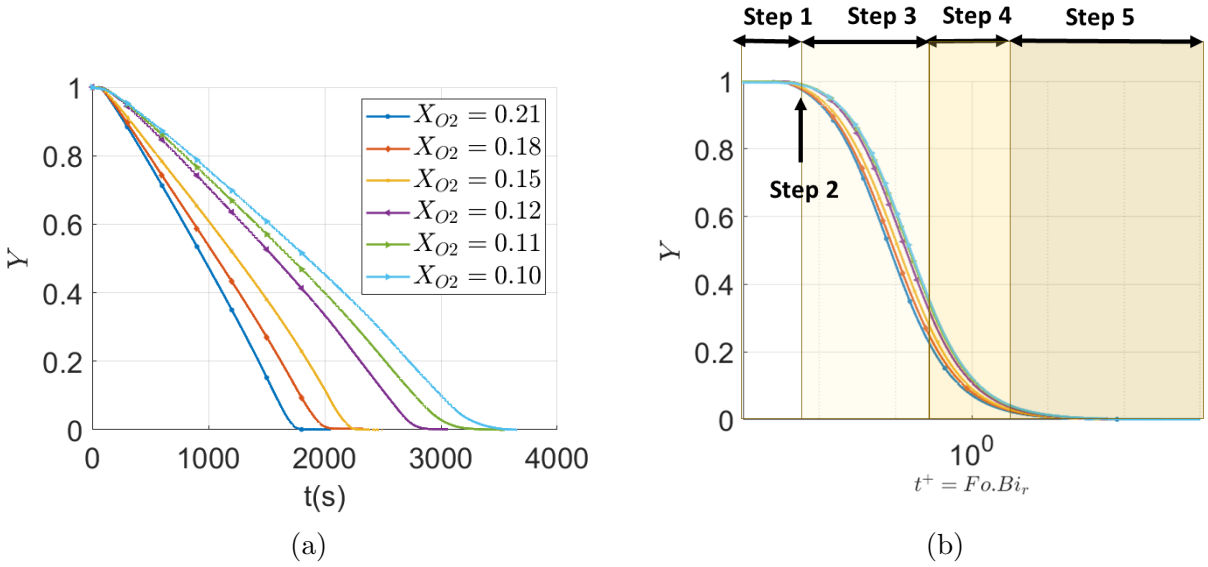

(a) (b)

Figure 4.6: a) Mass fraction Y with respect to time t. b) Mass fraction Y with respect to $t+$.

The time evolution of the mass fraction Y and the specific mass loss rate ($\dot{m}''$), as shown in Figure 4.6a and Figure 4.7a with respect to time, as well as in Figure 4.6b and Figure 4.7b with respect to $t+$. The plots show a clear correlation with the oxygen concentration parameter X_{O2}. The five steps explained prior are also observable here. The thermal decomposition of the PMMA starts when the sample is exposed to the radiant heating cone. The nucleation process starts and bubbles form and migrate to the sample surface. When the oxygen concentration exceeds $X_{O2} = 0.11$, ignition occurs, marking the start of thermal decomposition of a thermally thick sample. This phase is characterized by a line with no discernible change in slope in the mass fraction Y and a stationary phase in the specific mass loss rate $\dot{m}''$.

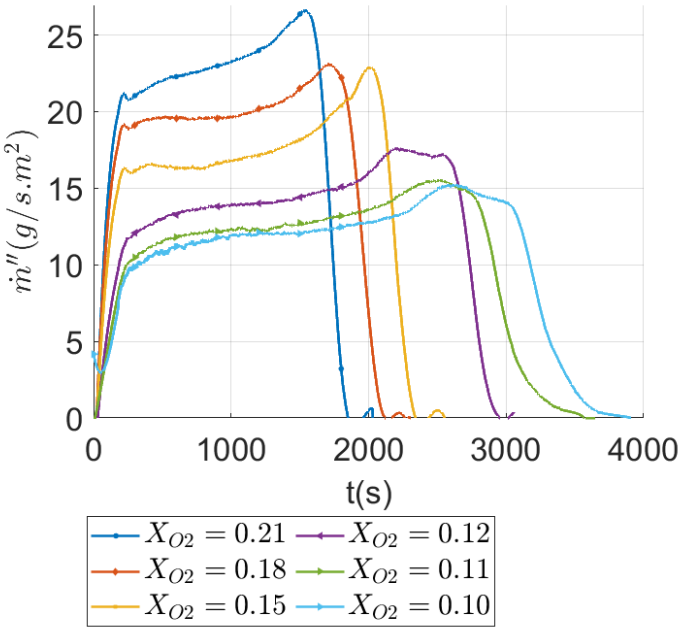

(a)

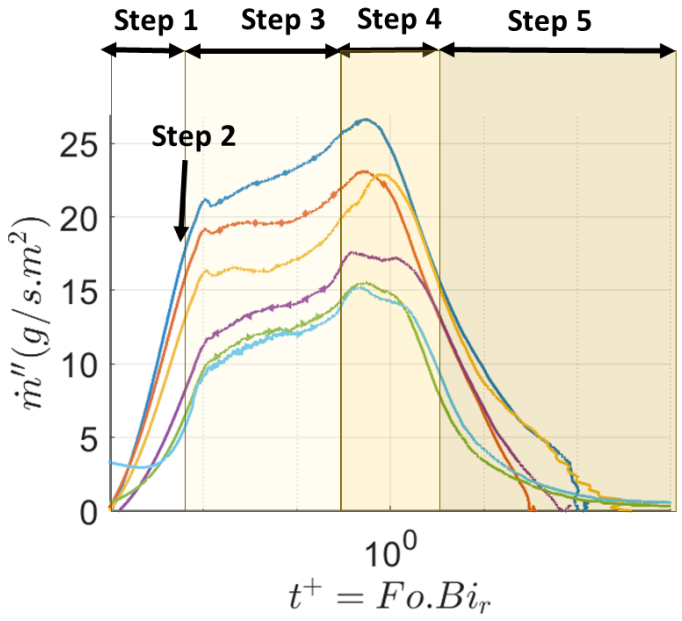

(b)

Figure 4.7: a) Specific mass loss rate $\dot{m}''$ with respect to time t. b) Specific mass loss rate $\dot{m}''$ with respect to $t+$.

The specific mass loss rate $\dot{m}''$ is particularly affected by the gas temperatures T and the

heat flux from the flame, both of which have higher values at elevated oxygen concentrations. This explains the observed decrease in the specific mass loss rate $\dot{m}''$ at lower oxygen concentrations. It is important to note that the plot of the specific mass loss rate $\dot{m}''$ for oxygen concentrations of $X_{O2} = 0.11$ and $X_{O2} = 0.10$ is similar, despite the presence of a flame at $X_{O2} = 0.11$. This suggests that at an oxygen concentration of $X_{O2} = 0.11$, the flame has minimal influence on the decomposition process.

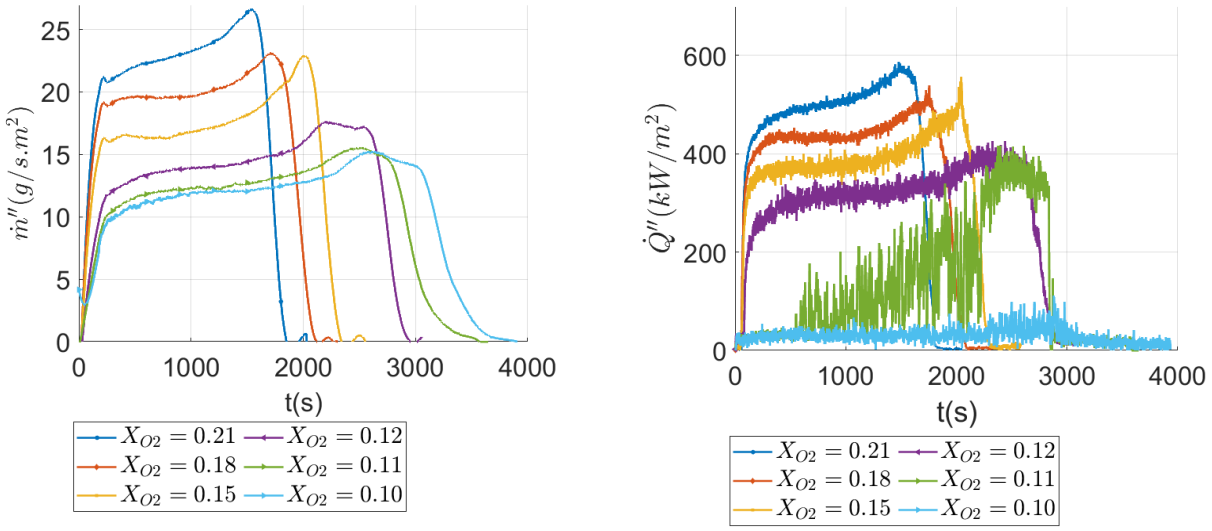

(a) (b)

Figure 4.8: a) Specific mass loss rate $\dot{m}''$ with respect to time t. b)Heat release rate for different oxygen concentrations against t.

It is interesting to compare the specific mass loss rate Figure 4.8a to the heat release rate Figure 4.8b for different oxygen concentrations. The specific mass loss rate and the heat release rate show a similar curve for high oxygen concentration. At $X_{O2} = 0.11$, there is a clear shift in the behavior of the heat release rate which is not visible in the plot of the specific mass loss rate. The heat release rate and the specific mass loss rate then cannot be correlated. This behavior is consistent with the flame images in Figure 4.1. When the flame is weak and becomes detached from the sample at $X_{O2} = 0.11$ it does not generate a similar heat release rate plot. However the sample still undergoes thermal decomposition due to the external heat flux of the radiant cone.

In-sample parameters

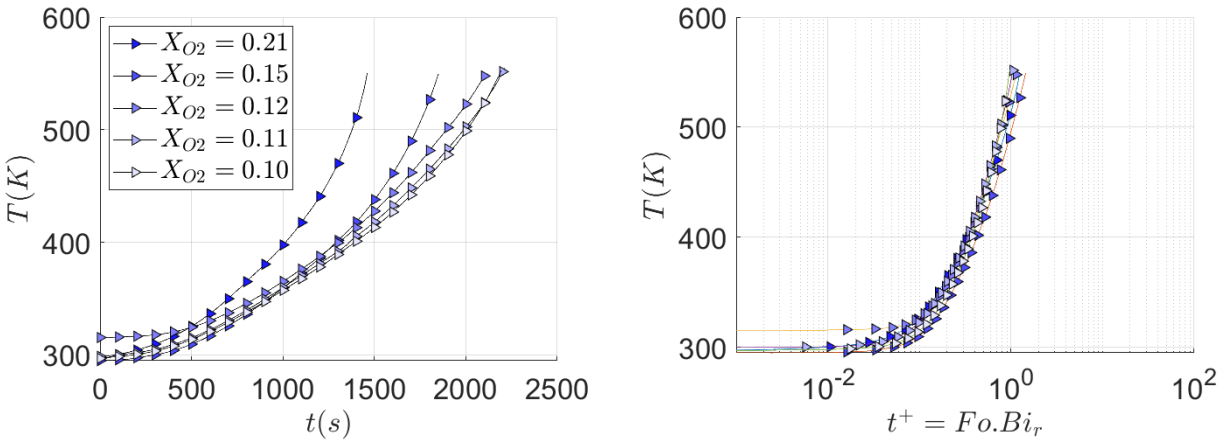

Figure 4.9: a) In-sample temperature evolution against the time t at $Z/L^0 = 5/6$. b) In-sample temperature evolution against the dimensionless time t^+ at $Z/L^0 = 5/6$.

Experiments were carried out using thermocouples placed within the material to assess the dynamics of heat transfer in a contaminated atmosphere. These thermocouples were placed at various depths, beginning at $5mm$ with an initial position of $Z/L^0 = 1/6$. In this section, the focus is on presenting the temperature kinetics and heating rate kinetics exclusively for the thermocouple located at the greatest depths $Z/L^0 = 5/6$. This thermocouple shows the heating behavior the sample throughout the depth of the sample. The temperature rise is initially gradual and then accelerates as the thermocouples approach both the pyrolysis front and the sample surface. In particular, the temperatures show a slower rise at lower oxygen concentrations, due to the material thermally decomposing at a slower rate, resulting in a slower regression of the sample surface. By eliminating the lag associated with lower oxygen concentrations, the representation in terms of dimensionless time t^+ in Figure 4.9b shows that the temperature rise within the material follows a consistent pattern regardless of oxygen concentration. Although there is a slight shift in values with decreasing oxygen concentration, the overall behavior remains similar.

The heating rates derived from the temperature measurements within the sample are plotted against both time t in Figure 4.10a and dimensionless time t^+ in Figure 4.10b. As

the thermocouple approaches the surface of the sample, there is a marked acceleration in the heating rate. Looking at the heating rate plotted against the dimensionless time t^+, a uniform behavior across different oxygen concentrations becomes apparent. Although the peak is somewhat less pronounced at lower oxygen concentrations, it remains a discernible phenomenon that manifests itself consistently across different oxygen concentrations. This suggests that, despite slight variations, the acceleration of the heating rate as the thermocouple approaches the sample surface remains a consistent feature across different oxygen concentrations. In particular, the dimensionless time plot highlights the general trends and characteristics that persist across the different conditions studied.

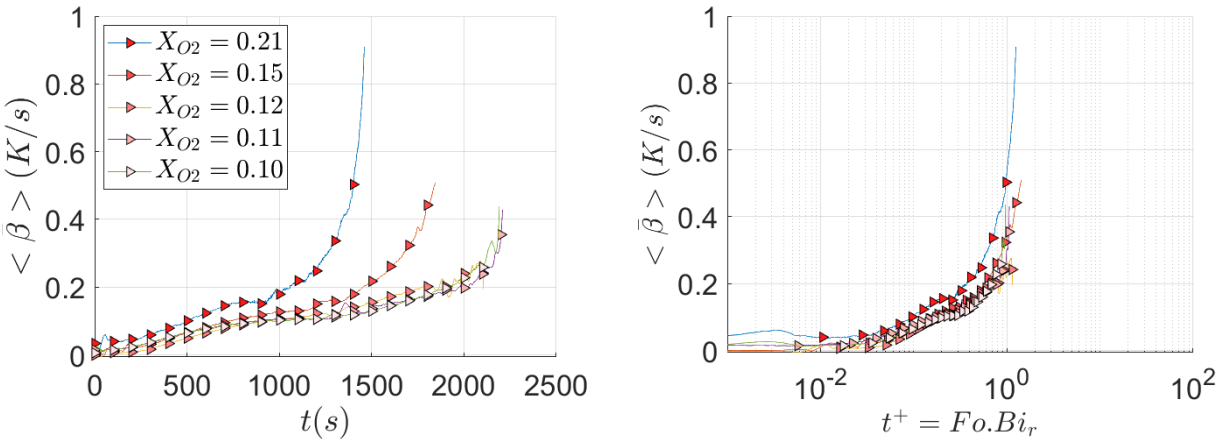

(a) (b)

Figure 4.10: a)In-sample heating-rate evolution against the time t at $Z/L^0 = 5/6$. b) In-sample heating-rate evolution against the dimensionless time t^+ at $Z/L^0 = 5/6$.

This section emphasized the effect of the oxygen concentration X_{O2} on different parameters in the solid and gas phases such as the in-sample heating rate, the mass transfer, the heat release rate, and the gas temperatures. It focuses on the kinetics of these parameters and their involvement with time through the tests under different oxygen conditions and one constant external heat flux $\dot{q}''_e = 35kW/m^2$. In the following section, the same parameters are studied under different external heat flux, to assess the combined effect of the oxygen concentration and heat flux on the thermal behavior of the PMMA.

4.2 Combined effect of the oxygen concentration and heat flux on the thermal behavior of the PMMA

The heat and mass transfers will be presented for several oxygen concentrations and three heat fluxes $\dot{q}''_e = 35$, 20, and $12 kW/m^2$.

4.2.1 Limiting oxygen concentration and critical heat flux to ignition

The oxygen concentrations used in this investigation were chosen after determining the oxygen limit for each specific heat flux condition, with a one-hour test limit specified as the criterion. When no inflammation was observed within this duration, the conditions were judged non-flammable. This study used varied heat flux levels to define a thorough flammability profile, and the results are summarized in Figure 4.11.

Establishing a clear boundary between flammable and non-flammable zones is difficult. During the test conducted, there was a degree of unpredictability when approaching critical conditions. For example, a test conducted at $\dot{q}''_e = 35 kW/m^2$ and $X_{O2} = 0.11$ could show combustion or no combustion, as shown in Figure 4.4. The presence or absence of combustion under such conditions is unpredictable. It was necessary then, to establish a critical zone, where results don't show repeatability. The limiting oxygen concentration LOC at which no ignition happened fell in the range of 0.11 to 0.12 for $\dot{q}''_e$ value of $20 kW/m^2$. The LOC was somewhat higher for the lower $\dot{q}''_e$ of $12 kW/m^2$, ranging between 0.12 and 0.13, reflecting a 0.2 increase. This growing LOC with decreasing $\dot{q}''_e$ pattern continues until no inflammation is seen even at an oxygen concentration of 0.21. The minimal heat flux is set to be $11.5 kW/m^2$. The limiting oxygen concentrations happen at different levels for the three irradiance levels studied. The values are presented in Table 4.2.

The limiting oxygen concentrations LOC follows a hyperbolic trend. A fitted model was made to describe the evolution of the LOC in the function of the external heat flux $\dot{q}''_e$. This model is detailed in Table 4.2.

$$LOC = 0.105(1 + exp^{\frac{9.5-\dot{q}''_e}{1.5}}) \tag{4.2.1}$$

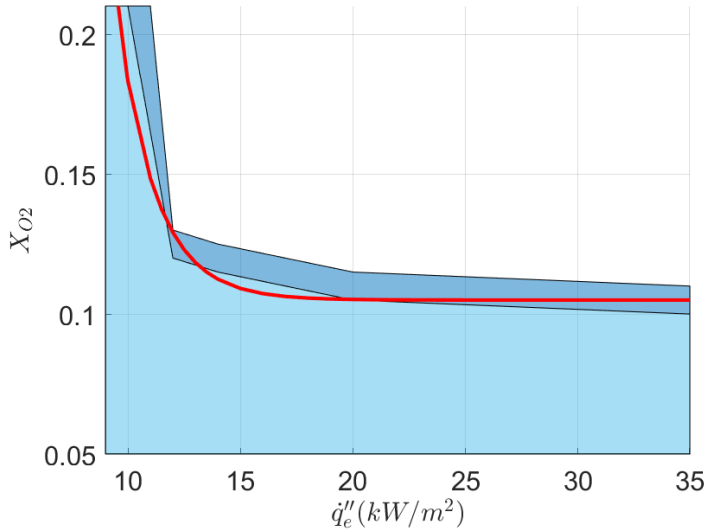

Figure 4.11: Limited oxygen concentration LOC as a function of the external heat flux $\dot{q}''_e$

$\dot{q}''_e(kW/m^2)$	X_{cr}
35	10
20	11
12	12
11	21

Table 4.2: Limiting oxygen concentration for different external heat fluxes

Where is LOC is the limiting oxygen concentration, 0.105 is a fitted parameter and corresponds to the limiting oxygen concentration X_{cr} for $\dot{q}''_e = 35kW/m^2$, 9.5 is a fitted parameter, $\dot{q}''_e(kW/m^2)$ is the heat flux fixed at the heating cone, and 1.5 is a fitted parameter.

Zhubanov and Gibov [52] studied the oxygen index for the PMMA for different external heat fluxes $\dot{q}''_e$. Although the values are not comparable due to the difference in experimental benches, the researchers found a similar hyperbolic trend.

This section focused on the limiting oxygen concentration LOC at different external heat fluxes. The LOC showed a decreasing pattern with higher heat fluxes. In the following section, the ignition and extinction times for different conditions will be discussed.

4.2.2 Ignition and extinction times

Ignition is correlated to environmental conditions, such as oxygen concentration and external heat flux. Extinction, on the other hand, marks the end of combustion and indicates in the present conditions for the PMMA that all the material has been consumed. Given the wide range of oxygen concentration and external heat flux here studied, the representation of ignition and extinction times becomes challenging. To address this, these times were expressed as $\frac{1}{\sqrt{t_{ig}}}$ and $\frac{1}{\sqrt{t_{ext}}}$ (with t_{ig} the time of inflammation and t_{ext} the one of extinction). These expressions allow for a more manageable representation, where higher values of $\frac{1}{\sqrt{t_{ig}}}$ and $\frac{1}{\sqrt{t_{ext}}}$ indicate shorter ignition and extinction times, respectively. Conversely, lower values of these parameters indicate longer ignition and extinction times. In cases where no ignition was observed, both ignition and extinction times were set to an arbitrary fixed value of 100000, defining infinity. Within the critical zone, the reported times correspond to tests where ignition occurred.

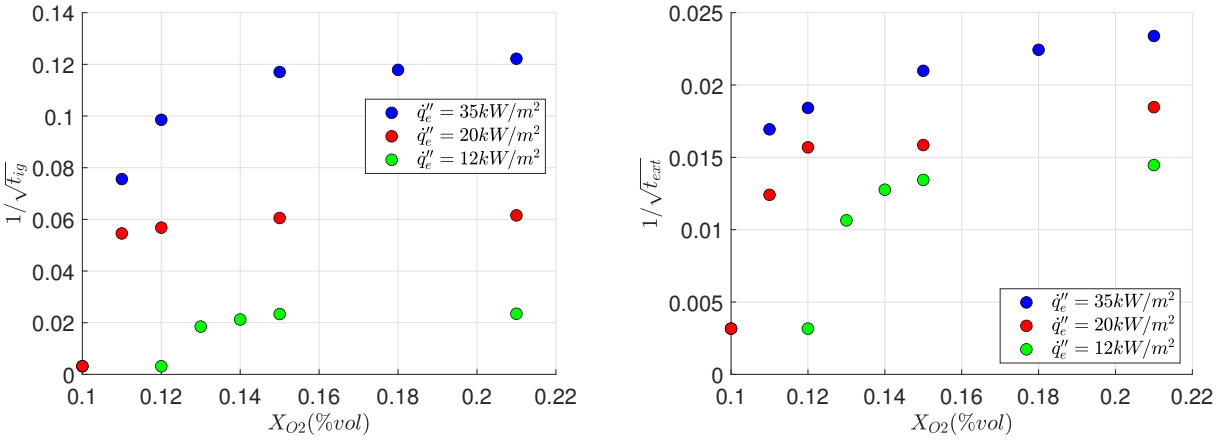

(a) (b)

Figure 4.12: a)$\frac{1}{\sqrt{t_{ig}}}$ in relation to the oxygen concentration X_{O2} for several external heat fluxes $\dot{q}''_e$ b)$\frac{1}{\sqrt{t_{ext}}}$ n relation to the oxygen concentration X_{O2} for several external heat fluxes $\dot{q}''_e$

The $\frac{1}{\sqrt{t_{ig}}}$ and $\frac{1}{\sqrt{t_{ext}}}$ are represented as a function of the oxygen concentration X_{O2} for several heat fluxes in Figure 4.12a and Figure 4.12b respectively. A discernible trend can be seen in the behavior of both $\frac{1}{\sqrt{t_{ig}}}$ and $\frac{1}{\sqrt{t_{ext}}}$, showing a consistent decrease with decreasing oxygen

concentrations. As the oxygen concentration approaches lower levels, these values become negligible, implying an infinite ignition and extinction time. In practical terms, this suggests that ignition does not occur under such conditions.

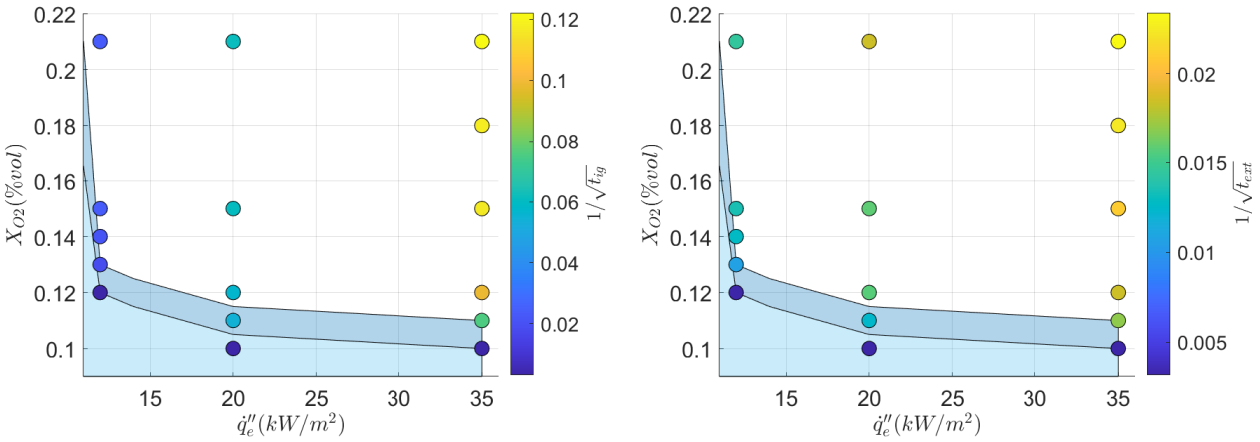

(a) (b)

Figure 4.13: a)$\frac{1}{\sqrt{t_{ig}}}$ to the oxygen concentration and the external heat flux, b)$\frac{1}{\sqrt{t_{ext}}}$ to the oxygen concentration and the external heat flux.

Furthermore, ignition time (Figure 4.13a) and extinction time (Figure 4.13b) can be expressed as functions of both oxygen concentration X_{O2} and external heat flux $\dot{q}''_e$. In this context, both $\frac{1}{\sqrt{tig}}$ and $\frac{1}{\sqrt{t_{ext}}}$ show a decrease with increasing heat flux at constant oxygen concentration. This trend is particularly pronounced as external heat flux reaches its minimum value. In this critical zone, the low heat flux at the surface of the sample not only is insufficient to sustain ignition, but also hinders the thermal decomposition of the material, making it harder to attain the lower flammability limit. Moreover, the low oxygen does not facilitate the mixing. This observed trend is in line with expectations and demonstrates the interaction of oxygen concentration and external heat flux in influencing ignition and extinction times in PMMA combustion.

However, there is a substantial lack of models describing the ignition time with the function of the oxygen concentration, which is the objective of this work. To try to get rid of the differences due to the external heat flux inducing a different limiting oxygen concentration, a dimensionless oxygen concentration parameter, denoted X^+_{O2}, is introduced by

Equation 4.2.2.

$$X_{O2}^{+} = \frac{X_{O2} - X_{cr}}{X_{air} - X_{cr}} \tag{4.2.2}$$

This parameter serves as a standardized measure, allowing a more comparative analysis of oxygen concentrations in different experimental conditions. When $X_{O2}^{+} = 0$, it means that the oxygen concentration is exactly at the critical level whereas a value of $X_{O2}^{+} = 1$ indicates that the test is carried out under ambient air conditions. Negative values of X_{O2}^{+} indicate tests performed at oxygen concentrations below the critical threshold. This dimensionless parameter provides a consistent framework for categorizing and comparing test scenarios based on their oxygen concentrations.

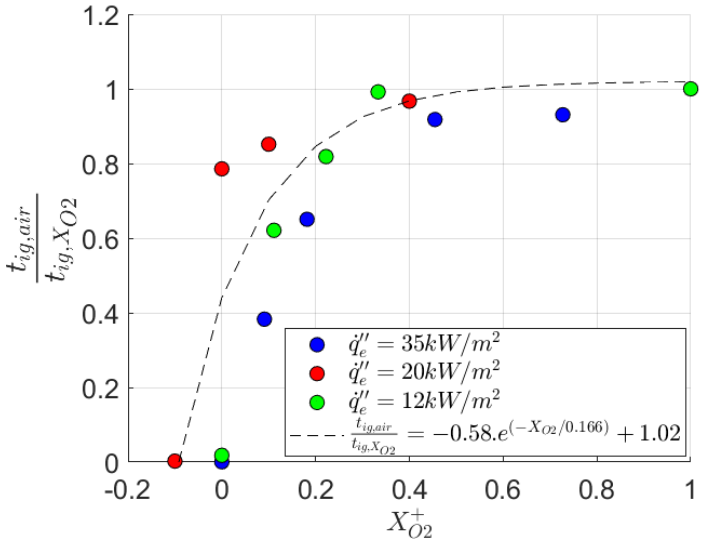

Figure 4.14: Ratio $\frac{t_{ig,air}}{t_{ig,O2}}$ as a function of the dimensionless oxygen concentration X_{O2}^{+}

In this context, the ratio $\frac{t_{ig,air}}{t_{ig,O2}}$ is introduced. The selected ratio enables a more understandable display as opposed to the traditional normalization method, which normally presents data under an oxygen concentration relative to those under air. This alternate method works well given the broad range of oxygen concentrations and external heat fluxes in this investigation. The values of $\frac{t_{ig,air}}{t_{ig,O2}}$ are plotted as a function of the dimensionless oxygen concentration X_{O2}^{+} in Figure 4.14. The data shows a noticeable decreasing trend as the dimensionless oxygen concentration decreases.

To model this trend an exponential model is derived and presented in Equation 4.2.3. The model provides a good representation of the overall trend observed in the ratio $\frac{tig,air}{t_{ig,O2}}$. Furthermore, the model shows a satisfactory fit for $X_{O2}^{+} > 0.2$, demonstrating its reliability within this range. However, as X_{O2}^{+} approaches and falls below 0.2, the data becomes sparser, indicating a degree of unpredictability. This behavior is logical considering that the data is approaching the limiting oxygen concentration where it becomes difficult to accurately predict combustion conditions.

$$\frac{t_{ig,air}}{t_{ig,O2}} = Ae^{\frac{-X_{O2}^{+}}{B}} + C \tag{4.2.3}$$

Where A, B and C are fitted parameters respectively equal to -0.58, 0.166, and 1.02.

4.2.3 Mass transfer

This subsection focuses on the effect of both the oxygen concentration and the external heat flux on the specific mass loss rate of the PMMA. The calculation of the averaged specific mass loss rate is challenging, especially at lower heat fluxes. Figure 4.15 shows the evolution of the mass loss rate over time for two different oxygen concentrations, $X_{O2} = 0.21$ and $X_{O2} = 0.14$, under $\dot{q}_e'' = 12kW/m^2$. The plot shows a delayed peak in the mass loss rate, occurring at least $1000s$ for $X_{O2} = 0.21$ and $2000s$ for $X_{O2} = 0.14$. During this pre-ignition phase, the sample undergoes thermal decomposition from the cone heat flux without combustion. To account for this, the method described previously referred to as 'Method 1', may lead to an inaccurate representation of the full decomposition in this test. This error becomes negligible at higher heat fluxes where the ignition time and peak MLR are almost instantaneous. An alternative approach, referred to as 'Method 2', involves averaging the SMLR over the entire test duration, taking into account the pre-peak decomposition. Figure 4.16 illustrates the difference in averaged mass loss rate values for various oxygen concentrations at an external heat flux of $12kW/m^2$, using both Method 1 and Method 2. The averaged mass loss rate values are lower with Method 2 than with Method 1 because the second one includes decomposition before the peak of the SMLR. The difference is more

significant at higher oxygen concentrations, where the SMLR increases significantly after the peak. The difference is less pronounced in the absence of combustion. Consequently the following mass loss rate values will be calculated using method 2 for a more accurate representation.

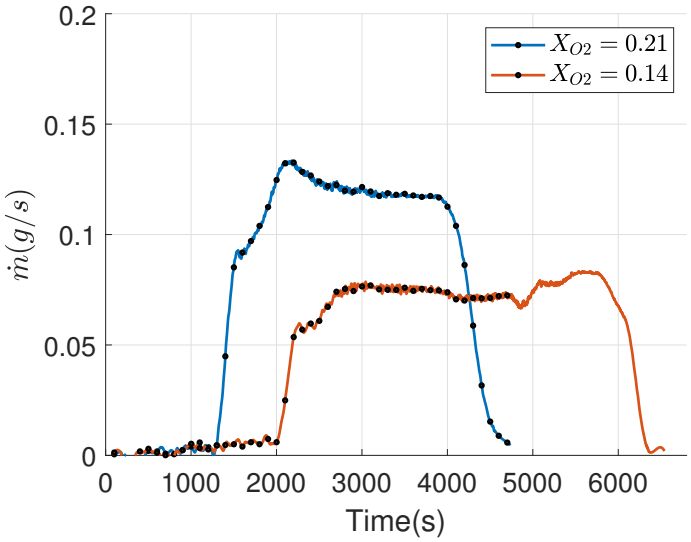

Figure 4.15: Mass loss rate for $X_{O2} = 0.21$ and $X_{O2} = 0.14$ under $\dot{q}''_e = 12kW/m^2$.

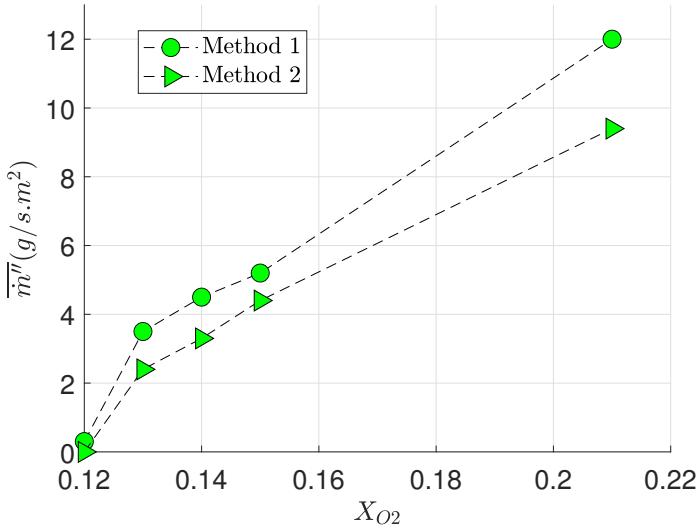

Figure 4.16: Averaged specific mass loss rate for several oxygen concentrations, under $\dot{q}''_e = 12kW/m^2$ for the two methods.

The averaged specific mass loss rate values, shown in Figure 4.17, show a linear relationship

with oxygen concentrations over different external heat fluxes.

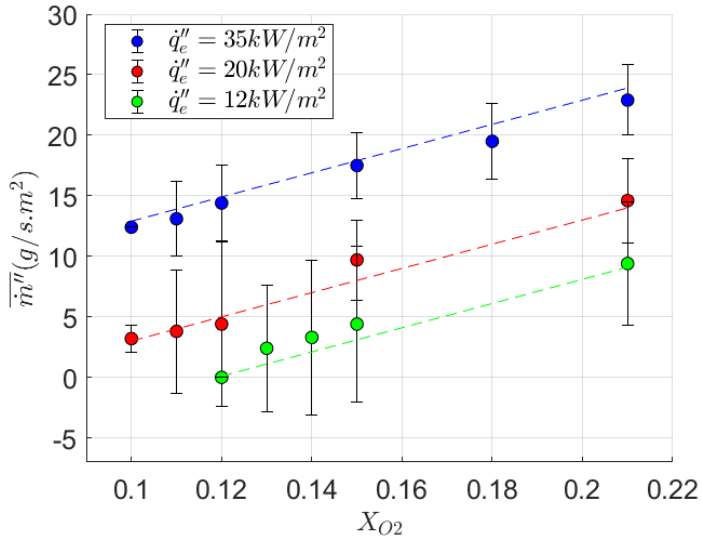

Figure 4.17: Averaged specific mass loss rate for several oxygen concentrations and external heat fluxes.

The three lines corresponding to different external heat fluxes appear parallel with a consistent slope of 100. The equations representing each line are detailed in Equation 4.2.4. This parallel behavior implies a uniform response irrespective of the external heat flux applied, with variations in values due solely to differences in heat flux at the sample surface. In particular, the standard deviation is more pronounced for intermediate values of X_{O2} at lower heat fluxes. This observation suggests a less stable and more unpredictable system under these conditions. In contrast, the system shows better stability at higher heat fluxes, e.g. for values under air and intermediate values of X_{O2} at higher heat fluxes. The variations in stability suggest that the response of the system is influenced by a complex interplay of oxygen concentration and external heat flux, with different levels of predictability under different conditions.

$$\begin{aligned} \overline{\dot{m}''} &= 100.X_{O2} + 2.9 \text{ for } \dot{q}''_e = 35kW/m^2 \\ \overline{\dot{m}''} &= 100.X_{O2} - 7 \text{ for } \dot{q}''_e = 20kW/m^2 \\ \overline{\dot{m}''} &= 100.X_{O2} - 12 \text{ for } \dot{q}''_e = 12kW/m^2 \end{aligned} \tag{4.2.4}$$

	X_{O2}	$\overline{\dot{m}''}(g/s.m^2)$
$\dot{q}''_e = 35kW/m^2$	0.21	22.9 ± 2.9
	0.18	19.5 ± 3.1
	0.15	17.5 ± 2.7
	0.12	14.4 ± 3.1
	0.11	13.1 ± 3.1
	0.10	12.4
$\dot{q}''_e = 20kW/m^2$	0.21	14.6 ± 3.5
	0.15	9.7 ± 3.3
	0.12	4.4 ± 6.8
	0.11	3.8 ± 5.1
	0.10	3.2
$\dot{q}''_e = 12kW/m^2$	0.21	9.4 ± 5.1
	0.15	4.4 ± 6.4
	0.14	3.3 ± 6.4
	0.13	2.4 ± 5.4
	0.12	0.3

Table 4.3: Average values of the specific mass loss rate $\overline{\dot{m}''}$ for different external heat fluxes and oxygen concentrations.

The values of the $\overline{\dot{m}''}$ are detailed in Table 4.3.

In the existing literature, a common method of presenting specific mass loss rates is to express the ratio $\frac{\overline{\dot{m}''_{O2}}}{\overline{\dot{m}''_{air}}}$, where $\overline{\dot{m}''_{O2}}$ is the specific mass loss rate at a given oxygen concentration and $\overline{\dot{m}''_{air}}$ is the specific mass loss rate at ambient air conditions undr a same external heat flux. As shown in Figure 4.18, this ratio has a linear and decreasing trend, reflecting the evolution of the averaged specific mass loss rate. For an external heat flux of $35kW/m^2$, $\overline{\dot{m}''_{O2}}$ is halved at the point where no combustion occurs, and for $\dot{q}''_e = 12kW/m^2$, it approaches 0 for the same condition. Three different lines in Figure 4.18 represent three different models, as detailed in Equation 4.2.5.

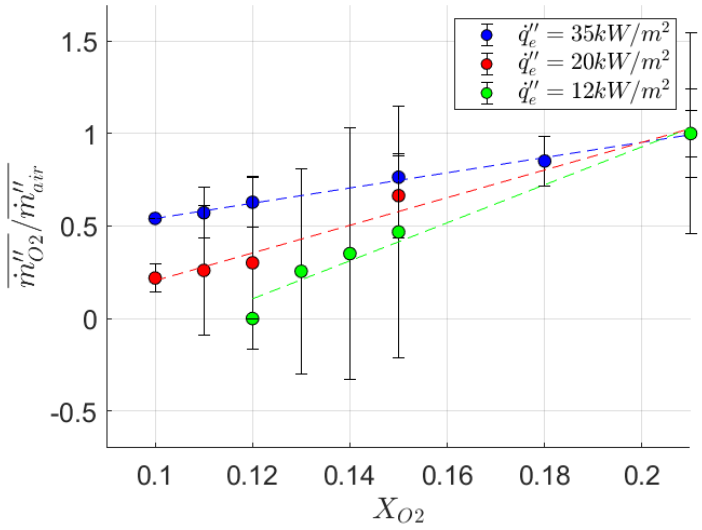

Figure 4.18: Ratio $\frac{\overline{\dot{m}''_{O2}}}{\overline{\dot{m}''_{air}}}$ for several oxygen concentrations and external heat fluxes.

$$\begin{aligned}
\frac{\overline{\dot{m}''_{O2}}}{\overline{\dot{m}''_{air}}} &= 4.12.X_{O2} + 0.13 \text{ for } \dot{q}''_e = 35kW/m^2 \\
\frac{\overline{\dot{m}''_{O2}}}{\overline{\dot{m}''_{air}}} &= 7.48.X_{O2} - 0.54 \text{ for } \dot{q}''_e = 20kW/m^2 \\
\frac{\overline{\dot{m}''_{O2}}}{\overline{\dot{m}''_{air}}} &= 10.3.X_{O2} - 1.13 \text{ for } \dot{q}''_e = 12kW/m^2
\end{aligned} \tag{4.2.5}$$

Peantross and Beyler [54] formulated a model based on Tewarson's experimental results [80], defining the ratio $\frac{\overline{\dot{m}''_{O2}}}{\overline{\dot{m}''_{air}}}$ in terms of oxygen concentration as expressed in Equation 4.2.6.

$$\frac{\overline{\dot{m}''_{O2}}}{\overline{\dot{m}''_{air}}} = 10.X_{O2} - 1.1 \tag{4.2.6}$$

Subsequently, Alibert [36] validated the Peatross and Beyler model with experimental data. Comparisons with literature values from various studies including *Mulholland et al.*[41], *Tewarson et al.* [1], Santo and Tamanini [40], Peatross and Beyler [54] and Alibert [36], are presented in Figure 4.20. The current study deviates from the model in Equation 4.2.6 and the values in [36] at high heat fluxes, but is closer to *Mulholland et al.*[41] under these conditions.

The coefficients recorded in Equation 4.2.5 for $\dot{q}''_e = 12kW/m^2$ are very similar to those found by Peatross and Beyler [54], supporting Chatenet's explanation [42] that external heat flux is a key factor in the deviation of mass loss rate ratios. The observed differences demonstrate how sensitive certain mass loss rates and related factors are to changes in experimental design. It highlights how important it is to take these things into account when analyzing and contrasting the findings of various studies.

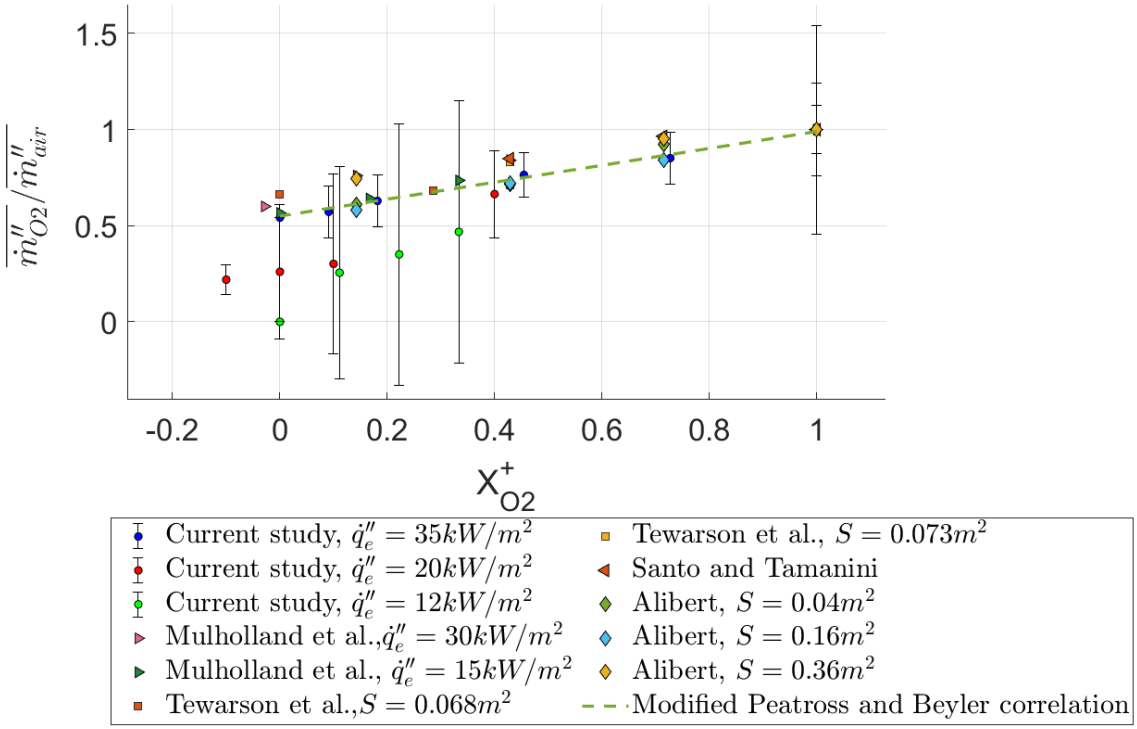

Figure 4.19: Ratio $\frac{\overline{\dot{m}''_{O2}}}{\dot{m}''_{air}}$ for different external heat flux with respect to X^+_{O2} and comparison with the literature *Mulholland et al.* [41], *Tewarson et al.* [1], Santo and Tamanini [40], Peatross and Beyler [54] and Alibert [36].

To address these discrepancies, another representation is to express the ratio of specific mass loss rates with respect to X^+_{O2}, as shown in Figure 4.19. This graph takes into account the critical oxygen concentration for each experimental condition and shows a good agreement between the values observed. As the critical oxygen concentrations are approached, the behavior of the specific mass loss rate ratio becomes complicated. The data is more scattered,

with a significant standard deviation, indicating a state of unpredictability and complexity. The observed threshold is situated around $X^+_{O2} = 0.28$. This threshold is consistent with previous observations, such as the behavior observed for $\dot{q}''_e = 35kW/m^2$ in the profiles of $\dot{q}''$ and flame characteristics discussed in the previous sections. However, before reaching this threshold, it is possible to extend the model proposed by Peatross and Beyler to include X^+_{O2}. After calculations, the modified model is detailed in Equation 4.2.7. This modified model provides a better description of the relationship between oxygen concentration, and specific mass loss rates regardless of the presence of an external heat flux.

$$\frac{\overline{\dot{m}''_{O2}}}{\overline{\dot{m}''_{air}}} = A^+ X^+_{O2} + B^+ \tag{4.2.7}$$

Where $A^+ = 0.4$ and $B^+ = 0.6$ are the fitted coefficients for the modified model of Peatross and Beyler.

A dimensionless specific mass loss rate parameter is introduced and denoted by $\overline{\dot{m}''^+}$ and detailed in Equation 4.2.8.

$$\overline{\dot{m}''^+} = \frac{\overline{\dot{m}''_{O2}} - \overline{\dot{m}''_{cr}}}{\overline{\dot{m}''_{air}} - \overline{\dot{m}''_{cr}}} \tag{4.2.8}$$

Where $\overline{\dot{m}''_{cr}}$ is the averaged specific mass loss rate at the critical oxygen concentration.

By representation the specific mass loss rate in terms of the dimensionless parameter, the results fit all on one line as shown in Figure 4.21. The found model is described in Equation 4.2.9 and shows good agreement with the results from the literature.

$$\overline{\dot{m}''^+} = X^+_{O2} \tag{4.2.9}$$

4.2.4 In-sample heating rate

This subsection focuses on the effect of both the oxygen concentration and the external heat flux on the in-sample heating rate at 5 different depths inside the PMMA sample. The heating rates $< \overline{\beta} >$ for different depths within the sample have been averaged and expressed in units of K/s. The results are presented in Figure 4.22a. The averaged heating rate is also

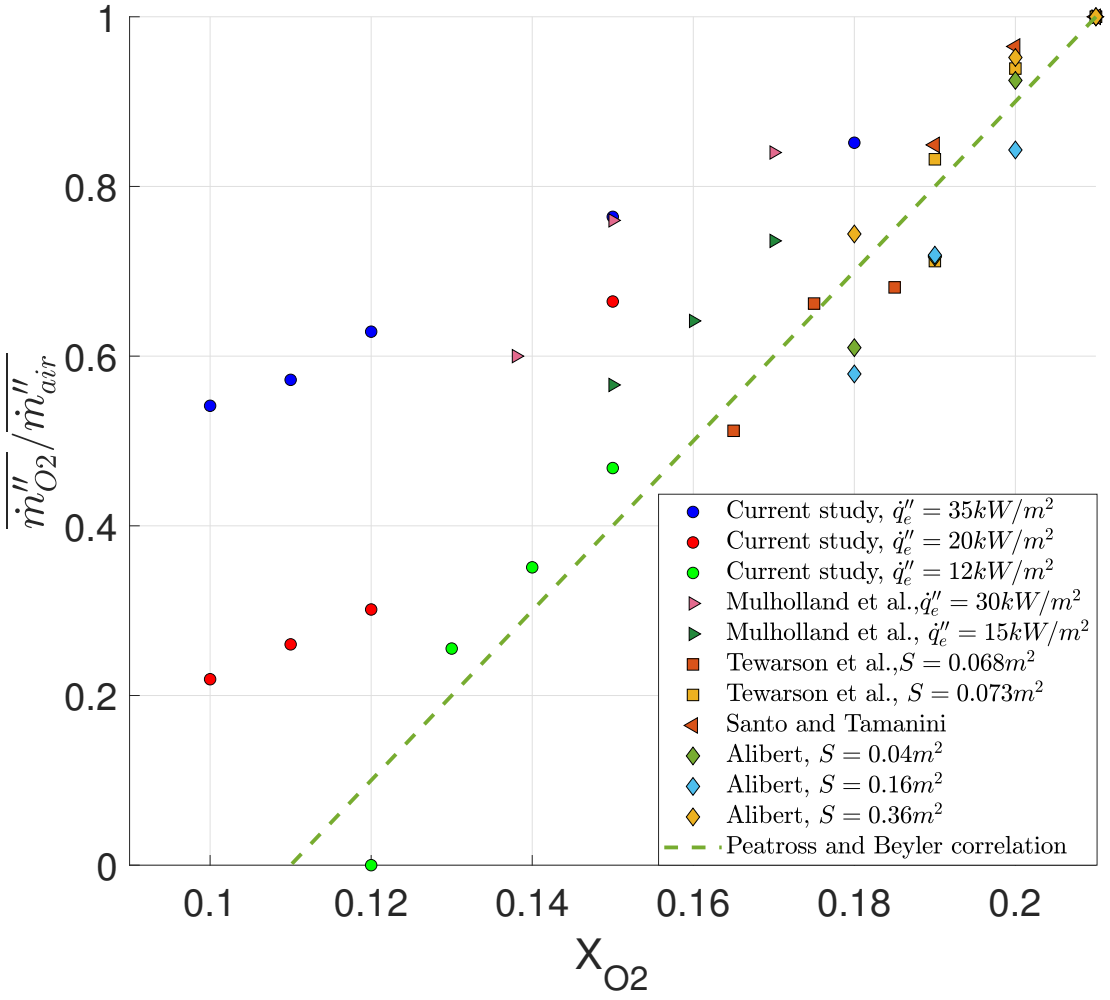

Figure 4.20: Ratio $\frac{\overline{\dot{m}''_{O2}}}{\overline{\dot{m}''_{air}}}$ for different external heat flux and from the current study and the literature: *Mulholland et al.* [41], *Tewarson et al.* [1], Santo and Tamanini [40], Peatross and Beyler [54] and Alibert [36].

.

plotted against the dimensionless oxygen concentration X^+_{O2} in Figure 4.22b.

Both plots exhibit similar trends. The $< \overline{\beta} >$ values show a discernible linear correlation with the oxygen concentration in all three heat flux conditions studied. Under ambient conditions, the maximum $< \overline{\beta} >$ value observed is $0.47K/s$ for $\dot{q}''_e = 35kW/m^2$. This value decreases significantly to $0.18K/s$ at an oxygen concentration of $X_{O2} = 0.10$, where no inflammation occurs. Furthermore, the $< \overline{\beta} >$ values at $X_{O2} = 0.10$ and $X_{O2} = 0.11$ are close, suggesting

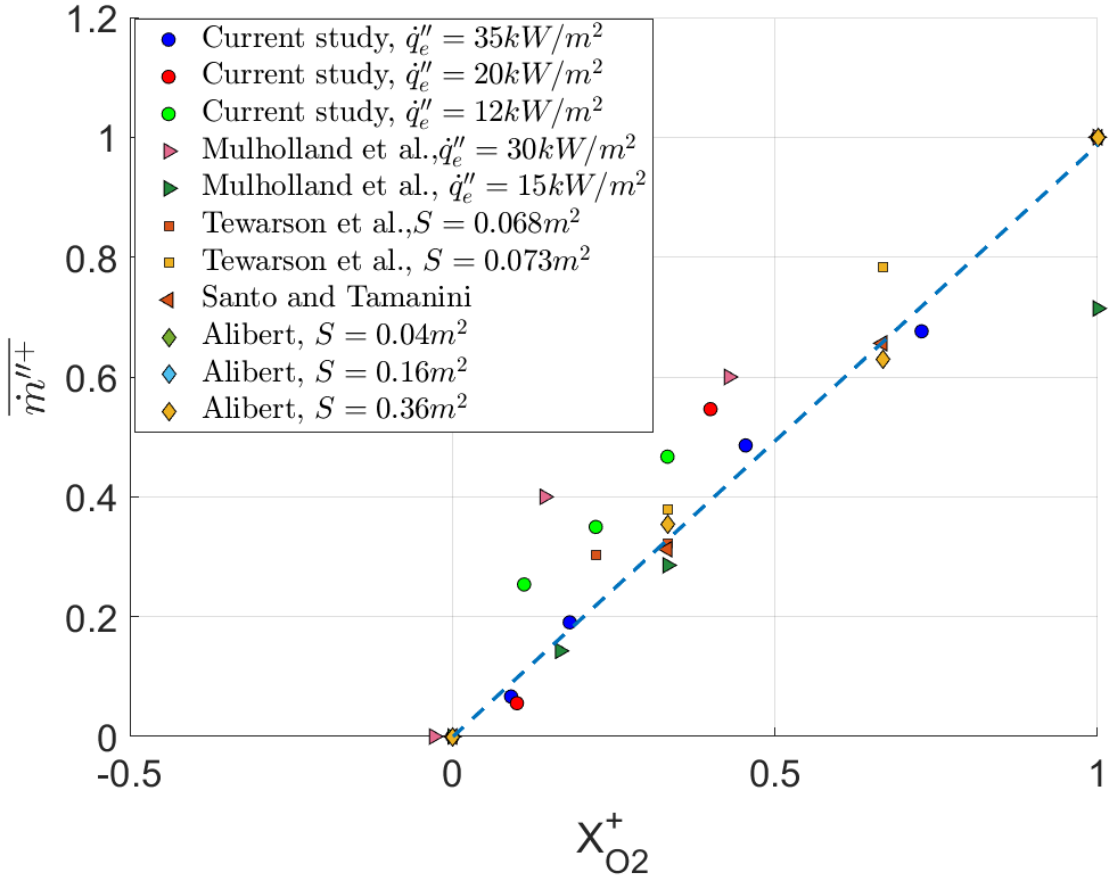

Figure 4.21: The dimensionless specific mass loss rate $\overline{\dot{m}''^+}$ for different external heat flux with respect to X^+_{O2} and comparison with the literature *Mulholland et al.* [41], *Tewarson et al.* [1], Santo and Tamanini [40], Peatross and Beyler [54] and Alibert [36].

that flames at these concentrations have a minimal effect on the decomposition rate of the material. For a heat flux of $\dot{q}''_e = 20kW/m^2$, the $< \overline{\beta} >$ values show a similar trend, decreasing from $0.30K/s$ in the air to $0.090K/s$ at the critical oxygen concentration of $X_{O2} = 0.11$. The lowest heat flux condition, $\dot{q}''_e = 12kW/m^2$, also experiences a decrease from $0.15K/s$ under ambient air to $0.044K/s$ at the critical concentration of $X_{O2} = 0.12$. Although this decrease is less marked compared to the higher heat flux conditions, it still illustrates the effect of oxygen concentration on the heating rate and highlights the sensitivity of the thermal decomposition of the material to varying environmental conditions.

The expected linear decrease in heating rate can be fully understood by examining the

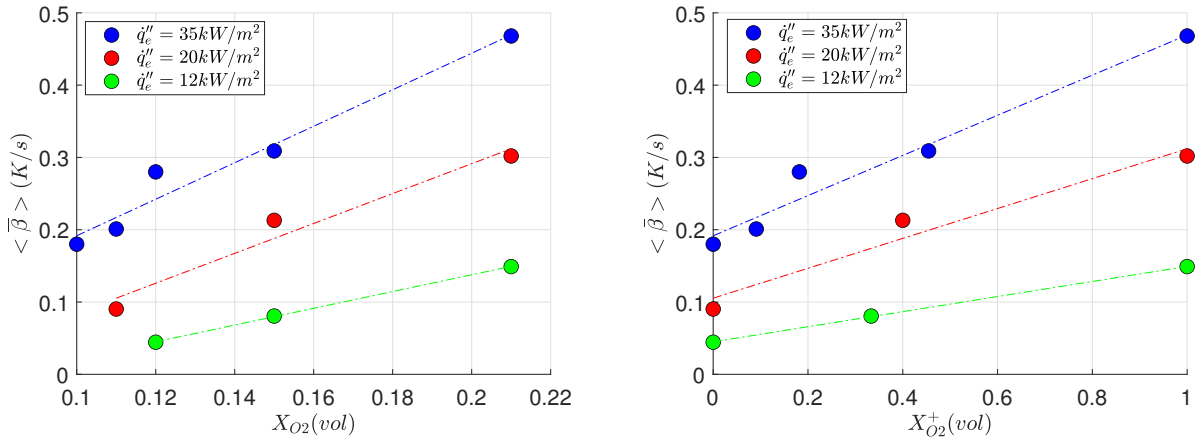

(a) (b)

Figure 4.22: a)Space-averaged in-sample heating rate $< \overline{\beta} >$ for several oxygen concentrations and heat fluxes. b) Space-averaged in-sample heating rate $< \overline{\beta} >$ against the dimensionless oxygen concentration.

relationship shown in Figure 4.23. The parameter $< \overline{\beta} >$ shows a consistent and linear decrease with $\overline{\dot{m}''}$ as shown in the equation in Equation 4.2.10. The linearity between these two parameters suggests a similar behavior with the oxygen concentration. Since $\overline{\dot{m}''}$ shows a linear evolution with respect to oxygen concentration, it can be expected that $< \overline{\beta} >$ follows a similar linear variation.

$$< \overline{\beta} >= 0.02.\overline{\dot{m}''} \tag{4.2.10}$$

Similar to the mass loss rate, the investigation extends to the ratio $\frac{<\overline{\beta_{O2}}>}{<\overline{\beta_{air}}>}$, presented in Figure 4.24a. Across the spectrum of oxygen concentrations, this ratio experiences a gradual decrease in the three heat fluxes studied. To improve the representation of this behavior, the ratio is plotted against the dimensionless oxygen concentration X^+_{O2} in Figure 4.24b. The plotted ratios exhibit a uniform linear trend line for all three heat flux conditions. The linear trend is expressed by Equation 4.2.11. Despite a slight scatter of data points away from the line when $X_{O2} < 0.28$, the overall adherence to the linear trend is good. It is noteworthy that for oxygen concentrations above 0.28, the data points closely follow the fitted linear relationship,

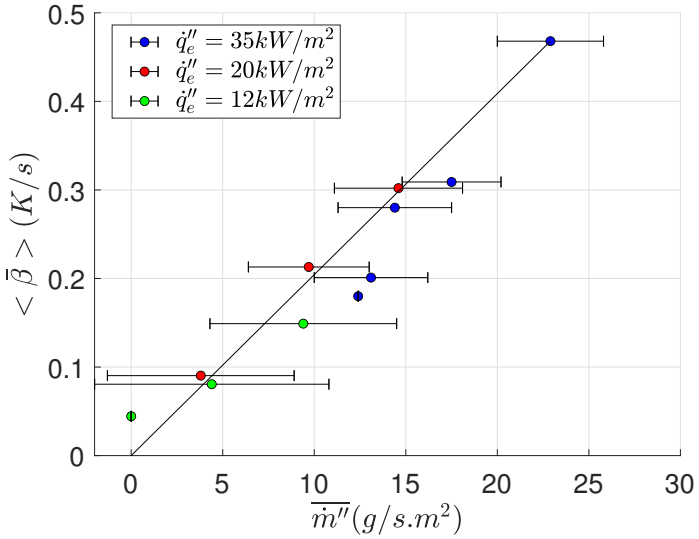

Figure 4.23: Averaged heating rate plotted against the specific mass loss rate.

$$\frac{< \overline{\beta_{O2}} >}{< \overline{\beta_{air}}} >= 0.6.X^{+}_{O2} + 0.41 \tag{4.2.11}$$

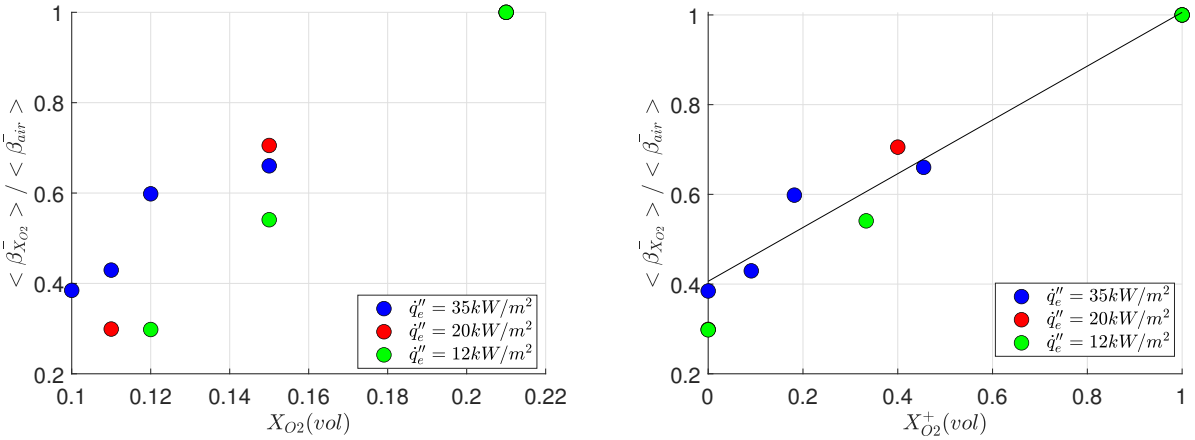

(a) (b)

Figure 4.24: a)Ratio $\frac{<\overline{\beta_{O2}}>}{<\overline{\beta_{air}}>}$ against X_{O2}. b)Ratio $\frac{<\overline{\beta_{O2}}>}{<\overline{\beta_{air}}>}$ against X^{+}_{O2}

A dimensionless heating rate parameter, denoted $< \overline{\beta^{+}} >$, has been introduced and is defined by Figure 4.25. This parameter characterizes the heating rate to the oxygen concentration and provides a normalized measure for comparison. At the critical value of X_{O2}, $< \overline{\beta^{+}} >$

reaches a minimum value of 0. Under ambient air conditions $< \overline{\beta^+} >$ reaches its maximum value of 1.

$$< \overline{\beta^+} >= \frac{< \overline{\beta_{O2}} > - < \overline{\beta_{cr}} >}{< \overline{\beta_{air}} > - < \overline{\beta_{cr}} >} \tag{4.2.12}$$

Where $< \overline{\beta_{cr}} >$ is the averaged heating rate at the ciricta value of X_{O2}, and $< \overline{\beta_{air}} >$ is the averaged heating rate under air.

The results are presented in Figure 4.25, showing a clear and linear progression with X^+_{O2}. The evolution of this dimensionless parameter can be described by Equation 4.2.13.

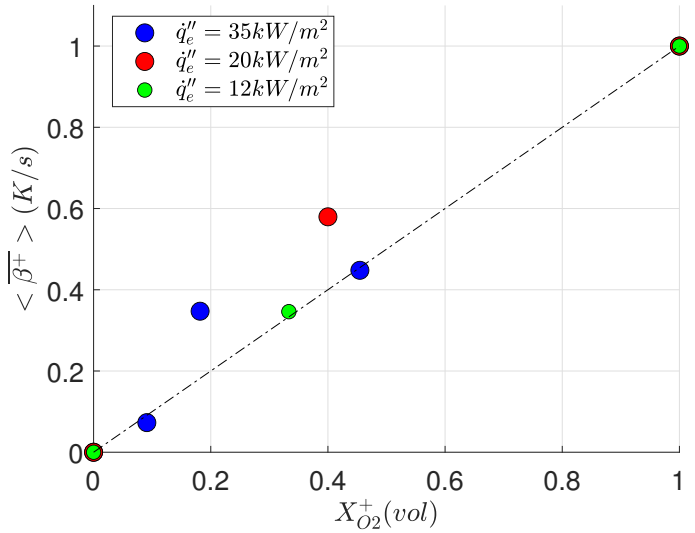

Figure 4.25: Dimensionless space-averaged in-sample heating rate $< \overline{\beta^+} >$ for several oxygen concentrations X^+_{O2} and heat fluxes

With this representation, it is sufficient to know the critical values $< \overline{\beta_{cr}} >$, and the parameter at ambient air conditions, $< \overline{\beta_{air}} >$ to be able to calculate the corresponding dimensionless heating rate, $< \overline{\beta_{O2}} >$, at any given oxygen concentration. The values of $< \overline{\beta_{cr}} >$ and $< \overline{\beta_{air}} >$ for each conditions are presented in Table 4.4.

$$< \overline{\beta^+} >= X^+_{O2} \tag{4.2.13}$$

$\dot{q}''_e(kW/m^2)$	$< \overline{\beta_{air}} > (K/s)$	$< \overline{\beta_{cr}} > (K/s)$
35	0.47	0.18
20	0.30	0.090
12	0.15	0.044

Table 4.4: $< \overline{\beta_{air}} >$ and $< \overline{\beta_{cr}} >$ for several external heat fluxes

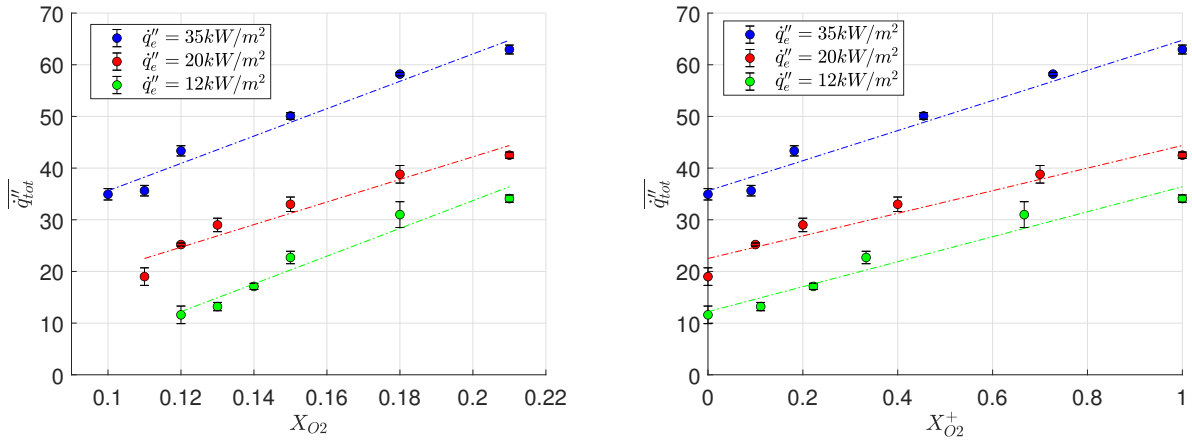

(a) (b)

Figure 4.26: a) Total heat flux at the surface of the sample $\dot{q}''_{tot}$ for different oxygen concentrations and external heat fluxes. b)Total heat flux at the surface of the sample $\dot{q}''_{tot}$ for different dimensionless oxygen concentrations and external heat fluxes

4.2.5 Heat flux at the surface of the sample

This subsection focuses on the heat flux received at the surface of the sample and the combined effect of the oxygen concentration and the external heat flux on this parameter. As shown in Figure 4.26, tests were carried out to assess the heat flux at the surface of the sample over a range of oxygen concentrations (Figure 4.26a) and the dimensionless oxygen concentration (Figure 4.27). The results showed a clear and consistent pattern between the total heat flux at the surface of the PMMA sample and oxygen concentration, across all three heat flux conditions studied. As oxygen concentrations decrease, the total heat flux linearly decreases to becomes equal to the external heat flux (the value under air is double the initial external heat flux). This highlights the importance of the flame heat flux in the total heat flux received at the surface of the sample.

The ratio of $\dot{q}''_{tot}$ to $\dot{q}''_e$ is plotted in Figure 4.27. The results show that the ratio $\dot{q}''_{tot}$ to $\dot{q}''_e$

decrease with the decreasing oxygen concentration. The total heat flux is of the same order of magnitude as the external heat flux for higher oxygen concentrations. It some cases, the total heat flux goes up to almost 3 times the external heat flux. When approaching lower oxygen concentrations that are close to the limiting concentration, the ratio become closer to 1. This suggests that the flame has a negligible influence on the overall heat balance at the sample surface.

The difference between the total heat flux $\dot{q}''_{tot}$ measured and the external heat flux $\dot{q}''_e$ is assumed to be the flame heat flux $\Delta\dot{q}''$. The flame heat flux values are presented in Figure 4.28.

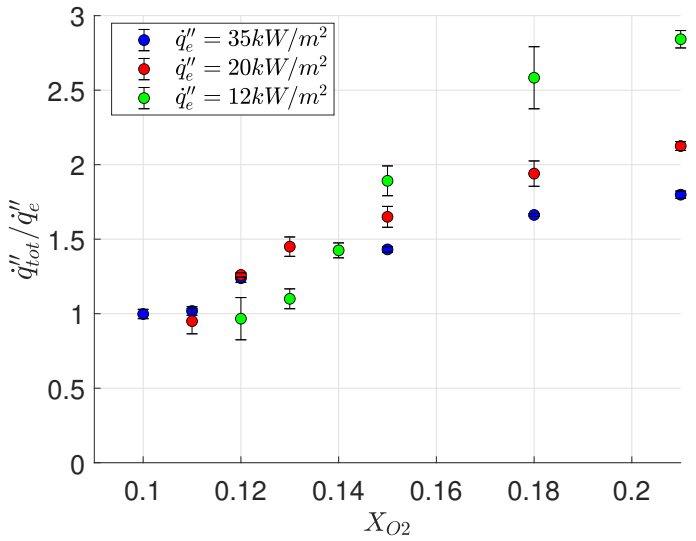

Figure 4.27: Ratio of $\dot{q}''_{tot}$ to $\dot{q}''_e$ for different oxygen concentrations and external heat fluxes

The flame heat flux shows a decrease in a linear pattern (Equation 4.2.14), starting with a value of $28kW/m^2$ for $\dot{q}''_e = 35kW/m^2$ and going down to 0 for lower oxygen concentrations. The linear pattern becomes more apparent by plotting the flame heat flux $\Delta\dot{q}''$ against the dimensionless oxygen concentration X^+_{O2} in Figure 4.29.

This linear evolution is described by Equation 4.2.14. It suggests that for a single dimensionless oxygen concentration, the flame heat flux is the same regardless of the external heat flux. The detailed values of the total heat flux $\dot{q}''_{tot}$ and the flame heat flux [36] are detailed in Table 4.5.

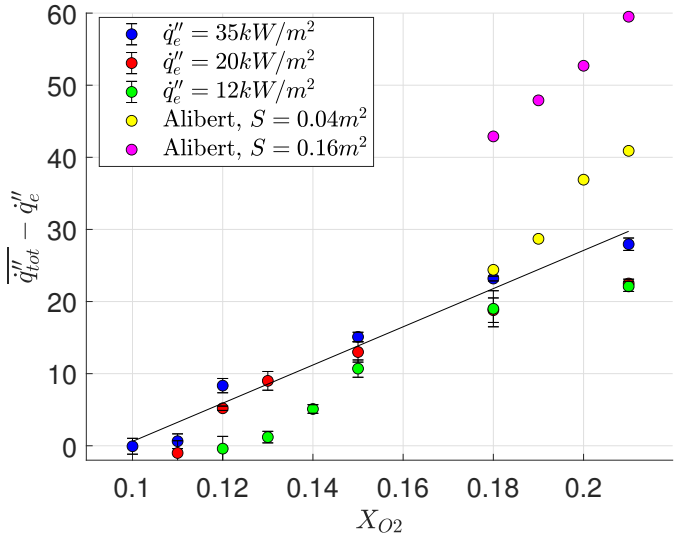

Figure 4.28: Flame heat flux $\Delta\dot{q}''$ given by $\dot{q}''_{tot} - \dot{q}''_e$ and comparison with values from reference [36].

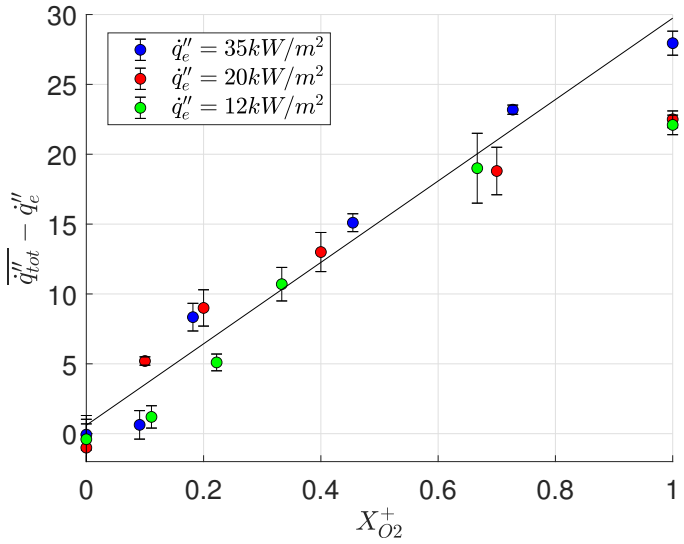

Figure 4.29: Flame heat flux $\Delta\dot{q}''$ given by $\dot{q}''_{tot} - \dot{q}''_e$ for several dimensionless oxygen concentrations X^+_{O2}.

$$\Delta\dot{q}'' = \dot{q}''_{tot} - \dot{q}''_e = 28X^+_{O2} \tag{4.2.14}$$

The comparison with Alibert's values for clear PMMA [36] in in Figure 4.28, having dimensions of $200 \times 200mm^2$ and $400 \times 400mm^2$, shows a difference due to the larger exposed

	X_{O2}	$\dot{q}''_{tot}(kW/m^2)$	[36]
$\dot{q}''_e = 35kW/m^2$	0.21	63 ± 0.86	28
	0.18	58 ± 0.33	23
	0.15	50 ± 0.64	15
	0.12	43 ± 0.99	8
	0.11	36 ± 1.02	1
	0.10	35 ± 1.1	0
$\dot{q}''_e = 20kW/m^2$	0.21	43 ± 0.6	23
	0.18	39 ± 1.7	19
	0.15	33 ± 1.4	13
	0.13	29 ± 1.3	9
	0.12	25 ± 0.3	5
	0.11	19 ± 1.7	0
$\dot{q}''_e = 12kW/m^2$	0.21	34 ± 0.7	22
	0.18	31 ± 2.5	19
	0.15	23 ± 1.2	11
	0.14	17 ± 0.6	5
	0.13	13 ± 0.8	1
	0.12	12 $pm1.7$	0

Table 4.5: Total heat flux and flame heat flux for several oxygen concentrations and externall heat fluxes.

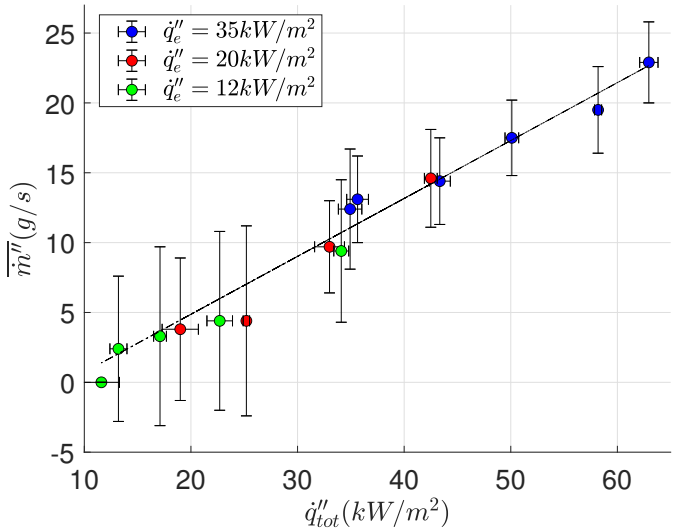

Figure 4.30: Specific mass loss rate to the total heat flux for several oxygen concentrations

surface in Alibert's samples. However, the trend observed is in line with the oxygen concentration. Indeed, Alibert observed a linear regression of the flame heat flux for both PMMA samples, confirming the similar trend observed in the current study.

The specific mass loss rate $\overline{\dot{m}''}$, is plotted in Equation 4.2.15 against the total heat flux receiced at the surface of the sample $\dot{q}''_{tot}$. The relationship between these two variables shows a linear regression, as shown in Equation 4.2.15.

$$\overline{\dot{m}''} = 0.41.\dot{q}''_{tot} - 3.5 \tag{4.2.15}$$

When the specific mass loss rate increases, it has a direct effect on both $\overline{\dot{Q}''}$, and the flame heat flux. Consequently, this increase in heat release and flame heat flux leads to an increase in the total heat flux received at the sample surface, forming a cycle. An initial increase in $\overline{\dot{m}''}$ subsequently increases $\overline{\dot{Q}''}$ and flame heat flux, resulting in increased heat flux at the sample surface. This increased heat flux in turn further increases the specific mass loss rate.

It is possible to determine the value of the heat of gasification. The slope of the line of the plot of $\overline{\dot{m}''}$ against $\dot{q}''_{tot}$ is the inverse of the heat of gasification L_G. From Equation 4.2.15, $\frac{1}{L_G} = 0.41$ and $L_G = 2.43kJ/g$. This value is in line with the ones from the literature for the PMMA which range from 1.42 to $2.77kJ/kg$ [5, 19, 30, 81, 82, 83, 84, 85, 86, 87, 88].

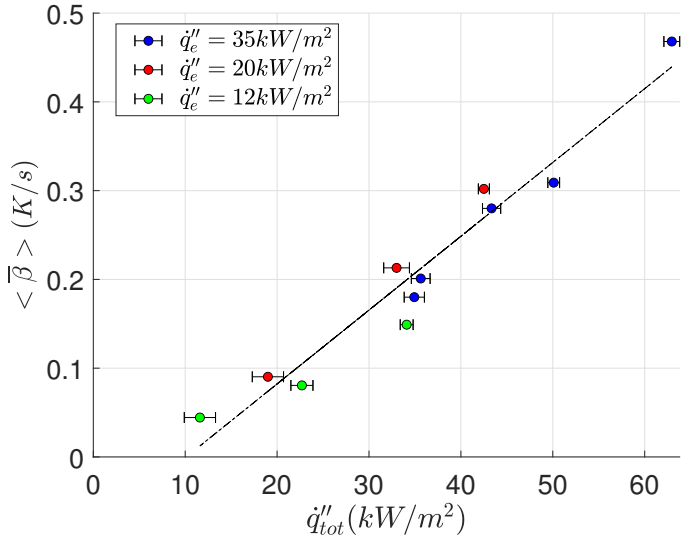

Figure 4.31: Averaged heating rate $< \overline{\beta} >$ with the total heat flux for several oxygen concentrations.

The relationship between the averaged heating rate and the total heat flux detected at the surface of the sample is represented in Figure 4.31, showing a clear linear progression as defined by Equation 4.2.16. This relationship can be anticipated by looking at the plot of the specific mass loss arte and the total heat flux. In fact, the in-sample heataing rate and the specific mass loss rate are closely related and exhibit similar behaviors.

$$< \overline{\beta} >= 0.0083\dot{q}''_{tot} - 0.0840 \tag{4.2.16}$$

4.2.6 Heat release rate

This susbection deals with the heat release rate and its behavior under several oxygen concentrations and heat fluxes. The relationship between heat release rate and oxygen concentration is shown in Figure 4.32 for various external heat fluxes.

The plots consistently show a decrease in heat release rate with decreasing oxygen concentration, as expected. This behavior mirrors the trend observed in the mass loss rate. Specifically, the heat release rate closely follows the mass loss rate, as more heat is generated by burning more material. Consequently, the higher heat release rate contributes to the overall mass

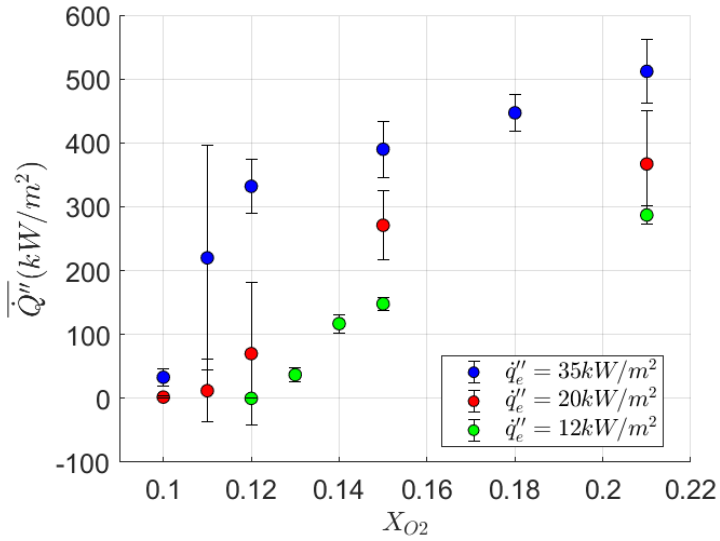

Figure 4.32: Averaged heat release rate $\overline{\dot{Q}''}$ for several oxygen concentrations and external heat fluxes.

loss rate. The highest standard deviation happens at the oxygen concentration where the transition happens, highlighting a chaotic and unpredictable behavior. The detailed values are presented in Table 4.6.

Using a similar approach to the specific mass loss rate, the heat release rate is plotted as against X_{O2} in Figure 4.33a. A consistent decrease in the heat release rate with increasing oxygen concentration is observed. For the same oxygen concentration, the ratio is higher for higher heat fluxes. The ratios are plotted against X^+_{O2} in Figure 4.33b. The ratio $\frac{\overline{\dot{Q}''_{O2}}}{\dot{Q}''_{air}}$ follows a linear trend for all heat flux conditions examined until a critical threshold is reached at $X^+_{O2} = 0.28$. At this point the ratio $\frac{\overline{\dot{Q}''_{O2}}}{\dot{Q}''_{air}}$ reaches a value of 0.63, consistent with the specific mass loss rate results. Beyond this threshold, the ratio drops significantly, reaching about 0.3 at $X^+_{O2} = 0.1$, and becoming negligible after. Above $X^+_{O2} = 0.28$, the flame is emitting a vibrant yellow color and providing a substantial heat flux to the sample surface, thereby accelerating its decomposition. Below this critical threshold, the heat flux contributed by the flame diminishes significantly, coinciding with the observed fading of the flame. This correlation underlines the influence of the oxygen concentration on the heat release rate and hence the combustion characteristics of the flame.The important standard deviation, at $X^+_{O2} = 0.1$

	X_{O2}	$\dot{Q}''(kW/m^2)$
$\dot{q}''_e = 35kW/m^2$	0.21	513 ± 50.2
	0.18	447 ± 28.2
	0.15	390 ± 44.0
	0.12	332 ± 41.9
	0.11	220 ± 176.2
	0.10	33 ± 13
$\dot{q}''_e = 20kW/m^2$	0.21	367 ± 83.4
	0.15	271 ± 54.0
	0.12	70 ± 110.9
	0.11	12 ± 49.3
	0.10	2 ± 1.6
$\dot{q}''_e = 12kW/m^2$	0.21	287 ± 14.4
	0.15	148 ± 10.5
	0.14	112 ± 14.5
	0.13	37 ± 11.3
	0.12	0

Table 4.6: Averaged values of the heat release for several oxygen concentrations and external heat fluxes.

suggests a state of increased variability and instability. This variability is indicative of an unstable flame and chaotic combustion behavior. As the oxygen concentration increases beyond $X^+_{O2} = 0.1$ there is a noticeable and significant decrease in the standard deviation. This decrease is consistent with a phase where combustion is sustained. The decreasing standard deviation underlines a more stabilized and predictable system, suggesting that the combustion behavior becomes less chaotic and more controlled as the oxygen concentration exceeds the critical value.

The total heat release (THR) calculated for each condition is plotted in Figure 4.34a over a range of oxygen concentrations. The plot shows an almost constant THR for higher oxygen concentrations, ranging from 8×10^5 to $1 \times 10^6 MJ/m^2$. This value decreases significantly as the oxygen concentration decreases and becomes negligible as the oxygen concentration approaches its limit. To further illustrate the trends associated with the THR, it is plotted against the dimensionless oxygen concentration X^+_{O2} in Figure 4.34b. This plot provides an overview of the overall heat release behavior throughout the experimental variations. The plot shows a consistent and coherent progression of the total heat release, with discernible

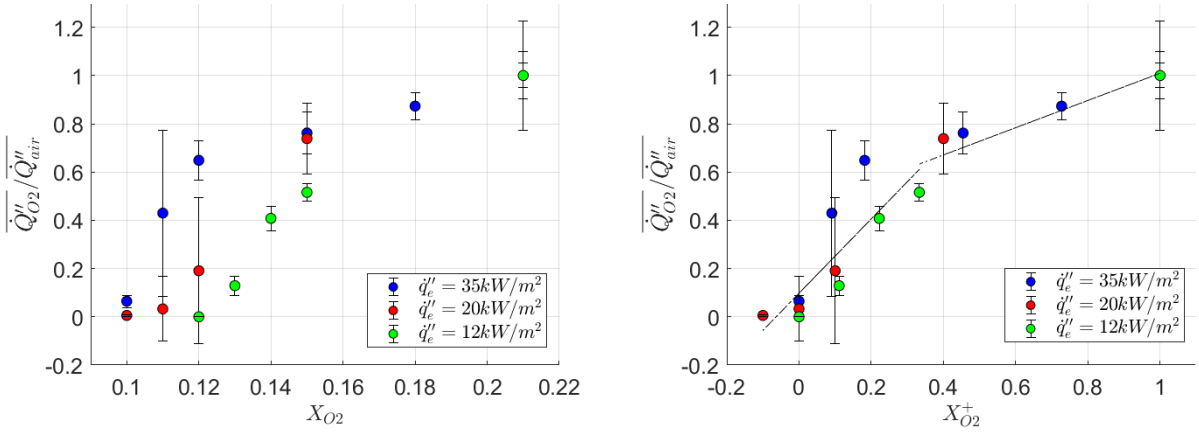

(a) (b)

Figure 4.33: a)Ratio $\frac{\overline{\dot{Q}''_{O2}}}{\dot{Q}''_{air}}$ for different external heat flux against X_{O2}. b)Ratio $\frac{\overline{\dot{Q}''_{O2}}}{\dot{Q}''_{air}}$ for different external heat flux against X^+_{O2}.

fluctuations corresponding to the previously discussed mass variations. In particular, beyond the critical oxygen concentration threshold $X^+_{O2} = 0.28$, there is a striking and sharp decrease in total heat release. This sharp decrease continues until it reaches zero at the critical oxygen concentration. This observed result is in line with expectations, given the simultaneous trend observed in the heat release rate, which also approaches zero at the critical oxygen concentration.

4.2.7 Gas temperature evolution

This section looks at the analysis of gas temperatures, as shown in Figure 4.35. We observe a consistent decrease of the temperatures with the decline of the oxygen concentrations. There is also a downward trend in gas temperatures with decreasing external heat flux. Thus, the recorded gas temperatures range from $833K$ under normal air conditions and an external heat flux of $35kW/m^2$ to $689K$ under air conditions with an external heat flux of $12kW/m^2$. The temperatures at lower oxygen concentrations drop to as low as $370K$. They show a linear decrease until a certain point where the temperatures drop. The values of the averaged gas temperatures are detailed in Table 4.7.

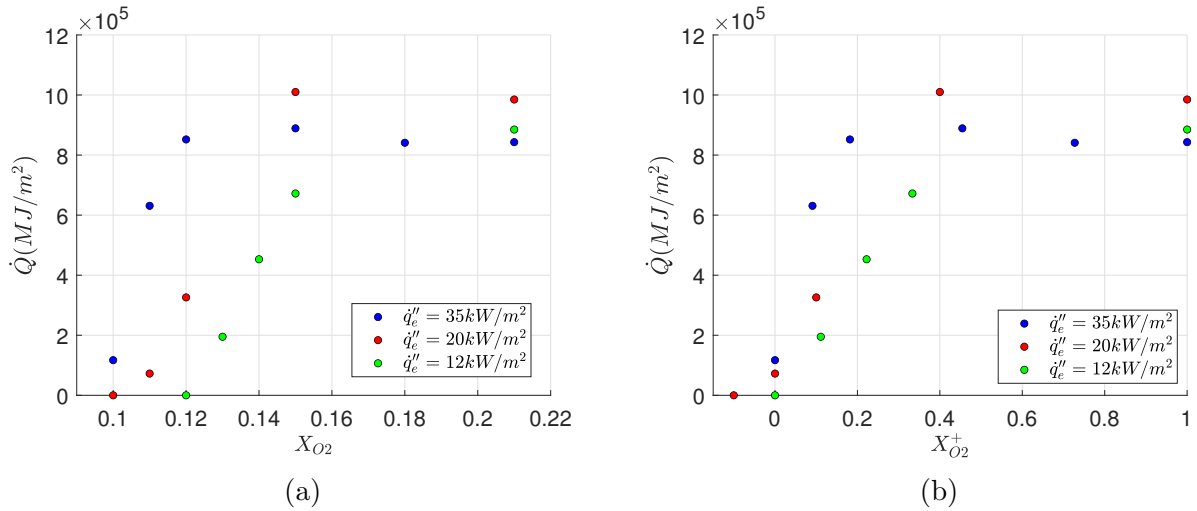

Figure 4.34: Total heat release $\dot{Q}$ for different external heat flux with respect to X_{O2}. b)Total heat release $\dot{Q}$ for different external heat flux with respect to X^+_{O2}.

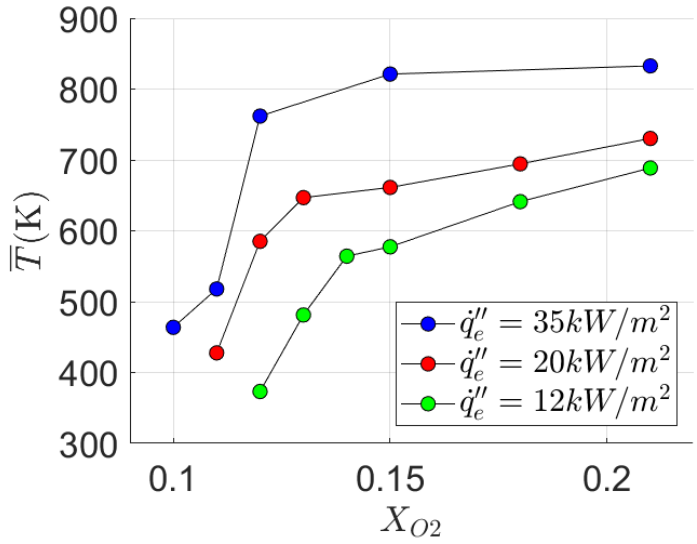

Figure 4.35: Average gaz temperatures for several oxygen concentrations and under several external heat fluxes.

The gas temperatures can be presented as the ratio $\frac{\overline{T_{O2}}}{\overline{T_{air}}}$, which represents the average temperature at a given oxygen concentration relative to the gas temperature at ambient air conditions. The results are visualized in Figure 4.36. The ratios show a similar trend as the gas temperature. At low oxygen concentrations, the temperature are almost half the ones obtained under air.

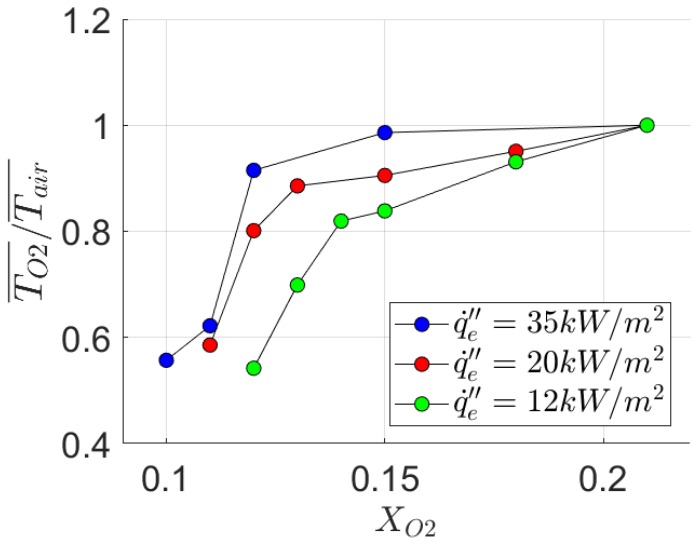

Figure 4.36: Averaged gas temperatures for several oxygen concentrations and heat fluxes.

	X_{O2}	$<\overline{T}>(K)$
$\dot{q}''_e = 35kW/m^2$	0.21	832,7
	0.15	821,1
	0.12	761,9
	0.11	517,9
	0.10	463,8
$\dot{q}''_e = 20kW/m^2$	0.21	730,3
	0.18	694,4
	0.15	661,2
	0.13	646,8
	0.12	585,1
	0.11	427,7
$\dot{q}''_e = 12kW/m^2$	0.21	688,6
	0.18	641,1
	0.15	577,3
	0.14	564,2
	0.13	481,2
	0.12	373,2

Table 4.7: Averaged gas temperatures for different external heat fluxes and oxygen concentrations

In Figure 4.38 the gas temperature is plotted against the specific mass loss rate. The plot shows a linear evolution of gas temperature with the specific mass loss rate, consistently

represented by a single trend line detailed in Equation 4.2.17.

$$< \overline{T} >= 7.16\dot{m}'' + 387 \tag{4.2.17}$$

This observation holds under varying external heat flux conditions, suggesting a robust and consistent relationship between gas temperature and specific mass loss rate. This linear correlation persists regardless of the external heat flux conditions, as indicated by the smooth trend line. As conditions become more prone to combustion, with higher $\dot{m}''$ values, there is a corresponding increase in heat release, leading to elevated gas temperatures. The direct correlation between gas temperature and specific mass loss rate emphasizes the dependence of temperature dynamics on combustion conditions.

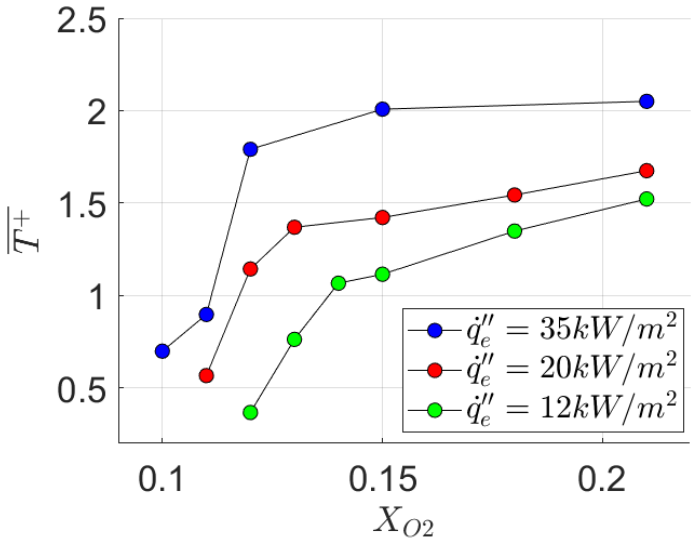

Figure 4.37: Average gaz temperatures in relation to the specific mass loss rate for several oxygen concentrations and external heat fluxes.

The relationship between gas temperatures and total heat flux $\dot{q}''_{tot}$ is shown in Figure 4.39. The average gas temperature shows a linear relationship with the total heat flux at the sample surface, as shown in Equation 4.2.18. This linear relationship is expected as the flame heat flux at the sample surface contributes significantly to the total heat flux. The flame heat flux is closely related to the flame temperature, i.e. an increase in the flame heat

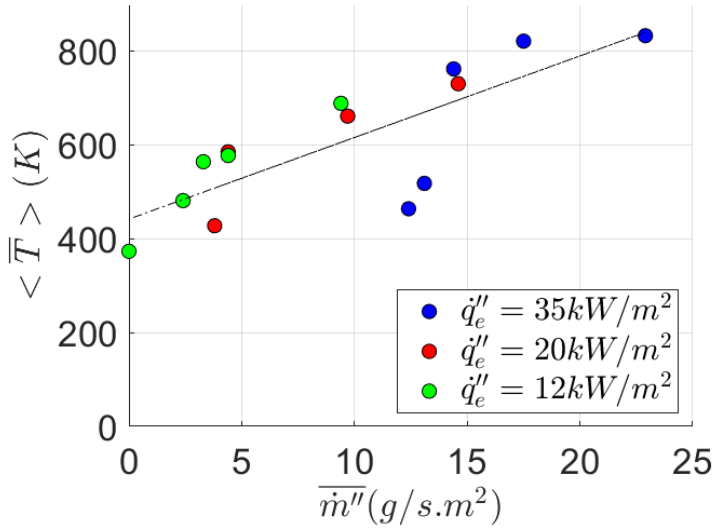

Figure 4.38: Average gas temperatures in relation to the specific mass loss rate for several oxygen concentrations and external heat fluxes.

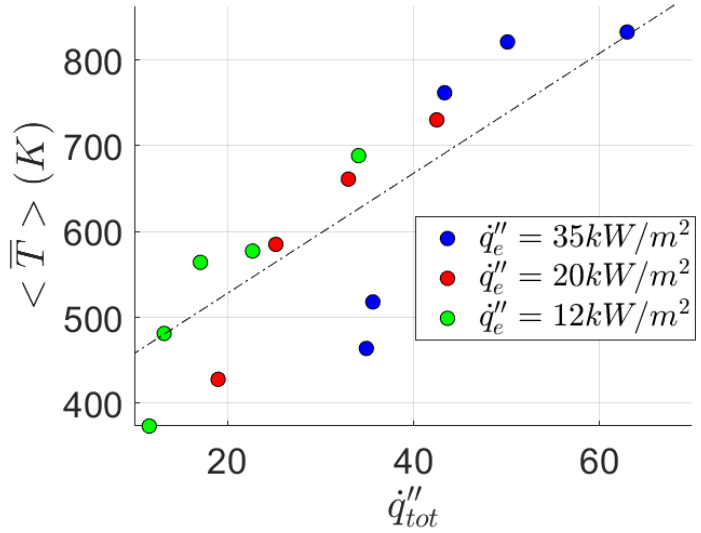

Figure 4.39: Average gas temperatures plotted against the total heat flux at the surface of the sample $\dot{q}''_{tot}$

flux corresponds to a higher gas temperature.

$$< \overline{T} >= 17.\dot{q}''_{tot} + 441 \tag{4.2.18}$$

4.3 Conclusion

This chapter is divided into two main sections. The first one deals with the effect on vitiation on the different combustion parameters, and the next one deals with the combined effect of vitiation and heat flux on the combustion parameters. The first section shows that the flame characteristics tend to change with less oxygen, becoming less bright and more detached from the sample surface. Parameters such as the heat release rate, the gas temperatures, the total heat release and the mass loss rate all show decrease with the oxygen concentration. For the in-sample temperature, the thermocouples reach a surface temperature of $550K$ faster for higher oxygen concentration. The second section allows the establishment of a model predicting the limiting oxygen concentration for each external heat flux. A dimensionless oxygen concentration X_{O2}^{+} is established. This parameter is used to find a model that predicts the ignition times. Additional models are fitted to predict the behavior of the several combustion parameters studied.

CONCLUSION AND PERSPECTIVES

This current work is dedicated to the study of the thermal behavior of PMMA as a function of the ambient conditions: the oxygen concentrations as well as the external heat fluxes. The study has been conducted using the controlled atmosphere cone calorimeter on horizontal thick sample of clear PMMA.

A state of the art review is done in the first chapter, showing the different parameters studied in the literature on the PMMA under air and in under-oxygenated atmopsheres. The literature review demonstrates that the oxygen content and the external heat flux have an impact on the combustion parameters. When oxygen levels fall, the PMMA's surface layer becomes more viscous, which affects mass transfer in the solid phase. The mass loss rate material is dependent on the oxygen concentration and decreases with decreasing oxygen levels. Heat release rate, flame form, and flame heat flux are among the gas phase features that are influenced by the oxygen content of the surrounding air. In addition, the external heat flux may have an effect on the limiting oxygen concentration. Is also highlighted the need to additional studies on the thermal behavior of the PMMA in under-oxygenated atmospheres. The experimental bench-scale used is described, as well as the instrumentation and the protocol used in Chapter 2. Some modifications have been made to the bench-scale and the sample to allow the measurements of specific parameters like the net heat flux at the surface of the sample, the temperatures into the sample and the gas temperatures in the chimney. The measurements and calculations performed are then presented.

The chapter 3 focuses on the results concerning the thermal decomposition and the combustion under air, for three different external heat fluxes. The main findings are summarised below:

Tests are conducted to find the critical heat flux, and the ignition times. The ignition time is dependant on the external heat flux, and it shows a hyperbolic trend. It increases with the decreasing of the external heat flux. The experimental critical heat flux is found to be $11.5 kW/m^2$ in accordance with the literature. Using the critical heat flux, additional ignition parameters have been calculated.

Observing the mass loss shows that there are five processes that can be used to describe the

PMMA thermal decomposition. A dimensionless time is introduced to overcome the delays caused by the difference in external heat flux. The values of the mass loss rate have been compared with the literature and a good agreement has been found.

Observing the mass loss shows that the thermal decomposition of PMMA takes place in five main steps. A dimensionless time is introduced to overcome the delays caused by the difference in external heat flux. The values of the mass loss rate have been compared with the literature and a good agreement is found.

The evolution of the in-sample temperatures and heating rates show a continuous growth with a marked increase as they approach the surface of the sample.

The heat release rate shows a decrease with the decreasing heat flux while the total heat release varies between 800 and $1000 MJ/m^2$.

The gas temperature evolutions are presented for different heights in the chimney. The 5 decomposition steps can also be seen on the plot of the gas temperatures. Concerning the averaged gas temperatures, the lowest thermocouple has a lower temperature than expected. The second thermocouple has the highest temperature, which continue to decrease while going up inside the stack.

The net heat flux received at the surface of the sample shows that the flame heat flux is considerable in comparison to the external heat flux emitted by the radiant cone. The ratio $\dot{q}''_{tot}$ to $\dot{q}''_e$ is expressed as a linear equation.

If chapter 3 provides insight into the behavior of the PMMA under air conditions for different external heat flux, it also provides a basis for comparison with the results obtained for different oxygen concentrations, presented in the following chapter. The chapter 4 is divided into 2 main sections. The first one focuses on the thermal behavior of the PMMA in under-oxygenated atmospheres under one external heat flux. The second focuses on the combined effect of both vitiation and irradiance levels. The main findings are detailed below:

The flame shows a bright yellow flame and is spread across the whole surface sample under air. As the oxygen drops, the flame becomes less luminous and bright. Getting closer to the critical oxygen concentrations, the flame detaches from the sample and becomes anchored at the spark plug. Finally, at the critical oxygen concentration, no flame are observed.

Tests are conducted to find the limiting oxygen concentration for several external heat flux. Establishing a clear cut between ignition and no ignition is complicated. In fact, for conditions that are close to the limit of the ignition, the results are not repeatable and their dispersion is important. Which is why, it is important to establish a zone where no repeatable results are observed. The limiting oxygen concentration is modelled in function of the external heat flux. Results show that the limiting oxygen concentration is dependent of the external heat flux. The value tend toward the higher value of oxygen when the external heat flux decrease.

The ignition a and extinction times are discussed in terms of $\frac{1}{\sqrt{t_{ig}}}$ and $\frac{1}{\sqrt{t_{ext}}}$ for a better representation. The ignition times and extinction times are longer for lower oxygen concentrations and external heat flux. A dimensionless oxygen concentration X_{O2}^{+} is introduced to take into account the different limiting oxygen concentrations that are result of different external heat flux.. The ratio $\frac{t_{ig,air}}{t_{ig,O2}}$ is expressed in terms of X_{O2}^{+} and a model describing this ratio is proposed.

The evolution of the averaged specific mass loss rate is found to be linear with the oxygen concentration, following one line with ever external heat flux. They are plotted as a ratio $\frac{\overline{\dot{m}''_{O2}}}{\dot{m}''_{air}}$ and compared to the results observed in the literature. The results show that for no or low external heat flux, the ratio $\frac{\overline{\dot{m}''_{O2}}}{\dot{m}''_{air}}$ follows the correlation of Peatross and Beyler. However, for a more significant external heat flux, the ratio deviates from the correlation. In an attempt to find one correlation that fits all the results, the ratio $\frac{\overline{\dot{m}''_{O2}}}{\dot{m}''_{air}}$ is plotted against the dimensionless oxygen concentration X_{O2}^{+}. A new linear model is found and shows a good fit for all the values.

The in-sample heating rates show a linear evolution with the dimensionless oxygen concentration. A dimensionless heating rate parameters is introduced and plotted against the dimensionless oxygen concentration. It is found that the dimensionless heating rate is equal to dimensionless oxygen concentration. To get the value of a heating rate at a given oxygen concentration, it is then sufficient to know the dimensionless oxygen concentration, the critical heating rate and the heating rate under air.

The net heat flux received at the surface of the sample shows a linear evolution with the

oxygen concentration. The flame heat flux, which is considered as the difference between the total heat flux received at the surface of the sample and the external heat flux emitted by the radiant heater, shows a linear evolution with the dimensionless oxygen concentration. The averaged specific mass loss rate and the averaged heating rate both show a linearity with the total heat flux. Two models are thus proposed.

The heat release rate (HRR) shows a decrease with the oxygen concentration. The ratio $\frac{\overline{\dot{Q}''_{O2}}}{\dot{Q}''_{air}}$ is plotted against the dimensionless oxygen concentration. It evolves linearly until a break in slope which happens at $X^+_{O2} = 0.28$. For $X^+_{O2} < 0.28$, the ratio $\frac{\overline{\dot{Q}''_{O2}}}{\dot{Q}''_{air}}$ drops suddenly. A similar behavior is observed for the total heat release.

Finally, the averaged gas temperature shows a decrease with the oxygen concentration. The gas temperatures decrease linearly with the specific mass loss rate as well as the external heat flux.

This chapter 4 allows the establishment of linear models that are able to describe the behavior of combustion parameters under different ambient conditions. This work constitutes a thorough experimental investigation of the combustion parameters in under-oxygenated atmospheres and different oxygen concentration. However, more work are required in order to fully understand the thermal behavior of the PMMA in those conditions:

The tests done to assess the heat flux at the surface of the sample required the insertion of a fluxmeter inside the sample, which can possibly change the outcome of the fluxmeter as mentioned earlier by constituting a thermal leak. In fact, the fluxmeter is supplied with water at ambient temperature to allow it to cool during the test. This cold gauge inside the sample constitutes a thermal leak that can disturb the energy balance of the sample. This effect on the overall thermal balance is unknown and hard to assess. Additional tests would be needed to be able to assess this error and eventually correct the measured heat flux.

The fluxmeter is positioned in the middle of the sample. However, the heat flux at other positions in the sample are different and the impact of the oxygen concentration on them is unknown. Further tests are needed.

In this work, the tests done are all under one air flow of 160l/min. The effect of the inlet air flow in conditions with low oxygen concentrations is not enough investigated. It would

necessitate more tests to assess this lack.

It can be also very interesting to complete the experiments with a detailed gas analysis of the gaseous compound emitted as a function of the oxygen concentration in order to have a better description of the chemical aspects.

During the present work, the PMMA in a bench-scale cone calorimeter is the main focus of the current effort. Thus it will be necessary to realize some tests at larger scales in order to check and to validate the results here obtained. Moreover, additional research is required using other materials.

Finally, new models should be developed from this experimental characaterization and the behavior of the polymer in under-oxygenated atmospheres must be taken into consideration in the numerical CFD models.

BIBLIOGRAPHY

[1] A Tewarson, JL Lee, and RF Pion. "The influence of oxygen concentration on fuel parameters for fire modeling". In: *Symposium (international) on combustion*. Vol. 18. Elsevier. 1981, pp. 563–570.

[2] S Fereres et al. "Mass flux at ignition in reduced pressure environments". In: *Combustion and flame* 158.7 (2011), pp. 1301–1306.

[3] S McAllister et al. "The combined effect of pressure and oxygen concentration on piloted ignition of a solid combustible". In: *Combustion and flame* 157.9 (2010), pp. 1753–1759.

[4] DJ Rasbash, DD Drysdale, and D Deepak. "Critical heat and mass transfer at pilot ignition and extinction of a material". In: *Fire safety journal* 10.1 (1986), pp. 1–10.

[5] A Tewarson and SD Ogden. "Fire behavior of polymethylmethacrylate". In: *Combustion and flame* 89.3-4 (1992), pp. 237–259.

[6] KC Tsai. "Orientation effect on cone calorimeter test results to assess fire hazard of materials". In: *Journal of hazardous materials* 172.2-3 (2009), pp. 763–772.

[7] M Försth and A Roos. "Absorptivity and its dependence on heat source temperature and degree of thermal breakdown". In: *Fire and Materials* 35.5 (2011), pp. 285–301.

[8] G Linteris et al. "Absorption and reflection of infrared radiation by polymers in fire-like environments". In: *Fire and Materials* 36.7 (2012), pp. 537–553.

[9] WR Zeng, SF Li, and WK Chow. "Preliminary studies on burning behavior of polymethylmethacrylate (PMMA)". In: *Journal of fire sciences* 20.4 (2002), pp. 297–317.

[10] WR Zeng, SF Li, and WK Chow. "Review on chemical reactions of burning poly (methyl methacrylate) PMMA". In: *Journal of Fire Sciences* 20.5 (2002), pp. 401–433.

[11] Standard ASTM. "E1354-99: Standard test method for heat and visible smoke release rates for materials and products using an oxygen consumption calorimeter". In: *ASTM International, West Conshohocken, PA* (1999).

[12] V Babrauskas et al. “A cone calorimeter for controlled-atmosphere studies”. In: *Fire and materials* 16.1 (1992), pp. 37–43.

[13] Standard ASTM. “E2058-03: Standard test method for measurement of synthetic polymer material flammability using a fire propagation apparatus”. In: *ASTM International, West Conshohocken, PA* (2003).

[14] A Tewarson and RF Pion. “Flammability of plastics—I. Burning intensity”. In: *Combustion and Flame* 26 (1976), pp. 85–103.

[15] N Bal. “Uncertainty and complexity in pyrolysis modelling”. PhD thesis. The University of Edinburgh, 2012.

[16] J Luche et al. “Characterization of thermal properties and analysis of combustion behavior of PMMA in a cone calorimeter”. In: *Fire safety journal* 46.7 (2011), pp. 451–461.

[17] HHG Jellinek and JE Clark. “A new technique for the study of high-polymer degradation reactions”. In: *Canadian Journal of Chemistry* 41.2 (1963), pp. 355–362.

[18] T Kashiwagi. “Polymer combustion and flammability—Role of the condensed phase”. In: *Symposium (International) on Combustion*. Vol. 25. 1. Elsevier. 1994, pp. 1423–1437.

[19] T Kashiwagi and TJ Ohlemiller. “A study of oxygen effects on nonflaming transient gasification of PMMA and PE during thermal irradiation”. In: *Symposium (International) on Combustion*. Vol. 19. Elsevier. 1982, pp. 815–823.

[20] ML Janssens, J Kimble, and D Murphy. “Computer tools to determine material properties for fire growth modeling from cone calorimeter data”. In: *Fire and Materials* 8 (2003), pp. 377–387.

[21] MA Delichatsios. “Piloted ignition times, critical heat fluxes and mass loss rates at reduced oxygen atmospheres”. In: *Fire Safety Journal* 40.3 (2005), pp. 197–212.

[22] A Tewarson. “Generation of heat and chemical compounds in fires”. In: *The SFPE Handbook Of Fire Protection Engineering* 1 (1988).

[23] M Zarzecki et al. “The effect of pressure and oxygen concentration on the combustion of PMMA”. In: *Combustion and Flame* 160.8 (2013), pp. 1519–1530.

[24] JG Quintiere. “Fundamentals of fire phenomena”. In: (2006).

[25] JR Hallman. “Ignition characteristics of plastics and rubber”. PhD thesis. The University of Oklahoma, 1971.

[26] HE Thomson and DD Drysdale. “Flammability of plastics I: ignition temperatures”. In: *Fire and Materials* 11.4 (1987), pp. 163–172.

[27] HR Wesson, JR Welker, and CM Sliepcevich. “The piloted ignition of wood by thermal radiation”. In: *Combustion and Flame* 16.3 (1971), pp. 303–310.

[28] BT Rhodes and JG Quintiere. “Burning rate and flame heat flux for PMMA in a cone calorimeter”. In: *Fire Safety Journal* 26.3 (1996), pp. 221–240.

[29] D Hopkins Jr and JG Quintiere. “Material fire properties and predictions for thermoplastics”. In: *Fire safety journal* 26.3 (1996), pp. 241–268.

[30] NA Dembsey PA Beaulieu. “Effect of oxygen on flame heat flux in horizontal and vertical orientations”. In: *Fire Safety Journal* 43.6 (2008), pp. 410–428.

[31] PA Beaulieu, NA Dembsey, and RL Alpert. “A new material flammability apparatus and measurement techniques”. In: *Inernational SAMPE symposium and exhibition*. SAMPE; 1999. 2003, pp. 2444–2455.

[32] L Orloff, J De Ris, and GH Markstein. “Upward turbulent fire spread and burning of fuel surface”. In: *Symposium (International) on Combustion*. Vol. 15. 1. Elsevier. 1975, pp. 183–192.

[33] L Orloff, AT Modak, and RL Alpert. “Burning of large-scale vertical surfaces”. In: *Symposium (International) on combustion*. Vol. 16. 1. Elsevier. 1977, pp. 1345–1354.

[34] Y Pizzo et al. “Steady and transient pyrolysis of thick clear PMMA slabs”. In: *Combustion and Flame* 162.1 (2015), pp. 226–236.

[35] A Kacem et al. “A fully coupled fluid/solid model for open air combustion of horizontally-oriented PMMA samples”. In: *Combustion and Flame* 170 (2016), pp. 135–147.

[36] D Alibert. “Effet de la sous-oxygénation sur les paramètres de combustion”. PhD thesis. Aix-Marseille, 2017.

[37] J Quintiere, Mt Harkleroad, and Y Hasemi. “Wall flames and implications for upward flame spread”. In: *Combustion Science and Technology* 48.3-4 (1986), pp. 191–222.

[38] KC Tsai and FS Wan. “Upward flame spread: the width effect”. In: *Fire Safety Science* 8 (2005), pp. 409–419.

[39] IT Leventon and SI Stoliarov. “Evolution of flame to surface heat flux during upward flame spread on poly (methyl methacrylate)”. In: *Proceedings of the Combustion Institute* 34.2 (2013), pp. 2523–2530.

[40] G Santo and F Tamanini. “Influence of oxygen depletion on the radiative properties of PMMA flames”. In: *Symposium (International) on Combustion*. Vol. 18. Elsevier. 1981, pp. 619–631.

[41] GW Mulholland et al. “The effect of oxygen concentration on CO and smoke produced by flames”. In: *Fire safety science* 3 (1991), pp. 585–594.

[42] S Chatenet. “An instrumented controlled-atmosphere cone calorimeter to characterize electrical cable behavior in depleted fires”. PhD thesis. Université de Lille, 2019.

[43] International Organization for Standardization. *ISO 13927: Plastics–Simple heat release test using a conical radiant heater and a thermopile detector*. 2003.

[44] D Marquis, E Guillaume, and D Lesenechal. “Accuracy (trueness and precision) of cone calorimeter tests with and without a vitiated air enclosure”. In: *Procedia Engineering* 62 (2013), pp. 103–119.

[45] D Marquis, E Guillaume, and A Camillo. “Effects of controlled ventilation conditions on combustibility assessment from a controlled atmosphere cone calorimeter”. In: *Proceeding of the 18th international conference on fire safety*. 2014.

[46] G Maragkos and B Merci. “Large eddy simulations of flame extinction in a turbulent line burner”. In: *Fire Safety Journal* 105 (2019), pp. 216–226.

[47] V Lecoustre et al. “Local extinction of diffusion flames in fires”. In: *Fire Safety Science* 10 (2011), pp. 583–595.

[48] C K Law. *Combustion physics*. Cambridge university press, 2010.

[49] N Peters. *Turbulent combustion*. 2001.

[50] FA Williams. *Combustion theory*. CRC Press, 2018.

[51] FA Williams. “Progress in knowledge of flamelet structure and extinction”. In: *Progress in Energy and Combustion Science* 26.4-6 (2000), pp. 657–682.

[52] KM Gibov TB Zhubanov. “Oxygen index and minimum limiting rates of polymer combustion”. In: *Fire and materials* 12.4 (1988), pp. 169–172.

[53] D Drysdale. *An introduction to fire dynamics*. John Wiley & Sons, 2011.

[54] MJ Peatross and CL Beyler. “Ventilation effects on compartment fire characterization”. In: *Fire Safety Science* 5 (1997), pp. 403–414.

[55] Y Utiskul. “Theoretical and experimental study on fully-developed compartment fires”. PhD thesis. 2006.

[56] JG Quintiere. “The burning of wood and plastic cribs in an enclosure”. In: *NBSIR 80-2054* 1 (1980).

[57] JG Quintiere. “An approach to modeling wall fire spread in a room”. In: *Fire Safety Journal* 3.3 (1981), pp. 201–214.

[58] DB Spalding. “Combustion of liquid fuels”. In: *Nature* 165.4187 (1950), pp. 160–160.

[59] J Li and S I Stoliarov. “Measurement of kinetics and thermodynamics of the thermal degradation for non-charring polymers”. In: *Combustion and Flame* 160.7 (2013), pp. 1287–1297.

[60] International Organization for Standardization. *ISO 291: plastics: standard atmospheres for conditioning and testing*. 2008.

[61] International Organization for Standardization. *ISO 5660-1: Reaction-to-fire tests-Heat release, smoke production and mass loss rate-Part 1:cone calorimeter method*. 2002.

[62] WM Thornton. "The relation of oxygen to the heat of combustion of organic compounds". In: *The London, Edinburgh, and Dublin Philosophical Magazine and Journal of Science* 33.194 (1917), pp. 196–203.

[63] ML Janssens. "Measuring rate of heat release by oxygen consumption". In: *Fire technology* 27 (1991), pp. 234–249.

[64] WJ Parker. "Calculations of the heat release rate by oxygen consumption for various applications". In: *Journal of fire sciences* 2.5 (1984), pp. 380–395.

[65] M Werrel et al. "The calculation of the heat release rate by oxygen consumption in a controlled-atmosphere cone calorimeter". In: *Fire and materials* 38.2 (2014), pp. 204–226.

[66] C Huggett. "Estimation of rate of heat release by means of oxygen consumption measurements". In: *Fire and materials* 4.2 (1980), pp. 61–65.

[67] JA Ang et al. "Temperature and velocity profiles in sooting free convection diffusion flames". In: *American Institute of Aeronautics and Astronautics journal* 26.3 (1988), pp. 323–329.

[68] AJ Yule, DS Taylor, and NA Chigier. "Thermocouple signal processing and on-line digital compensation". In: *Journal of Energy* 2.4 (1978), pp. 223–231.

[69] FM White. *Heat and Mass Transfer*. Addison-Wesley, 1988.

[70] RBS Bird and EN Lightfoot. *Transport Phenomena*. John Wiley & Sons, 1960.

[71] GF Hewitt, GL Shires, and TR Bott. *Process Heat Transfer*. CRC-Press, 1994.

[72] H Kramers. "Heat transfer from spheres to flowing media". In: *physica* 12.2-3 (1946), pp. 61–80.

[73] BR Munson, DF Young, and TH Okiishi. *Fundamentals of fluid mechanics*. Oceanographic Literature Review, 1995.

[74] TL Bergman. *Fundamentals of heat and mass transfer*. John Wiley & Sons, 2011.

[75] A Feingold and KG Gupta. “New analytical approach to the evaluation of configuration factors in radiation from spheres and infinitely long cylinders”. In: *Journal of Heat Transfer* 92 (1970), pp. 69–76.

[76] C Vovelle, R Akrich, and JL Delfau. “Mass loss rate measurements on solid materials under radiative heating”. In: *Combustion Science and Technology* 36.1-2 (1984), pp. 1–18.

[77] R Parot et al. “A simplified analytical model for radiation dominated ignition of solid fuels exposed to multiple non-steady heat fluxes”. In: *Combustion and Flame* 237 (2022), p. 111866.

[78] E Mikkola and IS Wichman. “On the thermal ignition of combustible materials”. In: *Fire and Materials* 14.3 (1989), pp. 87–96.

[79] D Price et al. “Flame retardance of poly (methyl methacrylate) modified with phosphorus-containing compounds”. In: *Polymer Degradation and Stability* 77.2 (2002), pp. 227–233.

[80] A Tewarson. “Experimental evaluation of flammability parameters of polymeric materials”. In: *Flame-Retardant Polymeric Materials*. Springer, 1982, pp. 97–153.

[81] M Chaos et al. “Evaluation of optimization schemes and determination of solid fuel properties for CFD fire models using bench-scale pyrolysis tests”. In: *Proceedings of the Combustion Institute* 33.2 (2011), pp. 2599–2606.

[82] JL Cordova and AC Fernandez-Pello. “Convection effects on the endothermic gasification and piloted ignition of a radiatively heated combustible solid”. In: *Combustion science and technology* 156.1 (2000), pp. 271–289.

[83] C Lautenberger and C Fernandez-Pello. “Generalized pyrolysis model for combustible solids”. In: *Fire Safety Journal* 44.6 (2009), pp. 819–839.

[84] EG Brehob and AK Kulkarni. “Experimental measurements of upward flame spread on a vertical wall with external radiation”. In: *Fire Safety Journal* 31.3 (1998), pp. 181–200.

[85] JEJ Staggs. "The heat of gasification of polymers". In: *Fire safety journal* 39.8 (2004), pp. 711–720.

[86] KD Steckler et al. "Analytical model for transient gasification of non-charring thermoplastic materials". In: *Fire Safety Science-Third International Symposium*. 1991, pp. 895–904.

[87] SI Stoliarov and RN Walters. "Determination of the heats of gasification of polymers using differential scanning calorimetry". In: *Polymer Degradation and Stability* 93.2 (2008), pp. 422–427.

[88] C Vovelle et al. "Experimental and numerical study of the thermal degradation of PMMA". In: *Combustion Science and Technology* 53.2-3 (1987), pp. 187–201.

Modélisation de la réaction au feu des matériaux en milieux sous ventilés. Application au PMMA.

Résumé

Dans le domaine de la sécurité incendie, l'inflammation et la combustion des matériaux polymères sont étroitement liées aux conditions ambiantes, notamment à la concentration en oxygène. Dans les premiers instant, l'incendie présente des caractéristiques similaires à une situation bien ventilée, mais au fur et à mesure que le feu se développe et que les matériaux combustibles se consument, la disponibilité d'oxygène peut diminuer. Le feu passe alors à un état de sous-oxygénation caractérisé par un comportement complexe et instable de la phase gazeuse. La diminution de l'oxygène influence également le transfert de chaleur et de masse à l'intérieur du matériau étudié, affectant sa décomposition thermique et sa combustion, ainsi que la cinétique et la nature des produits gazeux émis. Les études expérimentales ayant pour enjeu de caractériser l'influence de la sous oxygénation sur la réaction au feu des matériaux solides restent très limitées, et de manière corrélée, les modèles numériques sont souvent non validés pour des telles atmosphères. Dans ce contexte, le présent travail vise à caractériser la décomposition thermique et la combustion des matériaux polymères dans des environnements viciés, en se focalisant sur le poly(méthyl)méthacrylate (PMMA). Un cône calorimètre à atmosphère contrôlée (CACC) a alors été instrumenté de sorte à caractériser l'influence de la concentration d'oxygène sur les processus de décomposition thermique et de combustion : perte de masse, champs de températures, flux de chaleur, composition gazeuse. Au cours de l'étude expérimentale des concentrations d'oxygène allant de 10% à 21% ont été étudiées, pour 3 flux de chaleur. Les résultats expérimentaux soulignent l'influence significative de la concentration d'oxygène et du flux thermique externe sur le transfert de chaleur et de masse ainsi que sur la combustion du PMMA. La perte de masse, le taux de dégagement de chaleur et les températures représentent des progressions linéaires avec la concentration d'oxygène jusqu'à une certaine concentration pour laquelle le comportement devient chaotique et imprévisible. Un paramètre adimensionné représentant la concentration d'oxygène a été introduit, permettant de trouver des corrélations adaptées pour les différents paramètres

étudiés.

Mots clés: Air confiné, Combustion, Essais de comportement au feu, Incendies–Prévention, Polyméthacrylate de méthyle–Inflammabilité, Pyrolyse, Transfert de chaleur, Transfert de masse

Modeling of the reaction to fire of materials in under-ventilated spaces. Application on the PMMA.

Abstract

In the field of fire safety, the ignition and combustion of polymeric materials are closely linked to the ambient conditions, particularly the oxygen concentration. In the initial stages, the fire displays characteristics similar to a well-ventilated situation, but as the fire develops and the combustible materials burn, the availability of oxygen decreases. The fire moves into a state of under-oxygenation characterised by complex and unstable behaviour of the gaseous phase. Oxygen depletion also affects heat and mass transfer within the material under study, affecting its thermal decomposition and combustion, as well as the kinetics and nature of the gaseous products. Experimental studies aimed at characterising the influence of the under-oxygenation on the reaction to fire of solid materials are still very limited in the literature, and numerical models are often not validated for such atmospheres. In this context, the present work aims to characterise the thermal decomposition and the combustion of polymeric materials in contaminated environments, focusing on poly(methyl)methacrylate (PMMA). A controlled atmosphere calorimeter cone (CACC) was instrumented to characterise the influence of oxygen concentration on thermal decomposition and combustion processes: mass loss, temperature fields, heat flux, gas composition. During the experimental study, oxygen concentrations ranging from 10% to 21% were studied, for 3 different heat flows. The experimental results highlight the significant influence of oxygen concentration and external heat flux on heat and mass transfer as well as on PMMA combustion. Mass loss, heat release rate and temperatures show linear progression with oxygen concentration

up to a certain value where the behaviour becomes chaotic and unpredictable. A dimensionless parameter representing the oxygen concentration was introduced, allowing suitable correlations to be found for the various parameters studied.

Keywords: Calorimeters, Combustion, Fire testing, Fire prevention, Polymethylmethacrylate–Flammability, Pyrolysis, Heat-Transmission, Mass transfer